

OLD DOMINION UNIVERSITY
DEPARTMENT OF MECHANICAL ENGINEERING AND MECHANICS
COLLEGE OF ENGINEERING AND TECHNOLOGY
NORFOLK, VIRGINIA 23529

**EFFECTS OF NOSE BLUNTNES AND SHOCK-SHOCK INTERACTIONS
ON BLUNT BODIES IN VISCOUS HYPERSONIC FLOWS**

By

D. J. Singh, Graduate Research Assistant

and

S. N. Tiwari, Principal Investigator

Progress Report
For the period ended December 31, 1989

Prepared for
National Aeronautics and Space Administration
Langley Research Center
Hampton, Virginia 23665

Under
Research Grant NAG-1-423
Drs. Ajay Kumar and J. Philip Drummond
Technical Monitors
FLDMD-Computational Methods Branch

January 1990

(NASA-CR-184451) EFFECTS OF NOSE BLUNTNES
AND SHOCK-SHOCK INTERACTIONS ON BLUNT BODIES
IN VISCOUS HYPERSONIC FLOWS Progress Report,
period ending 31 Dec. 1989 (Old Dominion
Univ.) 197 p

N90-20950

Unclass

CSL 01A 13/02 027111

OLD DOMINION UNIVERSITY
DEPARTMENT OF MECHANICAL ENGINEERING AND MECHANICS
COLLEGE OF ENGINEERING AND TECHNOLOGY
NORFOLK, VIRGINIA 23529

**EFFECTS OF NOSE BLUNTNES AND SHOCK-SHOCK INTERACTIONS
ON BLUNT BODIES IN VISCOUS HYPERSONIC FLOWS**

By

D. J. Singh, Graduate Research Assistant

and

S. N. Tiwari, Principal Investigator

Progress Report

For the period ended December 31, 1989

Prepared for
National Aeronautics and Space Administration
Langley Research Center
Hampton, Virginia 23665

Under
Research Grant NAG-1-423
Drs. Ajay Kumar and J. Philip Drummond
Technical Monitors
FLDMD-Computational Methods Branch

Submitted by the
Old Dominion University Research Foundation
P.O. Box 6369
Norfolk, Virginia 23508-0369

January 1990

FOREWORD

This is a progress report on the research project, "Analysis and Computation of Internal Flow-Field in a Scramjet Engine," for the period ended December 31, 1989. Special attention during this period was directed to "Effects of Nose Bluntness and Shock-Shock Interactions on Blunt Bodies in Viscous Hypersonic Flows." The work was supported by the NASA Langley Research Center (Computational Methods Branch of the Fluid Mechanics Division) through the grant NAG-1-423. The grant was monitored by Drs. Ajay Kumar and J. Philip Drummond, FLDMD-Computational Methods Branch, Mail Stop 156.

EFFECTS OF NOSE BLUNTNES AND SHOCK-SHOCK INTERACTIONS ON BLUNT BODIES IN VISCOUS HYPERSONIC FLOWS

By

D. J. Singh¹ and S. N. Tiwari²

SUMMARY

A numerical study has been conducted to investigate the effects of blunt leading edges on the viscous flow field around a hypersonic vehicle such as the proposed National Aero-Space Plane. Attention is focused on two specific regions of the flow field. In the first region, effects of nose bluntness on the forebody flow field are investigated. The second region of the flow considered is around the leading edges of the scramjet inlet. In this region, the interaction of the forebody shock with the shock produced by the blunt leading edges of the inlet compression surfaces is analyzed. Analysis of these flow regions is required to accurately predict the overall flow field as well as to get necessary information on localized zones of high pressure and intense heating. The results for the forebody flow field are discussed first followed by the results for the shock interaction in the inlet leading edge region.

The forebody is modeled by slender cones and ogives with a spherically blunted nose. A combination of Navier-Stokes and parabolized Navier-Stokes equations is used to compute the flow field. The influence of entropy layer thickness on the extent of the leading edge effects is also considered. The extent of downstream effects of leading edge thickness are determined at Mach

¹Graduate Research Assistant, Department of Mechanical Engineering and Mechanics, Old Dominion University, Norfolk, Virginia 23529.

²Eminent Professor, Department of Mechanical Engineering and Mechanics, Old Dominion University, Norfolk, Virginia 23529.

numbers of 10 and 20 for cone angles of 5° , 10° , and 20° . Three values of nose bluntness are considered with the smallest nose blunting (0.0025m) representing the sharp cone/ogive. Depending upon the flow conditions and the geometry, significant differences have been found between the sharp and the blunted bodies; the differences persist as far as 236 nose radii downstream. Also, the bluntness effects decrease with increasing cone angle. The results show that the wall quantities are not affected much by the inclusion of high temperature effects through equilibrium chemistry.

For the flow region around the inlet, depending upon the Mach number and the angle of attack, the forebody shock can interact either with the blunt cowl leading edge shock or with the shock produced by the blunt leading edges of the swept sidewall compression surfaces of the inlet. For the interaction at the cowl leading edge, the forebody shock is assumed planar and the cowl is modeled by a two-dimensional cylindrically blunted wedge of infinite width. Use of the full Navier-Stokes equations is made on the cowl forebody and the thin-layer Navier-Stokes equations are suitably modified for space marching on the cowl afterbody. The results of the study show that the flow around the cowl is significantly altered by the impinging shock. The peak value of pressure is found to be nine times and heating rates eight times the stagnation point value for the unimpinged case at Mach 8.03. The peak values were slightly lower for Mach 5.94 calculations. The use of solution adaptive grids is made to properly resolve the flow field. The peak heating rates for the unadapted grid was four times the unimpinged stagnation point value versus eight times with the adapted grid. A preliminary study was also conducted to determine the influence of shock-shock interaction on the blunt leading edges of the swept sidewalls of the inlet. For this configuration, the flow field is fully three-dimensional. A three-dimensional thin-layer

Navier-Stokes code had been used to calculate the flow field. The peak pressure for this case is found to be 2.25 times and the peak heating three times the unimpinged stagnation values. The results of the study are compared with the available experimental and numerical results. This study presents the first full three-dimensional analysis of the shock-shock interaction on the swept inlet sidewalls and the accurate numerical solution to date using full Navier-Stokes equations for the two-dimensional interaction on the cowl leading edge.

TABLE OF CONTENTS

	<u>Page</u>
FOREWORD.....	iii
SUMMARY.....	iv
TABLE OF CONTENTS.....	vii
LIST OF FIGURES.....	ix
LIST OF TABLES.....	xiv
LIST OF SYMBOLS.....	xv

<u>Chapter</u>	<u>Page</u>
1 INTRODUCTION.....	1
2 LITERATURE SURVEY.....	5
3 DOWNSTREAM EFFECTS OF NOSE BLUNTNESS.....	15
3.1 Entropy Layer.....	18
3.2 Governing Equations.....	21
3.3 Method of Solution.....	25
3.4 Equilibrium Chemistry.....	28
3.5 Validation.....	29
4 EFFECTS OF SHOCK-SHOCK INTERACTIONS.....	30
4.1 Classification.....	31
4.2 Governing Equations.....	41
4.2.1 Nondimensionalization.....	42
4.2.2 Coordinate Transformation.....	43
4.2.3 Finite Volume Formulation.....	45
4.3 Method of Solution.....	46
4.3.1 Flux Vector Splitting.....	49
4.3.2 Algorithm.....	51
4.4 Grid Generation.....	55

TABLE OF CONTENTS (Continued)

<u>Chapter</u>	<u>Page</u>
5 RESULTS AND DISCUSSION.....	61
5.1 Parametric Study of Nose Bluntness Effects.....	61
5.2 Forebody and the Cowl Shock Interaction.....	101
5.3 Forebody Shock and the Inlet Sidewall Shock Interaction...	138
6 CONCLUSIONS.....	155
REFERENCES.....	158
APPENDICES	
A EQUILIBRIUM CHEMISTRY.....	165
B ADAPTIVE GRID.....	167
C RADIATIVE INTERACTIONS IN LAMINAR FLOWS.....	169

LIST OF FIGURES

<u>Figure</u>	<u>Page</u>
3.1 Physical model for hypersonic flow past a blunted cone.	16
3.2 Physical model for hypersonic flow past an ogive.	17
3.3 Typical grid for finite difference calculations.	27
4.1 Physical model for forebody and cowl shock interaction.	32
4.2 Physical model for forebody and inlet shock interaction.	33
4.3 Type I shock-shock interaction.	35
4.4 Type II shock-shock interaction.	36
4.5 Type III shock-shock interaction.	37
4.6 Type IV shock-shock interaction.	38
4.7 Type V shock-shock interaction.	39
4.8 Type VI shock-shock interaction.	40
4.9 Finite volume formulation.	47
4.10 Unadapted grid for two-dimensional calculations.	58
4.11 Adapted grid for two-dimensional calculations.	59
4.12 Grid for three-dimensional calculations.	60
5.1 Comparison of wall pressure with the inviscid theory.	63
5.2 Comparison of shock standoff distance with the inviscid theory. . . .	64
5.3 Comparison of skin friction coefficient with the laminar theory. . . .	65
5.4 Comparison of heat transfer coefficient with the laminar theory. . . .	66

<u>Figure</u>	<u>Page</u>
5.5 Variation of wall pressure with the axial distance for $\theta_c = 5^\circ$ at various Mach numbers.	69
5.6 Variation of shock standoff distance with the axial distance for $\theta_c = 5^\circ$ at various Mach numbers.	70
5.7 Variation of wall heat transfer with the axial distance for $\theta_c = 5^\circ$ at various Mach numbers.	71
5.8 Variation of skin friction with the axial distance for $\theta_c = 5^\circ$ at various Mach numbers.	72
5.9 Variation of wall pressure with the axial distance for $\theta_c = 5^\circ, 10^\circ$ and 20° at $M_\infty = 20$	78
5.10 Variation of shock standoff distance with the axial distance for $\theta_c = 20^\circ$ at $M_\infty = 20$	79
5.11 Variation of wall heat transfer with the axial distance for $\theta_c = 5^\circ, 10^\circ$ and 20° at $M_\infty = 20$	80
5.12 Variation of skin friction with the axial distance for $\theta_c = 5^\circ, 10^\circ$ and 20° at $M_\infty = 20$	81
5.13 Variation of wall pressure with the axial distance for $\theta_c = 5^\circ$ at various Reynolds numbers.	82
5.14 Variation of shock standoff distance with the axial distance for $\theta_c = 5^\circ$ at various Reynolds numbers.	83
5.15 Variation of wall heat transfer with the axial distance for $\theta_c = 5^\circ$ at various Reynolds numbers.	84
5.16 Variation of skin friction with the axial distance for $\theta_c = 5^\circ$ at various Reynolds numbers.	85
5.17 Variation of wall pressure with the axial distance for ogive at various Mach numbers.	87

<u>Figure</u>	<u>Page</u>
5.18 Variation of shock standoff distance with the axial distance for ogive at various Mach numbers.	88
5.19 Variation of wall heat transfer with the axial distance for ogive at various Mach numbers.	89
5.20 Variation of skin friction with the axial distance for ogive at various Mach numbers.	90
5.21 Variation of wall pressure with the axial distance for $\theta_c = 10^0, 20^0$ and ogive at $M_\infty = 20$	91
5.22 Comparison of velocity profiles at $x = 0.5, 1.0$, and 5.0 m for ogive at Mach 20.	93
5.23 Comparison of temperature profiles at $x = 0.5, 1.0$, and 5.0 m for ogive at Mach 20.	94
5.24 Comparison of wall pressure for equilibrium and perfect gas.	96
5.25 Comparison of shock standoff for equilibrium and perfect gas.	97
5.26 Comparison of wall heat transfer equilibrium and perfect gas.	98
5.27 Comparison of skin friction for equilibrium and perfect gas.	99
5.28 Comparison of temperature profiles for equilibrium and perfect gas at $x = 0.5, 1.0$, and 5.0 m for ogive at Mach 20.	100
5.29 Computational domain.	102
5.30 Temperature contours for the cowl forebody, $M_\infty = 8.03$	105
5.31 Mach number contours for the cowl forebody, $M_\infty = 8.03$	106
5.32 Pressure number contours for the cowl forebody, $M_\infty = 8.03$	107
5.33 Density contours for the cowl forebody, $M_\infty = 8.03$	108
5.34 Variation of surface pressure for the cowl forebody, $M_\infty = 8.03$	109
5.35 Variation of surface heat transfer for the cowl forebody, $M_\infty = 8.03$	110
5.36 Temperature contours for the cowl forebody for $M_\infty = 8.03$ with adapted grid.	112

<u>Figure</u>	<u>Page</u>
5.37 Mach number contours for the cowl forebody, $M_\infty = 8.03$ with adapted grid	113
5.38 Pressure contours for the cowl forebody for $M_\infty = 8.03$ with adapted grid.	114
5.39 Density contours for the cowl forebody, $M_\infty = 8.03$ with adapted grid	115
5.40 Velocity vectors for the cowl forebody, $M_\infty = 8.03$ with adapted grid.	116
5.41 Variation of surface pressure for the cowl forebody, $M_\infty = 8.03$ with adapted grid.	118
5.42 Variation of surface heat transfer for the cowl forebody, $M_\infty = 8.03$ with adapted grid.	119
5.43 Temperature contours on the windward side of the cowl afterbody, $M_\infty = 8.03$	122
5.44 Temperature contours on the leeward side of the cowl afterbody, $M_\infty = 8.03$	123
5.45 Mach number contours on the windward side of the cowl afterbody, $M_\infty = 8.03$	124
5.46 Mach number contours on the leeward side of the cowl afterbody, $M_\infty = 8.03$	125
5.47 Variation of shock standoff distance with axial distance for the cowl afterbody, $M_\infty = 8.03$	126
5.48 Variation of surface pressure with axial distance for the cowl afterbody, $M_\infty = 8.03$	127
5.49 Temperature for the cowl forebody, $M_\infty = 5.94$	128
5.50 Mach contours for the cowl forebody, $M_\infty = 5.94$	129
5.51 Pressure contours for the cowl forebody, $M_\infty = 5.94$	130
5.52 Density contours for the cowl forebody, $M_\infty = 5.94$	131
5.53 Variation of surface pressure for the cowl forebody, $M_\infty = 5.94$. . .	132

<u>Figure</u>	<u>Page</u>
5.54 Variation of surface heat transfer for the cowl forebody, $M_\infty = 5.94$.	133
5.55 Mach number contours on the windward side of the cowl afterbody, $M_\infty = 5.94$.	134
5.56 Mach number contours on the leeward side of the cowl afterbody, $M_\infty = 5.94$.	135
5.57 Variation of shock standoff distance with axial distance for the cowl afterbody, $M_\infty = 5.94$	136
5.58 Variation of surface pressure with axial distance for the cowl after- body, $M_\infty = 5.94$	137
5.59 Pressure contours for the unimpinged case in stagnation ($\theta = 0$) and $z = \text{constant}$ plane.	140
5.60 Temperature, Mach number and the Pressure contours in the stag- nation plane($\theta = 0$).	142
5.61 Temperature contours in the $z = 2.3, 2.6$, and 2.8 cm plane.	143
5.62 Local regions of high heating rates and corresponding schlieren pho- tograph.	144
5.63 Surface pressure contours for Type V interaction.	145
5.64 Pressure contours in the stagnation plane($\theta = 0$).	146
5.65 Comparison of surface pressure with the experimental data.	149
5.66 Comparison of surface heat transfer with the experimental data.	150
5.67 Variation of the surface pressure in various $y = \text{constant}$ planes	151
5.68 Variation of the surface heat transfer in various $y = \text{constant}$ planes	152
5.69 Variation of the surface pressure in various $z = \text{constant}$ planes	153
5.70 Variation of the surface heat transfer in various $z = \text{constant}$ planes	154

LIST OF TABLES

<u>Table</u>	<u>Page</u>
5.1 Flow conditions for the forebody calculations	67
5.2 Entropy swallowing distance (x/R_n) for 5° cone at $M_\infty = 10$	74
5.3 Distance (x/R_n) up to which bluntness effect persist for $M_\infty = 10$. .	75
5.4 Distance (x/R_n) up to which bluntness effect persist for $M_\infty = 20$. .	76
5.5 Freestream and stagnation point conditions for the cowl.	104
5.6 Freestream conditions for inlet.	139

LIST OF SYMBOLS

a	= speed of sound
C_{DT}	= drag coefficient of spherical nose
C_f	= coefficient of skin friction
c_p	= specific heat at constant pressure
C_h	= coefficient of heat transfer
e	= total energy per unit volume
J	= transformation jacobian
\dot{m}	= mass flow rate
M	= Mach number
p	= pressure
Pr	= Prandtl number
Q	= conservation variable
q	= heat transfer
Q_w	= wall heat transfer, nondimensionalized by $\rho_\infty U_\infty^3$
R, S	= viscous terms of Navier-Stokes equations
Re	= Reynolds number
R_n	= nose radius
S	= distance along body surface measured from the stagnation point
\bar{S}	= S/R_n
S_c	= swallowing distance
T	= temperature
u	= axial velocity

x	=streamwise coordinate in physical domain measured from virtual tip of sharp nose
\bar{x}	$= x/R_n$
y	= normal coordinate in physical domain
\bar{y}	$= y/R_n$
γ	= ratio of specific heats
δ	= shock generator angle
δ_{sh}	= shock standoff distance
δ_c	= conical shock angle
θ	= angular position on cowl forebody
θ_c	= cone half angle
μ	= dynamic viscosity
ξ, η, ζ	= curvilinear coordinates
ρ	= density
ψ	= stream function
γ	= ratio of specific heats
τ	= viscous shear stress

Subscripts

c	= inviscid sharp cone conditions
e	= local conditions at the boundary layer edge
i	= ith specie
o	= stagnation point conditions
w	= wall conditions
∞	= freestream conditions

Chapter 1

INTRODUCTION

There is a renewed interest in the hypersonic flow regime after a gap of over a decade primarily because of the proposed National Aero-Space Plane. This hypersonic aircraft is to be powered by an airbreathing engine which should be very closely integrated with the airframe to avoid severe drag penalties. The whole forebody of the vehicle is used to precompress the airflow before it enters the engine inlet. The air is further compressed inside the inlets and the supersonic combustion takes place inside the scramjet combustor. The burned gases are expanded through the nozzles as well as on the aft portion of the undersurface. Integrating the airframe with the propulsion system for the hypersonic aircraft makes the traditional wind tunnel guided design not only difficult but very expensive. However, due to recent advances in computer architecture and efficient algorithm, it is now possible to solve more and more complex problems numerically. The Computational Fluid Dynamics (CFD) has emerged as an extremely valuable engineering tool in aerodynamic analysis and design. A wide variety of very complicated flows are being simulated by computers. At the NASA Langley Research Center, a great deal of numerical and experimental efforts are directed toward a better understanding of the complex flow field in different regions of the Aero-Space Plane. Numerical modeling of the flow field has proven to be a valuable tool for getting better insight

into the complex nature of these flows. This approach in conjunction with ongoing experimental program provides an effective analysis capability.

The forebody geometry is relatively simple and fixed and can be modeled by long slender bodies of revolution with blunted nose. A reusable vehicle will probably not have an ablative surface. Thus, the forebody flow field analysis appears fairly straight forward. But, in addition to the prediction of wall properties, such as skin friction, heat transfer and pressure, an accurate estimate must be made of the entire flow field in order to predict the mass and the momentum flux entering the inlet. The thickness of the boundary layer at the inlet face is important for predicting the inlet performance. It is, therefore, necessary to incorporate realistic geometrical modeling and flow conditions in the analysis of the forebody. One of the geometrical features which can have significant effect on the entire flow field is the nose bluntness. In hypersonic flows over slender bodies, the influence of nose bluntness can be significant for hundreds of nose dimensions downstream. Thus, it is important to develop efficient and reliable methods for predicting the effects of blunt nose on the entire flow field.

In most studies involving flow past slender bodies, it is assumed that the leading edge is infinitely sharp. In practice, it is impossible to manufacture a body with zero leading edge thickness as well as all bodies must have some finite bluntness in order to sustain the heat generated at hypersonic speeds. The leading edge heat transfer can be decreased by increasing the leading edge thickness. However, this results in a drastic increase in drag. With the advancement in material technology, it is possible to reduce the leading edge thickness without encountering intolerable heating rates in the vicinity of the nose. But the extent to which this bluntness influences the development of flow downstream is not known precisely for hypersonic flows. In general, such a calculation is very difficult because of the various competing effects such as pressure interaction, vorticity interaction, and curvature

parameters. To calculate the flow over blunted slender bodies, two sets of equations are utilized in the present investigation. For the nose section, the use of full Navier-Stokes equations is necessary due to the presence of the subsonic region; but slightly downstream of the nose region on the body, the flow becomes predominantly supersonic and the space marching parabolized Navier-Stokes equations can be used. A shock fitting algorithm for both the Navier-Stokes and parabolized Navier-Stokes equation is used. The real gas effects which might be present at hypersonic speeds are also considered.

Another impact that a blunt leading edge can have is on the inlet flow field. The optimum propulsion efficiency occurs when the forebody shock impinges on the engine cowl lip so that all the precompressed air is captured by the inlet. Depending upon the Mach number and the angle of attack the forebody shock can interact with the shock from the compression surface leading edges of the inlet. This interaction results in a very complex flow field and can result in large increase in pressure and heat transfer over certain localized regions. The large temperature gradients cause thermal stresses which could result in structural failure. In order to relieve the influence of thermal stresses, some form of active cooling is needed. To determine the cooling requirements, pressure and heating rates on the body need to be predicted accurately. Such phenomena also occur on space shuttle and other high speed vehicles at the point where the bow shock from the nose interacts with the wing leading-edge shock.

For accurate predictions of shock interference patterns and aerothermal loads, it is necessary to employ modern algorithms. The classical central difference numerical algorithms have less than desired resolution in the shock regions. In recent years, the upwind biased algorithms have become a popular alternative to the central difference schemes. These methods model the characteristic nature of the equation. The information at each grid point is obtained from the direction dictated

by the characteristic theory. The particular upwind method used here is the flux vector splitting due to van Leer which is used to solve the compressible Navier-Stokes equations with upwind biased differencing for the inviscid terms and central difference approximation for the viscous terms. The cowl forebody is modeled by a cylindrically blunted wedge of infinite width which allows a two-dimensional analysis of the flow field. An adaptive grid technique is used to properly resolve the flow field features and to accurately predict the surface heat transfer. The use of full Navier-Stokes equations is made on the cowl forebody and the thin layer Navier-Stokes equations are suitably modified for the space marching on the cowl afterbody. For the forebody shock interaction with the inlet sidewall, the compression surface leading edge is modeled by a swept wedge. In this case, the line of intersection of the forebody shock and the compression surface leading edge shock is curved making the flow field fully three-dimensional.

The objective of the present investigation is to develop an accurate solution procedure for determining the zone of influence of the leading edge thickness and to calculate the shock interference phenomenon with an accurate prediction of aerothermal loads on the blunt leading edges of slender bodies in viscous hypersonic flows. The high temperature effects which might be present at hypersonic speeds are accounted for by using an equilibrium gas model. The influence of entropy layer on the leading edge effects is also addressed. To accurately predict the shock interactions, the importance of a suitable grid is discussed. Two types of shock interference patterns are considered. The analyses ranges from a few simplified approaches to the solution of the combination of full Navier-Stokes and parabolized Navier-Stokes equations. The solution procedures are validated by comparing the present results with the available experimental and numerical data.

Chapter 2

LITERATURE SURVEY

In this chapter, the theoretical and analytical works carried out in the area of the effects of nose bluntness and shock-shock interactions are reviewed. The effect of blunt leading edge on flat plates and slender bodies is considered first and then the available work on shock-shock interactions is reviewed.

Early studies on the effects of nose blunting are summarized in classical books on hypersonic flows [1] - [5]*. They deal with approximate approaches such as the Newtonian theory, small disturbance theory, and constant density assumptions. Some empirical correlations have been developed on the basis of experimental data. But these approaches have limited validity and are very restrictive in nature.

Some specific studies of nose bluntness effects have been carried out for flat plates [6] - [10]. Hammitt and Bogdonoff [6] carried out experiments on blunted flat plates. A wide range of Mach number and Reynolds number were considered for various leading edge thicknesses. It was found that the flow over a flat plate with thick leading edge is essentially inviscid but viscosity plays an important role for thin leading edges. Also the effect of leading edge is felt for several thousand leading edge thicknesses downstream. Vas et al. [7] did an experimental study of the shock shape and surface pressure distribution about thick two-dimensional and axisymmetric bodies. The shock shape was found to be parabolic about flat plates

*The numbers in brackets indicate references.

with flat and cylindrical leading edge for $\frac{x}{R_n} < 10$. The pressures on the cylindrical sections can be predicted reasonably well by the Newtonian theory and the pressure coefficient ratio on the surface was found to be higher for two-dimensional bodies than for axially symmetric bodies. Allegere and Bisch [8] studied the effects of the angle of attack and leading edge on the flow about flat plates at Mach 18. The Reynolds number considered were 70-15000. It was found that the wall pressure increases with increasing leading edge thickness and angle of attack.

Cheng et al. [9] did a theoretical and experimental study of the leading edge bluntness and boundary layer displacement effects for the situation where both effects are equally important. The interaction of the two effects was treated theoretically by extending the basic shock layer concept. In the outer inviscid flow, a model consisting of a detached shock wave and an entropy layer was introduced to account for the bluntness. In the boundary layer the approximate solution was found to be governed by the local flat plate similarity theory. Bradfield et al. [10] conducted an experimental investigation to ascertain the effects of leading edge bluntness on the laminar boundary layer of a flat plate. It was demonstrated that the effect of the leading edge bluntness is an important consideration in the formulation and development of the boundary layer on a flat plate at supersonic speeds. The ratio of leading edge thickness to the value of boundary layer thickness at the measuring stations may be taken as criterion of the magnitude of this effect.

The flow field over slender bodies has been studied by various investigators. However, most of these studies are limited to rarefied flows [11] - [14] and/or to a very small nose bluntness [15] - [28]. Vas and Sierchio [11] performed an experimental study to determine the downstream effects of nose bluntness in hypersonic rarefied flows. The study was carried out at Mach 25 and freestream Reynolds number of 11000 per inch on 5° half angle sharp and blunted cones. Significant differences between the sharp and blunted bodies were noted on the surface and

flow quantities. McCroskey et al. [12] studied the leading edge flows over slender bodies in rarefied hypersonic flows. The primary attention was directed upstream of the merged layer. Based on the experimental data it was established that there is a competition between the displacement and merging effects in determining the surface pressure and heat flux. Feik et al. [13] conducted experimental studies on cones of 5° , 10° and 15° half angles at Mach 25 and Reynolds number 7000-15000 per inch. The effect of bluntness within the merged region and the flow downstream of the merged region was studied. Significant effects of the nose bluntness were found on the location of merging, the location of shock wave after the merging, and both the surface pressure and heat transfer within and considerably downstream of the merged region.

Vogenitz et al. [14] conducted numerical experiments on rarefied flows of a monoatomic gas about slender cones and flat plates at Mach 10 and 25; cone half angle ranged from 3° - 15° . The gas model was composed of hard sphere model which accommodates completely to solid surface and reflect diffusively. Leading edge flows on sharp slender cone was found to differ substantially from that on the flat plates. Burke and Curtis [15] measured static pressure distribution on the surface of a blunted 7.5 degree half angle cone for Mach 8-18 and Reynolds number of 1×10^6 per foot. It was found that the position of minimum pressure and the rate of pressure recovery depends upon cone angle. Bertram [16] examined the aerodynamic effect of nose blunting on a 10° cone, the blunting consisted of a plane cut normal to cone axis. The shock shape was found to have an inflection at about 40-60 nose radii from the nose and the surface pressure reaches a minimum. For lower values of Reynolds number, the surface pressure data were not affected to any considerable extent by viscous effects. Dewey [17] studied the slender vehicles operating in high-altitude, high-temperature environment. The study showed that a regime of significant practical interest exists in which the effects of leading edge

bluntness and viscous interaction are of comparable magnitude; the lift and drag depend to a large extent on the relative effect of the leading edge bluntness and boundary layer displacement.

Cheng and Pallone [18] investigated the inviscid leading edge effects in hypersonic flow on the basis of small perturbation theory. The results were obtained under the assumption of one dimensional adiabatic flow of an ideal gas and infinite shock strength. Various correlations for surface pressure and shock shape were developed for several values of γ . Lees and Kubota [19] analyzed inviscid hypersonic flow over blunt nosed slender bodies. Based on similarity theory, correlations for shock shape and surface pressure for slender bodies were developed. It was found that the shape of the bow shock wave, flow field and wall quantities are dominated by the blunt nose over a downstream distance many times greater than the characteristic nose dimension. Cheng [20], on the basis of small perturbation theory, developed the laws of similitude for hypersonic, inviscid, real gas flow field over blunted flat plates, cones and wedges. The results for real gas flow over a cone at zero yaw agreed with the laws of similitude developed. Also the thickness of the singular region near the surface of a blunt region was estimated and its effects on the pressure prediction was determined. Lees [21] calculated laminar heat transfer over blunt nose bodies at hypersonic flight speeds for limiting cases of thermodynamic equilibrium and diffusion as controlling factors for the rate of heat transfer. De Jarnette and Davis [22] developed a simplified method for calculating the laminar heat transfer over blunt bodies with only freestream Mach number and the ratio of specific heat as input parameters. The viscous problem was simplified by using the axisymmetric analog for three-dimensional boundary layers in conjunction with the Lees' laminar heating rate relation. The results for 15° and 20° cones at freestream Mach number of 10.6, for various angles of attack, showed good agreement with experimental data.

In recent years, certain numerical and experimental efforts have been directed to investigate the effects of nose bluntness on slender bodies [23] - [28]. Stetson [23] conducted an experimental study on blunted cones to determine the leading edge effects on the boundary layer transition. Based upon the results it was concluded that transition depends upon the 'entropy swallowing distance' which in turn is a strong function of the leading edge thickness. Nowak [24] did an experimental investigation at Mach 6.7 to determine the effects of Reynolds number, angle of attack and the nose shape on aerothermal environment of a 12.4° half angle cone. Three nose tip configurations were tested on the cone; a three inch radius, a one inch radius and a sharp tip. Heating rate distribution, surface pressure distribution, shock shape and shock layer profiles were measured and compared with predictions. Surface pressure and heating rates when normalized by their stagnation values were found to be independent of the freestream Reynolds number. With the increasing bluntness, the surface pressure took longer distance to recover from the nose overexpansion.

Zoby and Simmonds [25] did engineering calculations over hyperboloids, paraboloids, ellipsoids and sphere-cones. The heating and constant or variable entropy conditions were coupled with an approximate inviscid code. Results were obtained for various angles of attack and good comparison with experimental data was obtained. Thompson et al. [26] did a numerical study to assess the applicability of viscous shock layer code and various engineering codes for aerothermal predictions over slender spherically blunted cones. The numerical results were compared with experimental data from flight and ground based tests. The effects of nose blunting and angle of attack on drag and heat transfer were illustrated. Gupta et al. [27] obtained numerical solution for hypersonic laminar and turbulent flows over slender bodies. The results were obtained from the viscous shock layer equations at Mach 8-15 for sphere-cones and hyperboloids. Detailed comparisons were made with

other numerical results and experimental data to assess the accuracy of viscous shock layer solutions. Zoby et al. [28] conducted a parametric study of laminar nonequilibrium heat transfer on slender vehicles. The study included the variation of altitude-velocity conditions, cone half angle and nose bluntness. The effect of wall catalycity to reduce the heating rates was also investigated.

A great deal of work is currently underway on shock-shock interactions at various places due to the practical significance of the phenomenon in complex high speed flows. In relation to the National Aero-Space Plane, special attention is directed to study the shock-shock interaction at the cowl plate and the inlet sidewalls of the scramjet engine inlet. In order to avoid the structural failure, it is very crucial to calculate the thermal stresses arising in the scramjet inlet. To have an optimum design in terms of structural strength and cooling requirements, accurate calculations of surface pressure and heating rates are of utmost importance. Due to the complexity of the problem, most of the earlier works are either experimental or of highly simplified model where empirical inputs have been used. The effects of Mach number, Reynolds number, impinging shock strength and sweep angle have been studied on surface pressure and heat transfer over flat plates, cylinders, hemispheres and various leading edge geometries. The experimental data has unusually large scatter due to difficulties in making accurate measurements over the narrow zone where the impingement occurs. Until recently, the numerical calculations were virtually nonexistent. With the rapid advancement in computer hardware and improved algorithms, it is now possible to compute such complex flow field accurately.

Teterin [29] conducted experimental study on the effect of incident shock on the flow field and force effects on the cylinder. The cylinder was mounted on a 25° wedge. In order to isolate the effects of shock-shock interaction from separation, the separation zone was eliminated by means of a fillet. Schlieren pictures were obtained and the pressure distribution was measured. Sukovstin and Shestova [30]

studied effects of bow shock impingement on a body located in the influence zone of primary body (creating the bow shock) . An approximate integral method was presented and results were obtained for Mach 3-20.

Edney [31] in 1968 conducted a detailed study of the shock-shock interaction phenomenon at Aeronautical Research Institute of Sweden. Three basic models, a 30 mm diameter hemisphere/cylinder, a 30 mm diameter flat faced cylinder, and a 30° half angle cone/cylinder with 5 mm nose radius and 15 mm base radius were tested at Mach numbers of 4.6 and 7.0. Edney was the first to classify these interactions into six basic patterns, which can occur when an extraneous shock interacts with the bow shock of a blunt body. The interactions could result in shock-boundary layer interaction (Type I, II, V), shear layers (Type III), supersonic jet (Type IV) or expansion fan-boundary layer interactions (Type VI). All of these interactions, except for Type VI, increase the surface pressure and heat transfer over a localized zone. The Type IV interaction is the most severe one, producing largest increase in pressure and heat transfer. The type VI interaction is the only one that causes the heat transfer and pressure to decrease due to production of an expansion fan.

Keyes and Hains [32] continued the work of Edney for higher Mach numbers, Reynolds numbers and various values of specific heat. All six types of interaction were studied. The planar shock waves were allowed to impinge upon the bow shock surrounding swept fins, hemisphere and wedges. The impinging shock wave was generated by a wedge. Heat transfer measurements were obtained using a phase change paint technique. Peak heating rates of 17 times and peak pressure of eight times the unimpinged stagnation point values were measured. The results showed that pressure and heating rates are strongly affected by Mach number, specific heat, impinging shock strength and geometry.

Craig and Ortwerth [33] investigated the leading edge shock impingement

problem at Mach 15 in the Airforce Applied Physics Laboratory. This study was carried out to determine the pressure and temperature amplifications on the leading edge of hypersonic inlets. The peak heat transfer amplification on leading edge was found to be less than five. In this study the spacing between the pressure taps and the thin film thermometer was too large to give adequate resolution. The data obtained cannot be used due to lack of resolution and unavailability of information on the position and strength of the impinging shock. Wieting [34] conducted an experimental study on the shock wave interference over a cylindrical leading edge at Mach 6.3, 6.5 and 8.0. The model consisted of a three inch diameter cylinder. The results were presented for heat transfer and pressure distribution for a two-dimensional shock wave interference on a cylinder. This was considered to be representative of the cowl leading edge of the scramjet inlet. The local heat transfer rate and pressure were amplified up to ten times the unimpinged stagnation point values.

Several semi-empirical approaches have been proposed to theoretically predict the peak heating and pressure [35] - [40] but they rely on several empirical inputs which must be known apriori. Morris and Keyes [35] developed a computer program based on semi-empirical correlations to calculate the peak pressure and heating rates for all six types of interactions. The correlations require various inputs such as width of impinging jet and length of transmitted shock. In general this information is not known apriori. Crawford [36] improved upon the Edney's graphical approach for predicating peak pressure and heat transfer by plotting a family of pressure deflection curves with the pressure ratio on a logarithmic scale and flow deflection on linear scale thus eliminating the need for iterations as Mach number is uniquely defined on this set of coordinates. Keyes and Morris [37] developed correlations for peak pressure and heating for shock/boundary layer interaction and shear layer attachments for two-and three-dimensional interactions. The Mach number

considered were 6 and 20 over a freestream Reynolds number range from 3.3-25.6 million per meter and specific heat ratio of 1.4 and 1.67. The shock generator angle was varied from 5° – 25° . Bramlette [38] developed an approximate method for computing pressure for Type III and IV interference. The peak pressure obtained for various shock generator angles showed good comparison with the experimental data. Markarian [39] studied the problem of aerodynamic heating caused by shock wave and boundary layer interactions. It was found that heating rates for this type of interaction are significantly higher than normally predicted values; also the heating rates were found to be higher for laminar interaction than turbulent interaction. Some empirical correlations were developed to predict the heating based on the inviscid pressure rise across the interaction. Bertin et al. [40] studied shock interference pattern for delta wing orbiters. The surface pressure and heat transfer distribution in the interaction perturbed region were obtained for velocities from 1167 m/s to 7610 m/s. At high velocities, the Type IV interaction was found to exist for wing leading edge sweep as low as 27° . For this case, no locally severe heating rates were obtained.

There are very few numerical studies available on the shock-shock interaction due to the complexity of the problem. Tannehill et al. [41,42] presented the first successful numerical simulation of the interaction problem based on the explicit MacCormack method. White [43] solved this problem using the Reynolds-averaged Navier-Stokes equations (based on an implicit finite-volume method) and obtained results for Mach 6.0. Klopfer [44] conducted an extensive study for various Mach numbers using the second-order implicit TVD algorithm but the results for the peak heat transfer for the Type IV interaction were off by a factor of about 2.25, although the pressure was in close agreement with the experimental results. Perry et al. [45] used the Roe scheme to solve the Type IV interactions but did not give any heat transfer results. Moon et al. [46], in a recent paper, provided the results

for the Type III interference pattern. The study indicated that the flow for this type of interaction in the impingement region is turbulent rather than laminar.

Most of the studies mentioned earlier to study the shock-shock interaction are two-dimensional in nature except [32], thus cannot be used for interaction on swept inlet sidewalls. The only related numerical study on three-dimensional interaction was carried out by Holst et al. [47]. They solved the three-dimensional shock-shock interaction on an infinite cylinder using the explicit MacCormack scheme. The viscosity was assumed an order of magnitude higher than the actual viscosity to physically thicken the boundary layer and a very coarse grid was employed. The resulting solution was at best qualitative in nature.

The literature survey clearly indicates the need for an additional extensive study in this important field of current interest.

Chapter 3

DOWNSTREAM EFFECTS OF NOSE BLUNTNESS

In this chapter the effects of nose bluntness on the flow field and wall quantities over forebody of a generic hypersonic plane are considered. The calculation of hypersonic viscous flow field past long slender axisymmetric blunt bodies is of prime interest to the designer of aerospace vehicles. A wide variety of flow conditions are encountered during the trans-atmospheric flight of these vehicles. As mentioned previously, the forebody of these vehicles must have finite thickness in order to sustain the pressure and heating rates encountered at hypersonic speeds. The forebody is modeled by spherically blunted cones and ogives. The physical model for hypersonic flow past a blunt-nosed slender body is shown in Fig. 3.1. The relative positions of boundary, entropy, and shock layers are indicated in the figure. The first physical problem considered is the flow past a blunt nosed slender cone. Numerical results have been obtained by employing a combination of a Navier-Stokes code and a parabolized Navier-Stokes code. These are discussed here briefly and some specific results are presented in Chap. 5.

In the present study, 5° , 10° , and 20° half-angle cones are selected first with spherical nose tip as shown in Fig. 3.1. Three nose tips with radius of 0.0025m, 0.025m and 0.05m are considered, with the smallest nose radius tip approximating the sharp tip. Blunting was accomplished by keeping the cone angle fixed and

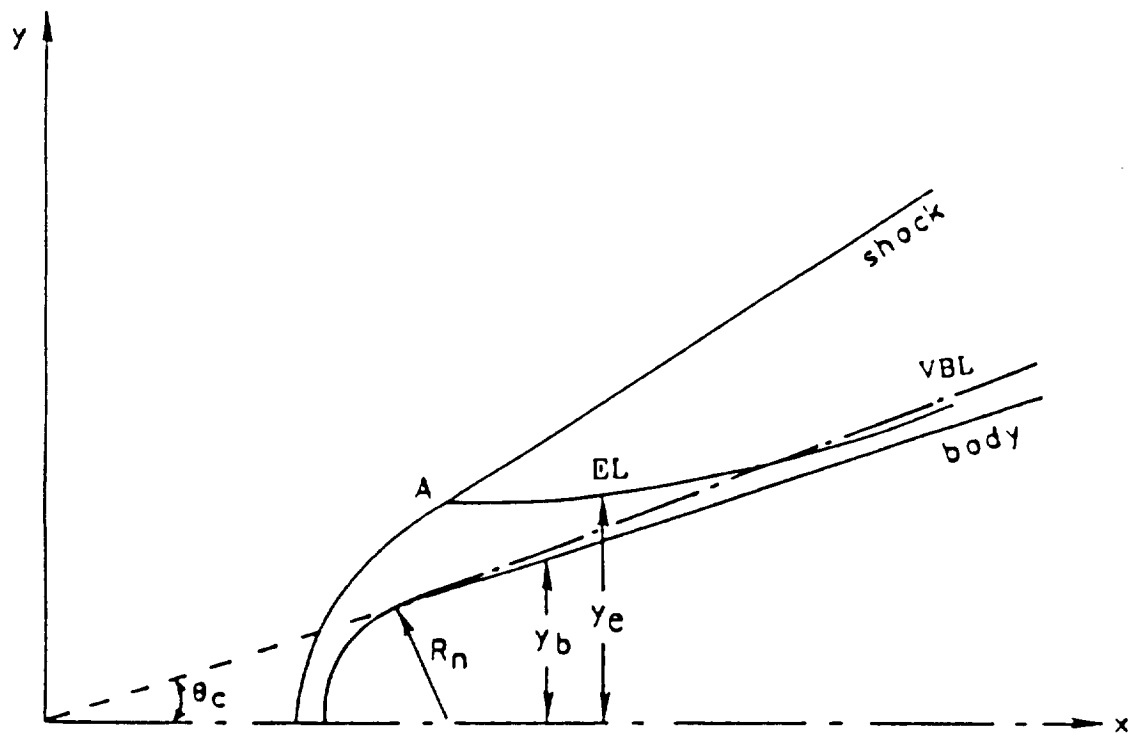


Fig. 3.1 Physical model for hypersonic flow past a blunted cone.

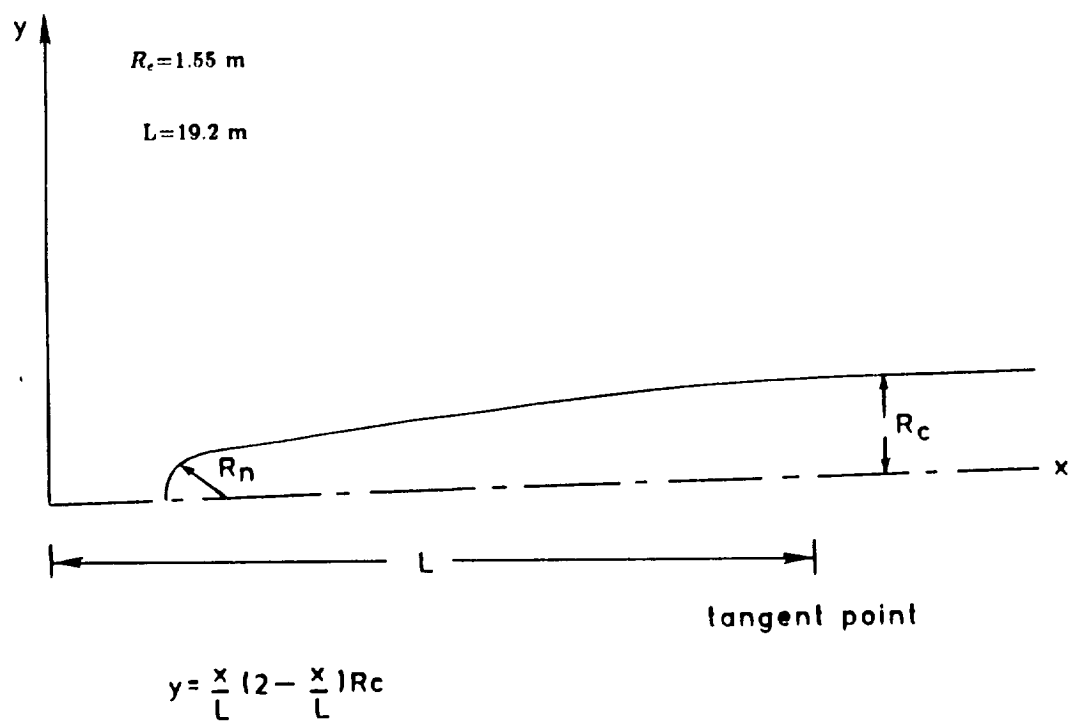


Fig. 3.2 Physical model for hypersonic flow past an ogive.

increasing the nose radius. The bluntness effects are determined by comparing the solutions obtained from the blunted tips with that obtained from the sharp tip. As shown in Fig. 3.1, the origin of the coordinate system is at the virtual tip of the sharp cone with x axis along the symmetry line and y axis normal to it. Due to symmetry of the flow field at zero angle of attack, only half of the flow is calculated. The second geometry considered is a generic forebody (Fig. 3.2) with three nose tips of same radii as the cone. Here again the smallest nose radius approximates the sharp tip body.

3.1 Entropy Layer

Nose bluntness at hypersonic speed causes shock wave to be detached and curved in the nose region. The entropy of the flow increases across a shock wave, the stronger the shock wave, the larger the entropy increase. So the streamline passing through the nearly normal portion of the shock will have larger entropy increase than a streamline passing through the weaker portion of the shock. This change in entropy production in the nose region generates a layer of flow with entropy gradient, known as the entropy layer, which "influences" the development of the boundary layer in two different ways. First, it causes a continuous change of the flow properties at the outer edge of the boundary layer in the streamwise direction and second, it produces a velocity and pressure gradient at the outer edge. These external gradients invalidate the classical boundary layer approach. However Ferri [48] pointed out that these gradients are important when the vorticity of the inviscid flow is of the same order as that of the boundary layer. These conditions may exist when the Reynolds number is low and the Mach number is high. The thickness of the entropy layer is a function of the leading edge bluntness; even a small leading edge thickness generates an entropy layer which influences the local flow conditions for a large distance downstream. For some distance downstream of

the blunt nose the boundary layer grows inside the entropy layer which eventually is swallowed by the boundary layer in the case of flow past blunted cones. This distance is called the entropy swallowing distance. For conical flows, the entropy swallowing distance is defined [23] as "the location at the cone frustum where fluid, which has gone through the strong portion of the bow shock, has been swallowed by the boundary layer." This is by no means a precise definition as it depends upon the shock shape, boundary layer assumptions, and definition of the entropy layer thickness. The presence of the entropy layer has an important effect on the aerodynamic heating predication.

For hypersonic flows over a blunted slender cone, the curvature of the shock produces the entropy layer as shown in Fig. 3.1. Once the shock attains conical shape, it is no longer curved and hence no more entropy gradient is produced. The thickness of the entropy layer decreases as it moves downstream on the body and eventually it is swallowed by the boundary layer. The entropy effects in the boundary layer vanish asymptotically further downstream.

To calculate the entropy swallowing distance without calculating the flow field, certain assumptions regarding the shock shape and the boundary layer have to be made. Several investigators have attempted to approximate the shock shape for slightly blunted cones. Klaimson [49] has given one of the most accurate, yet simple, expression for the shock shape as

$$\bar{y} = 1.424 \cos \theta_c \left[C_{DT}^{0.5} \left(\frac{\bar{x}}{\cos \theta_c} \right) \right]^{0.46} \quad (3.1)$$

For hypersonic speeds, the drag on the hemispherical nose can be calculated as

$$C_{DT} = 2 - \cos^2 \theta_c \quad (3.2)$$

A comparison of this shock shape with numerically calculated shape has been shown to give excellent agreement [49] within the region of interest. The value of \bar{y} , where

the shock approaches the conical angle, is given by

$$\bar{y}_c = \cos \theta_c \left[0.984 C_{DT} \left(\frac{1}{\sin^2 \delta_c} - 1 \right) \right]^{0.426} \quad (3.3)$$

The angle δ_c can be obtained from the relation

$$M_\infty \sin \delta_c = 4 + 1.01 (M_\infty \sin \theta_c - 3.43) \quad (3.4)$$

With the known value of \bar{y}_c , the entropy swallowing distance, \bar{S}_c , can be approximated as [50]

$$\frac{\bar{S}_c}{Re_\infty^{\frac{1}{3}}} = \left[\frac{1.5 \bar{y}_c^4 M_\infty}{P_c / P_\infty f^2(\eta_c) 4 M_c \sin^2 \theta_c} \right]^{\frac{1}{3}} \quad (3.5)$$

In Eq. (3.5), $f(\eta)$ is the transformed stream function defined as

$$\psi(S, \eta) = (2\bar{S})^{\frac{1}{2}} f(\eta), \quad f' = \frac{u}{U_e} \quad (3.6)$$

where

$$\eta = \frac{\rho_e U_e R_n}{(2\bar{S})^{\frac{1}{2}}} \int_0^\eta \frac{\rho}{\rho_e} dy$$

$$\bar{S} = \int_0^S \rho_e U_e \mu_e R_n^2 dS$$

In the present study, entropy swallowing distance is calculated by considering the mass flow rate. The entropy layer thickness is calculated in the downstream region, and the point where the entropy layer thickness becomes equal to the boundary layer thickness is termed as the entropy swallowing point. To estimate the thickness of the entropy layer, its edge is defined as the streamline that passes through the point A (Fig. 3.1) at which the shock attains the conical angle as given by Eq. (3.4). Most of the entropy changes occur before this point. The rate of mass flow in the entropy layer is given by

$$\dot{m} = 2\pi \int_{y_b}^{y_e} \rho u y dy \quad (3.7)$$

At point A, the mass flow rate is expressed as

$$\dot{m}_A = \pi y_e^2 \rho_\infty U_\infty \quad (3.8)$$

Since the mass flow rate through the entropy layer is constant, $y_e(x)$ can be calculated using Eqs. (3.7) and (3.8). At point A, y_e is same as y_c given by Eq. (3.3)

The entropy swallowing distances calculated using present approach were compared with the results of Rotta [50] for various nose bluntness and Reynolds number. As will be shown later the present approach for calculating the entropy swallowing distance agrees qualitatively with the merging distance for skin friction, surface pressure, wall heat transfer and shock shape. The theoretical calculations of Rotta assume that the pressure on the conical portion of the body is constant and, therefore, the overexpansion and recompression on the shoulder are neglected. This causes the overestimation of the entropy swallowing distance. For small bluntness, the overexpansion can be neglected. Thus, Rotta's results are valid only for very small values of nose bluntness.

3.2 Governing Equations

To calculate the flow over blunted slender bodies, two sets of equations are utilized. For the nose section, the use of full Navier-Stokes equations is necessary due to the presence of the subsonic region; but slightly downstream of the nose region on the body, the flow becomes predominantly supersonic and the Navier-Stokes equations are simplified for space marching. The Navier-Stokes equations without body force and external heat addition can be written in nondimensional, strong conservation form as [51]

$$\frac{\partial U}{\partial t} + \frac{\partial(E - E_v)}{\partial x} + \frac{\partial(F - F_v)}{\partial y} + \frac{\partial(G - G_v)}{\partial z} = 0 \quad (3.9)$$

where

$$U = \{\rho, \rho u, \rho v, \rho w, \rho e_t\}^T$$

$$E = \{\rho u, \rho u^2 + p, \rho uv, \rho uw, (\rho e_t + p)u\}^T$$

$$E_v = \{0, \sigma_{xx}, \tau_{xy}, \tau_{xz}, \sigma_{xx}u + \tau_{xy}v + \tau_{xz}w + q_x\}^T$$

$$F = \{\rho v, \rho vu, \rho v^2 + p, \rho vw, (\rho e_t + p)v\}^T$$

$$F_v = \{0, \tau_{xy}, \sigma_{yy}, \tau_{yz}, \tau_{xy}u + \sigma_{yy}v + \tau_{yz}w + q_y\}^T$$

$$G = \{\rho w, \rho wu, \rho wv, \rho w^2 + p, (\rho e_t + p)w\}^T$$

$$G_v = \{0, \tau_{xz}, \tau_{yz}, \sigma_{zz}, \tau_{xz}u + \tau_{yz}v + \sigma_{zz}w + q_z\}^T$$

$$\sigma_{xx} = \frac{2\mu}{3Re} \left(2 \frac{\partial u}{\partial x} - \frac{\partial v}{\partial y} - \frac{\partial w}{\partial z} \right)$$

$$\sigma_{yy} = \frac{2\mu}{3Re} \left(2 \frac{\partial v}{\partial y} - \frac{\partial u}{\partial x} - \frac{\partial w}{\partial z} \right)$$

$$\sigma_{zz} = \frac{2\mu}{3Re} \left(2 \frac{\partial w}{\partial z} - \frac{\partial u}{\partial x} - \frac{\partial v}{\partial y} \right)$$

$$\tau_{xy} = \frac{\mu}{Re} \left[\frac{\partial u}{\partial y} + \frac{\partial v}{\partial x} \right]$$

$$\tau_{xz} = \frac{\mu}{Re} \left[\frac{\partial u}{\partial z} + \frac{\partial w}{\partial x} \right]$$

$$\tau_{yz} = \frac{\mu}{Re} \left[\frac{\partial v}{\partial z} + \frac{\partial w}{\partial y} \right]$$

$$q_x = \frac{\mu}{M_\infty^2 Re_l Pr (\gamma - 1)} \frac{\partial T}{\partial x}$$

$$q_y = \frac{\mu}{M_\infty^2 Re_l Pr (\gamma - 1)} \frac{\partial T}{\partial y}$$

$$q_z = \frac{\mu}{M_\infty^2 Re_l Pr (\gamma - 1)} \frac{\partial T}{\partial z}$$

and

$$e_t = e + \frac{u^2 + v^2 + w^2}{2} \quad (3.10)$$

$$p = (\gamma - 1)\rho e \quad (3.11)$$

These equations are nondimensionalized with respect to the freestream values. The coefficient of viscosity μ is obtained using the Sutherland's law. For perfect gas calculations, Prandtl number is taken as 0.72.

For the spherical nose region of the body, the flow is analyzed by the code SOFIA [52]. It solves complete Navier-Stokes equations using an explicit, finite volume, alternating two step scheme and uses local time stepping to accelerate the

convergence to steady state. It also incorporates time dependent grid adaptation to properly resolve the flow gradients without increasing the grid points. Once the flow field is obtained over the nose section, it is used as initial plane solution to initialize the parabolized Navier-Stokes equations. In the present investigation, a parabolized Navier-Stokes code developed by Vigneron et al. [53] and subsequently modified by Gnoffo [54] is used for analyzing the downstream flow over the bodies. Parabolized Navier-Stokes (PNS) equations are subset of the complete Navier-Stokes equations and can be used to predict complex three-dimensional, steady, supersonic, viscous flow fields. These equations can be solved using a space marching technique as opposed to the time marching, which is usually employed for the Navier-Stokes equations. They are valid in both viscous and inviscid regions and thus unlike boundary layer equations no special effort is needed for viscous/inviscid interactions. They can be obtained by

- (i) Neglecting unsteady terms
- (ii) Neglecting streamwise viscous diffusion terms
- (iii) Modifying the streamwise flux to permit the stable time like marching of the equations from the initial data plane.

For these equations to be valid, the flow in the inviscid region should be supersonic and streamwise velocity component should be positive. Thus, these equations fail in the presence of streamwise separation, although they are valid in the region of crossflow separation. The streamwise pressure gradient needs special treatment as will be explained later.

The following two independent variable transformations are applied to allow for conical effects and stretching between the body and shock.

$$a = x \qquad b = \frac{y}{x} \qquad c = \frac{z}{x} \qquad (3.12)$$

$$\xi = a \qquad \eta = \eta(a, b, c) \qquad \zeta = \zeta(b, c) \qquad (3.13)$$

Upon combining Eqs. (3.9), (3.12) and (3.13), neglecting unsteady terms and viscous derivatives in ξ direction, the PNS equations are expressed as [53]

$$\frac{\partial E_1}{\partial \xi} + \frac{\partial F_1}{\partial \eta} + \frac{\partial G_1}{\partial \zeta} = 0 \quad (3.14)$$

where

$$\begin{aligned} E_1 &= \frac{a^2 E}{J} \\ F_1 &= \frac{a}{J} \left[\left(a \frac{\partial \eta}{\partial a} - b \frac{\partial \eta}{\partial b} - c \frac{\partial \eta}{\partial c} \right) (E - E_v) \right. \\ &\quad \left. + \frac{\partial \eta}{\partial b} (F - F_v) + \frac{\partial \eta}{\partial c} (G - G_v) \right] \\ G_1 &= \frac{a}{J} \left[\left(-b \frac{\partial \zeta}{\partial b} - c \frac{\partial \zeta}{\partial c} \right) (E - E_v) \right. \\ &\quad \left. + \frac{\partial \zeta}{\partial b} (F - F_v) + \frac{\partial \zeta}{\partial c} (G - G_v) \right] \\ J &= \frac{\partial(\eta, \zeta)}{\partial(b, c)} \end{aligned}$$

The presence of streamwise pressure gradient term allows for upstream propagation of information in the subsonic regions of the flow; thus, the equations are not well posed for space marching method. Various remedies have been proposed to overcome this problem, the most successful one was proposed by Vigneron et al. [53]. In this approach, a fraction of the pressure gradient term is retained in the subsonic region and the remainder is either omitted or is evaluated explicitly using the backward differencing technique. Thus the term E_1 is split as

$$E_1 = E_1^* + P \quad (3.15)$$

$$E_1^* = \{\rho u, \rho u^2 + \omega p, \rho uv, \rho uw, (\rho e_t + p)u\}^T$$

$$P = \{0, (1 - \omega)p, 0, 0, 0\}^T$$

This treatment of the pressure gradient allows for stable marching scheme without encountering departure solutions. An eigen value analysis given in [53] indicates that for stability

$$\omega \leq \frac{\sigma \gamma M_\xi^2}{1 + (\gamma - 1) M_\xi^2} \quad (3.16)$$

where ω is the factor of safety; in the present calculations its value is taken as 0.9.

3.3 Method of Solution

The PNS equations are a mixed set of hyperbolic-parabolic equations in the streamwise direction. Equation(3.14) is solved with a finite difference method using the Beam and Warming algorithm [55]. It is an implicit, non-iterative algorithm with approximate factorization in Delta form. The Vigneron technique is used to suppress the numerical instabilities due to streamwise pressure gradients. Details of numerical procedure are available in [53]. For the sake of completeness only a brief description is given here.

Using the Euler implicit scheme, Eq.(3.14) can be written in the Delta form as

$$\begin{aligned} & \left[\frac{\partial E_1^*}{\partial U_1} + \Delta \xi \frac{\partial}{\partial \zeta} \left(\frac{\partial G_1}{\partial U_1} \right) \right] \left(\frac{\partial E_1^*}{\partial U_1} \right)^{-1} \left[\frac{\partial E_1^*}{\partial U_1} + \Delta \xi \frac{\partial}{\partial \eta} \left(\frac{\partial F_1}{\partial U_1} \right) \right] \Delta^i U_1 \\ & = -\Delta \xi \left(\frac{\partial F_1}{\partial \eta} + \frac{\partial G_1}{\partial \zeta} \right) - \Delta_e P \end{aligned} \quad (3.17)$$

where

$$U_1 = a^2 U / J, \Delta^i U_1 = U_1^{i+1} - U_1^i \text{ and } \Delta_e P = \Delta^{i-1} P$$

Since the vectors E_1 , F_1 , and G_1 are homogeneous functions of degree one in U , the conservative form of the governing equation is maintained. The viscosity μ is assumed independent of vector U and is a function of the position only. The cross derivative terms are neglected in the calculation of Jacobian. Equation(3.17) is solved in the following four steps.

$$\begin{aligned} & \left[\frac{\partial E_1^*}{\partial U_1} + \Delta \xi \frac{\partial}{\partial \zeta} \left(\frac{\partial G_1}{\partial U_1} \right) \right] \Delta^i \bar{U}_1 = RHS(3.17) \\ & \Delta \bar{U}_1 = \left[\frac{\partial E_1^*}{\partial U_1} \right] \Delta U_1^i \\ & \left[\frac{\partial E_1^*}{\partial U_1} + \Delta \xi \frac{\partial}{\partial \eta} \left(\frac{\partial F_1}{\partial U_1} \right) \right] \Delta^i U_1 = \Delta \bar{U}_1 \\ & U_1^{i+1} = U_1^i + \Delta U_1^i \end{aligned} \quad (3.18)$$

This procedure avoids the computation of inverse matrix and introduces two one-dimensional operators which are solved using the Thomas algorithm. In order

to damp the spurious oscillations, second order implicit and fourth order explicit damping terms are added. After adding the dissipation terms the truncation error of the algorithm is consistent with the first order Euler scheme.

Due to symmetry of the flow field, only one half of the flow field is computed. The generalized coordinates η and ζ are defined such that the computational plane has a square shape of side unity with uniform spacing in both directions. The outer boundary corresponds to the shock and the inner to the body. The grid points are clustered near the body to properly resolve the gradients. A typical grid is shown in Fig. 3.3.

At the body surface, no slip, zero pressure gradient and constant wall temperature conditions are imposed. At the outer boundary, shock fitting approach is used and the flow variables behind the shock are calculated by the Rankine-Hugoniot relations. At the plane of symmetry, reflecting conditions are used. As mentioned earlier, the initial plane solution to initiate the marching procedure is provided by the Navier-Stokes equations.

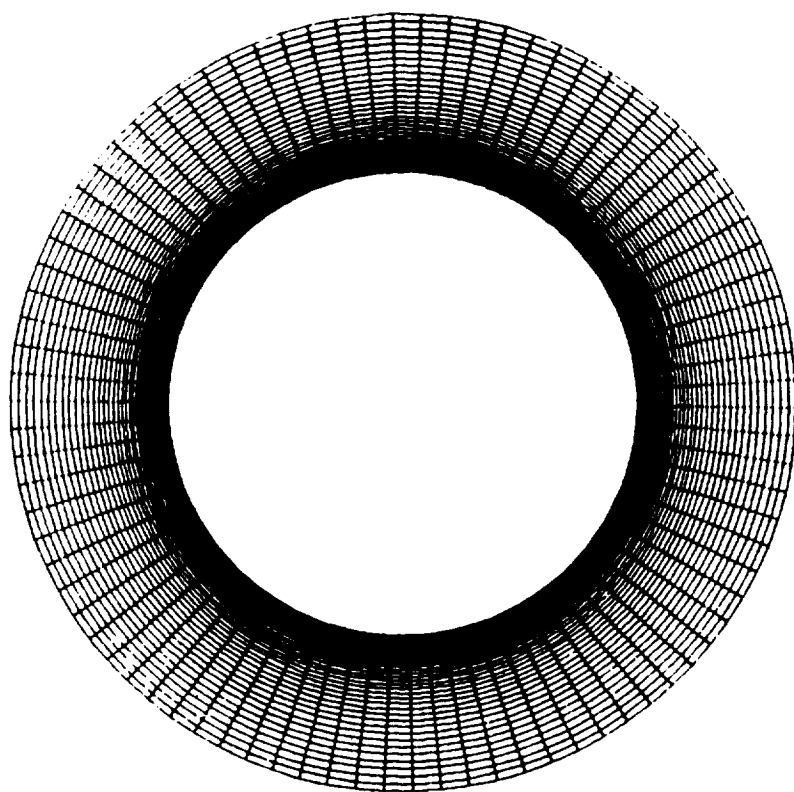


Fig. 3.3 Typical grid for finite difference calculations.

3.4 Equilibrium Chemistry

To include the real gas effects which might be present at hypersonic speeds, calculations are also made with equilibrium air chemistry. The equilibrium chemistry package developed in [56] is used in the analysis. In this model, complete thermodynamic equilibrium is assumed, in which the gas properties and concentration of atoms and molecules are identical with their equilibrium values appropriate to the local conditions. The rates of reaction are assumed very fast in comparison with the rate of diffusion. Here, the free energy minimization technique with the method of steepest descent is utilized. The mole fractions of the constituent species are calculated as a function of temperature and pressure. The assumption of equilibrium is made on the basis of physics of the problem. In the blunt body flows near the stagnation point, where the shock is nearly normal, the velocities are very low and temperature is very high. Consequently the flow attains equilibrium values prior to leaving the nose region. The particles crossing the bow shock farther from the axis experience higher velocities and lower temperature due to weaker shock, thus reducing the degree of non-equilibrium. On the after body past the sonic line, the flow experiences expansion thus increasing the velocity while reducing pressure and density, both of these effects try to quench the chemistry and produce frozen flows. Thus the afterbody flows can be calculated by using an effective value of γ determined from the mass concentration. Similar approaches have been taken previously by several authors [57,58]. The equilibrium chemistry option can easily be incorporated into a perfect gas code with equivalent γ approach where γ is now defined as the ratio of enthalpy to internal energy. Further details on implementation of the equilibrium chemistry model are given in Appendix A.

3.5 Validation

The PNS code was validated by comparing the present results with those calculated using the laminar theory with reference temperature concept [59]. For the same Reynolds number, the skin friction on a cone and a flat plate is related by

$$C_{fe,cone} = \sqrt{3}C_{fe,plate} \quad (3.19)$$

Consequently, the heat transfer coefficient is expressed as

$$C_{he,cone} = \frac{C_{fe,cone}}{2Pr^{\frac{2}{3}}} \quad (3.20)$$

The value of $C_{fe,plate}$ can be calculated from

$$C_{fe,plate} = \frac{0.664\sqrt{C^*}}{\sqrt{Re_{xe}}} \quad (3.21)$$

where Re_{xe} is the Reynolds number based upon the distance along the cone surface and the subscript e refers to the edge conditions. The surface flow along the cone is assumed to be constant, then ρ_e , U_e , and T_e can be calculated by inviscid supersonic cone theory [60]. The quantity C^* in Eq.(3.21) is the reference viscosity and is given by the Sutherland's law as

$$C^* = \left(\frac{T^*}{T_e}\right)^{0.5} \frac{T_e + K}{T^* + K}$$

where

$$K = 200^\circ R$$

and

$$\frac{T^*}{T_e} = 0.5 + 0.039M_e^2 + 0.5\frac{T_w}{T_e}$$

By using Eqs.(3.19)-(3.21), the theoretical values of $C_{fe,cone}$ and $C_{he,cone}$ can be calculated.

These results are compared with the numerically calculated values for sharp cone at $M_\infty = 10$ and are discussed in Chap. 5.

Chapter 4

EFFECTS OF SHOCK-SHOCK INTERACTIONS

In this chapter, the physical models used to calculate the two-and three-dimensional shock-shock interactions in the scramjet inlet are discussed. The various types of interaction patterns as described by Edney [31] are reviewed and how they occur in the scramjet configuration is discussed. The governing equations and method of solution used are described. Depending upon the Mach number and the angle of attack, the forebody shock can interact with the inlet flow; thus producing a very complex flow field. The primary factors affecting the nature of the interaction are freestream conditions, strength of the impinging shock, geometry and impingement location. Shock-shock interaction can also occur on space shuttle, missile launcher and other high-speed aircrafts. As mentioned earlier, this study concentrates on interactions in scramjet inlet but the results obtained are very general in nature and can be applied to other applications as well. All interactions considered here are of the free interaction type i.e., the region upstream of the interaction zone is independent of the source of impinging shock. Two types of interaction can occur in the scramjet inlet; interaction of the forebody and the cowl shock, and the interaction of the forebody and the inlet sidewall shock. The interaction of cowl lip shock with the forebody shock is modeled by a cylindrically blunt wedge with an oblique shock impinging on it in such a way that the line of interaction is parallel

to the cylinder axis. If the end effects are neglected, the flow in each plane normal to the interaction line should be identical. Therefore, a two-dimensional model as is shown in Fig. 4.1 is used. The interaction of inlet sidewall shock and the forebody shock is more complicated because the inlet sidewalls are swept back and the forebody shock is normal to the axis. Thus the flow is fully three-dimensional in nature. The interaction point of the forebody and inlet sidewalls shocks is far away from the inlet/body junction. Therefore, the effect of the body on the shock-shock interaction is neglected and the inlet sidewalls is modeled by an infinite swept blunt wedge with impinging shock normal to its axis as shown in Fig. 4.2.

4.1 Classification

Edney [31] in 1968 categorized the shock-shock interactions into six basic patterns (Types I to VI, Figs. 4.3 - 4.8). The primary factors in determining the type of interaction are strength of the impinging shock, location of the impingement and the freestream Mach number. All six types of interactions can occur when an oblique shock interacts with the bow shock of the leading edge. This classification is a general one and sometimes it is not clear to which category an interaction belongs. Types I, II, and V interactions result in shock-boundary layer interactions, Type III results in attaching shear layer interaction, Type IV produces a supersonic jet, surrounded by subsonic flow and the Type VI interaction results in an expansion fan-boundary layer interaction. The shock-shock interaction causes the stagnation point to move and produce a localized zone of high pressure and heat transfer. Since for a blunt body the peak heating and pressure occur at the stagnation point, an amplification factor is defined as ratio of the peak value of pressure (or heat transfer) divided by its value at the stagnation point for the unimpinged case.

The Type I interaction occurs when two weak shocks of opposite family interact. When an oblique shock intersects the leading edge shock well above the

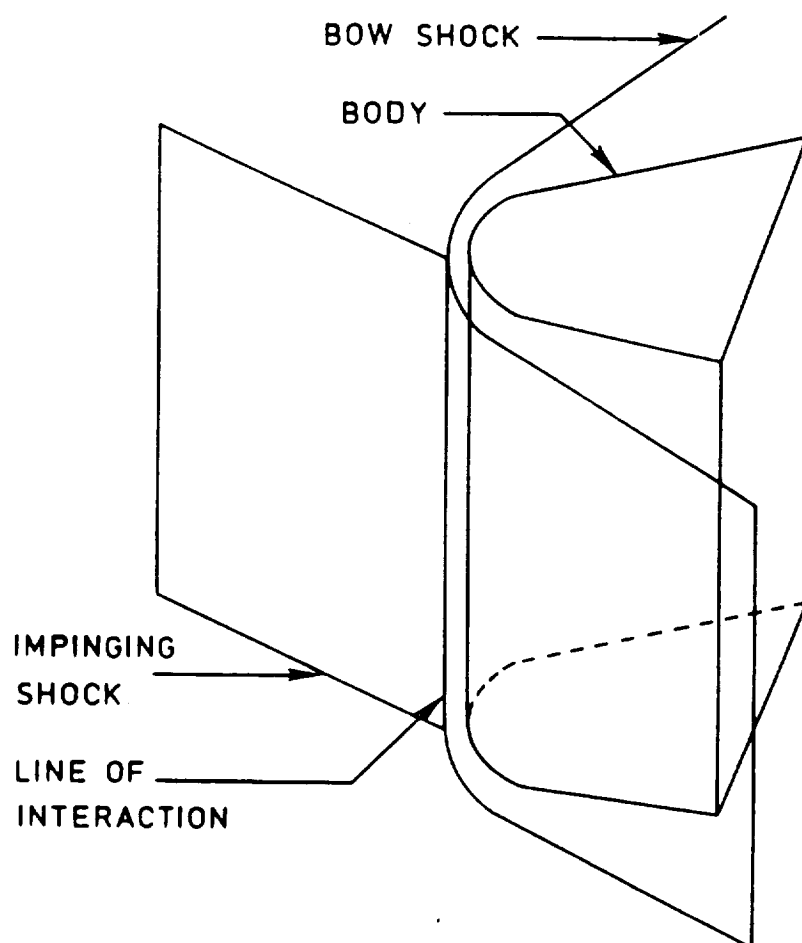


Fig. 4.1 Physical model for forebody and cowl shock interaction.

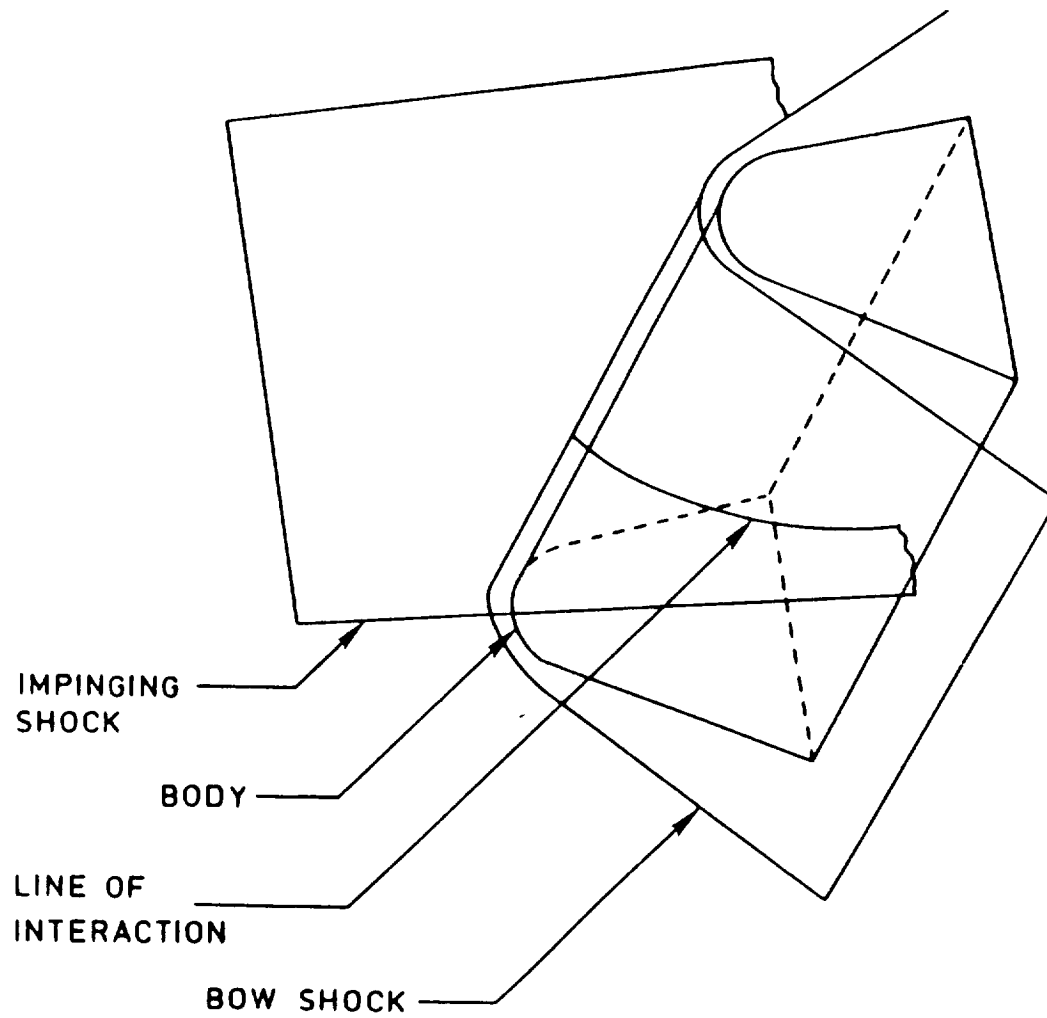


Fig. 4.2 Physical model for forebody and inlet shock interaction.

upper sonic line, the interaction occurs as is shown in Fig. 4.3. The interaction produces a shear layer and a transmitted shock; the shock strikes the body, thus causing shock-boundary layer interaction. If the transmitted shock is strong, it can cause boundary layer to become turbulent or even separated. Holden [61] correlated the peak pressure and heat transfer with the relation $q/q_o = (p/p_o)^{0.85}$ over the Mach number range 2.4 - 13.

A Type II interaction occurs when two shocks of opposite family intersect. If the impinging shock intersects the leading edge shock just above the upper sonic line, this type of interaction is produced. This interaction produces two shear layers and a transmitted shock as shown in Fig. 4.4. The transmitted shock strikes the body, causing pressure and heating amplification. Depending upon the body shape, the shear layer can also strike the body, thus resulting in additional amplification of heating and pressure. In general, the upper shear layer (from pt. A) is stronger than the lower shear layer (from pt. B).

A Type III interaction occurs when a weak shock wave interacts with the strong shock wave. When the oblique shock strikes the bow shock inside the sonic region, this type of interaction occurs. The flow is supersonic above the shear layer and subsonic below it. A reflected shock exists between the body and the leading edge shock which turns the flow parallel to the body. The pressure and heating rates are amplified due to striking shear layer and reflected shock. times.

A Type IV interaction occurs when the impinging shock strikes the leading edge shock near the stagnation zone, where the shock is nearly normal. This produces a supersonic jet bounded by two shear layers and submerged in subsonic flow. Near the body, it produces jet bow shock and stagnation zone when it strikes the body. This produces a very complex flow field with presence of shocks, shear layers and the jet. Type IV interaction is the most severe case and produces the largest amplification of heating and pressure.

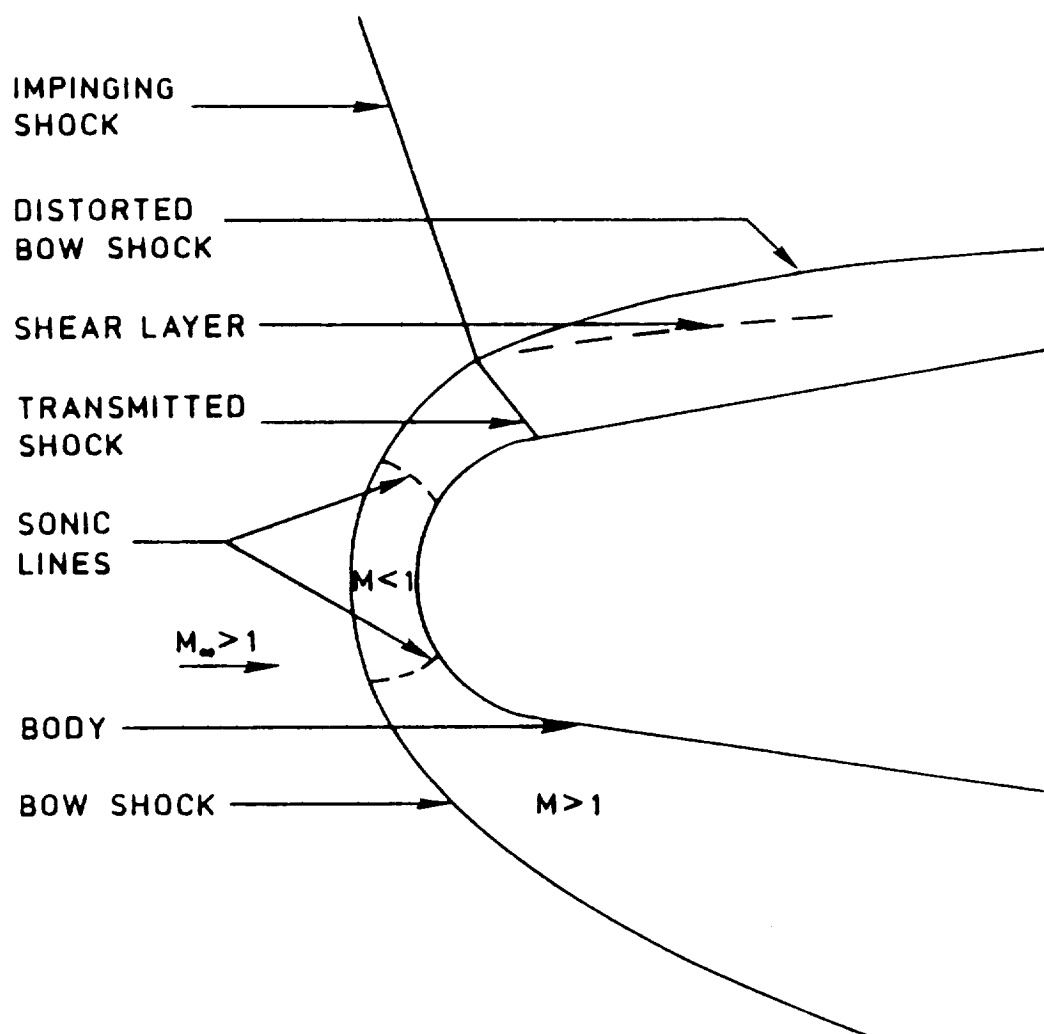


Fig. 4.3 Type I shock-shock interaction.

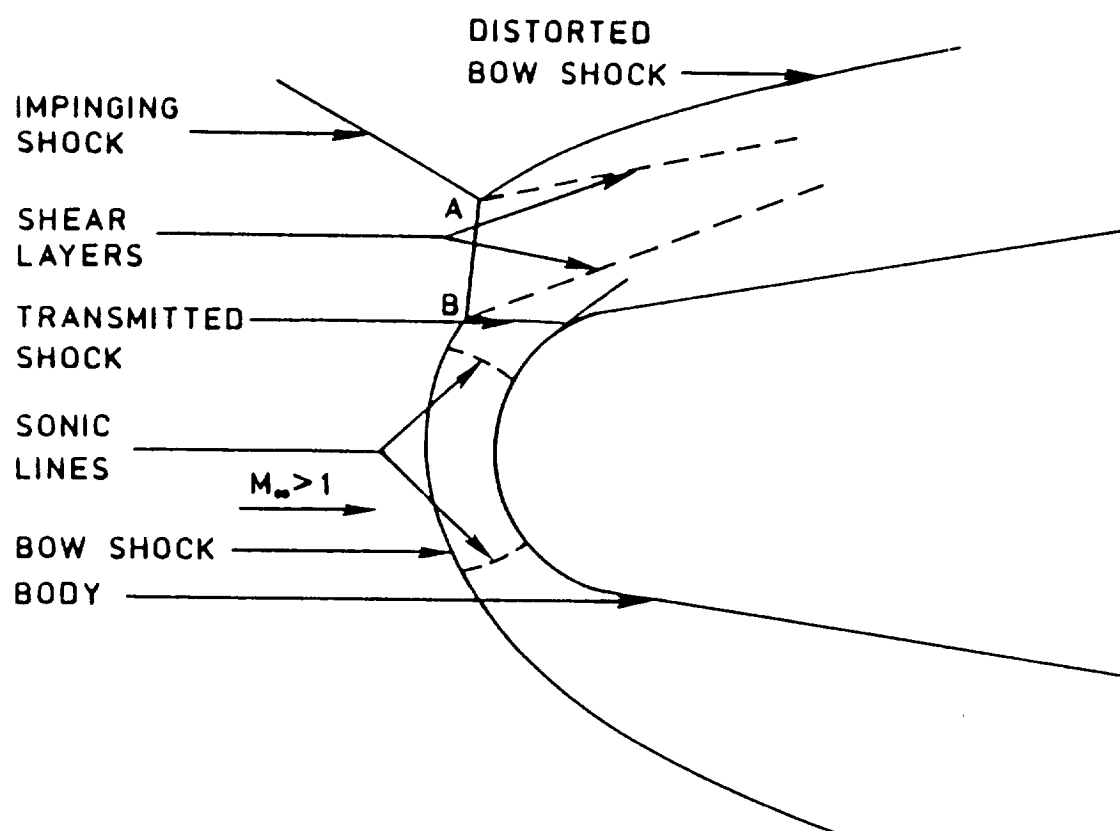


Fig. 4.4 Type II shock-shock interaction.

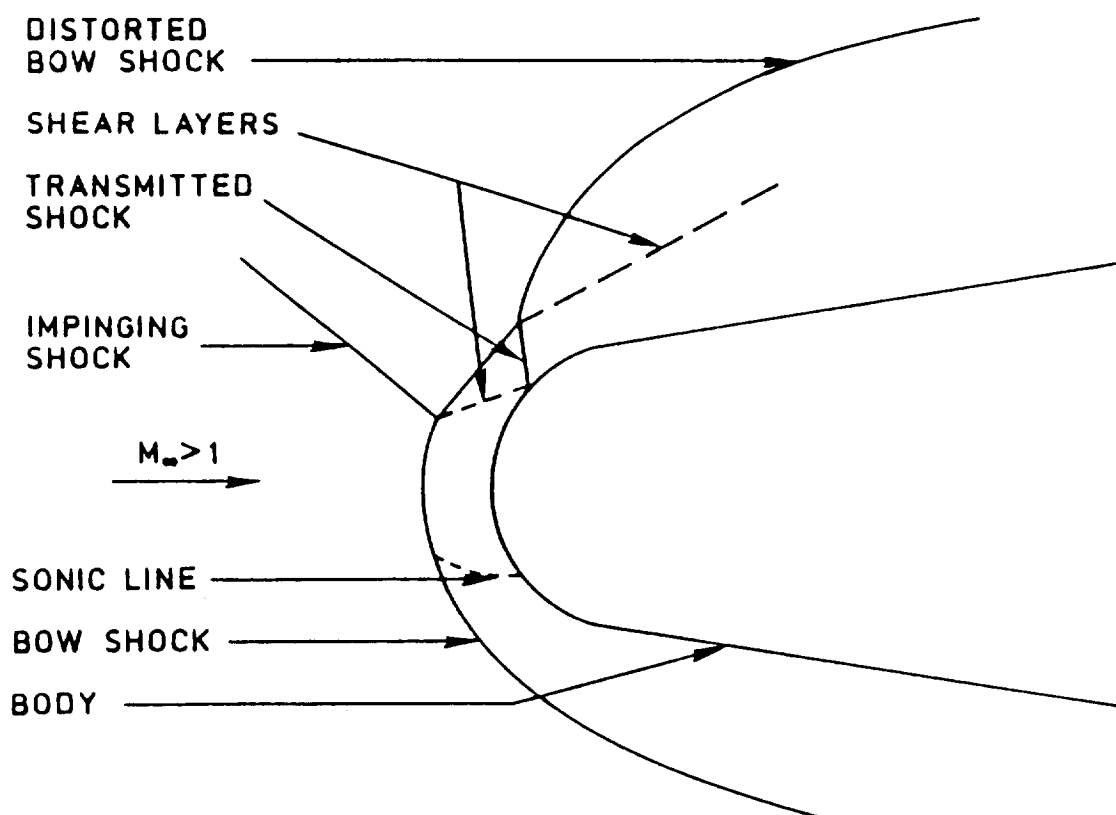


Fig. 4.5 Type III shock-shock interaction.

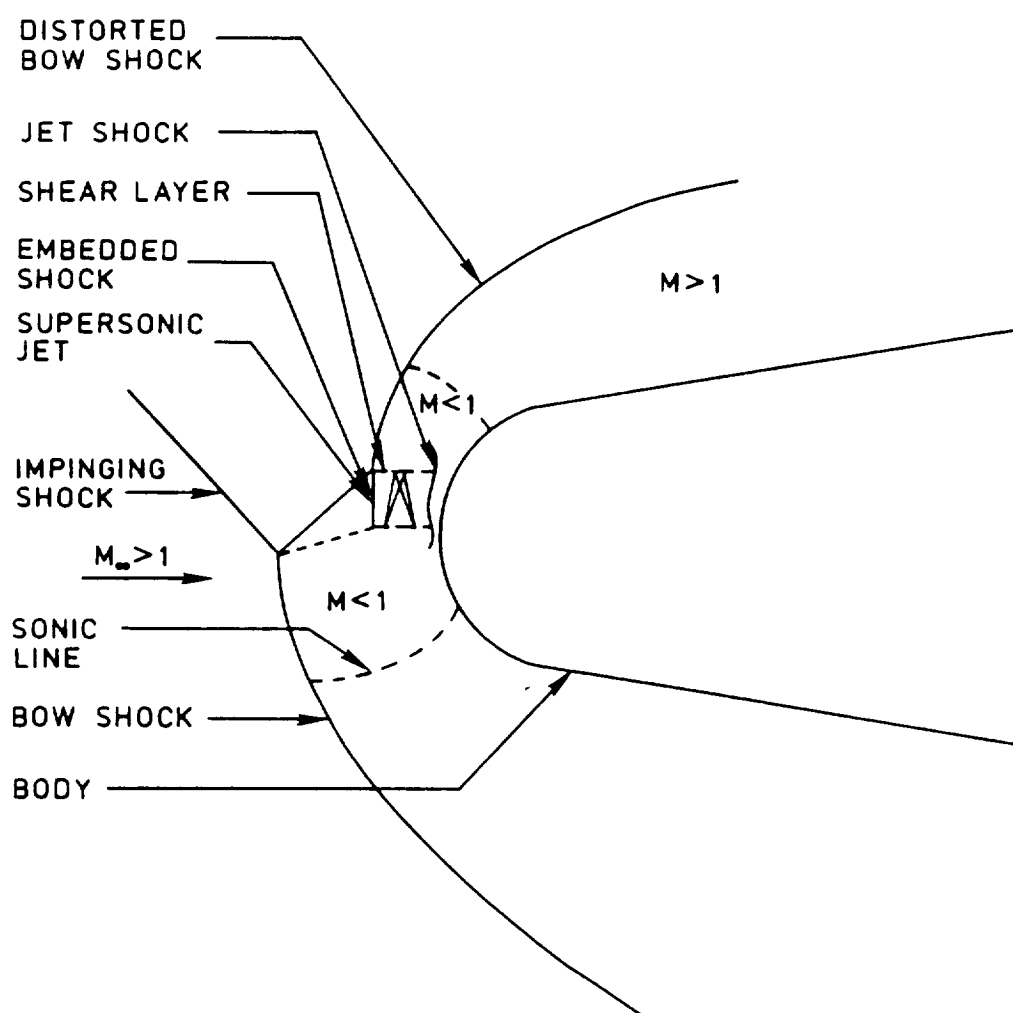


Fig. 4.6 Type IV shock-shock interaction.

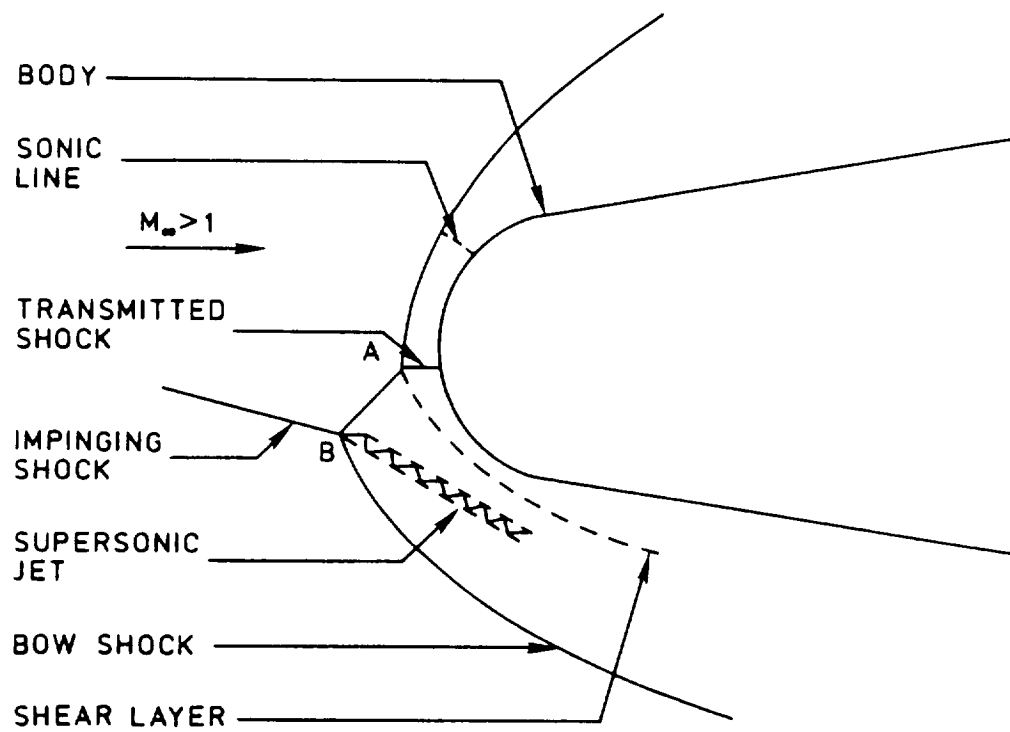


Fig. 4.7 Type V shock-shock interaction.

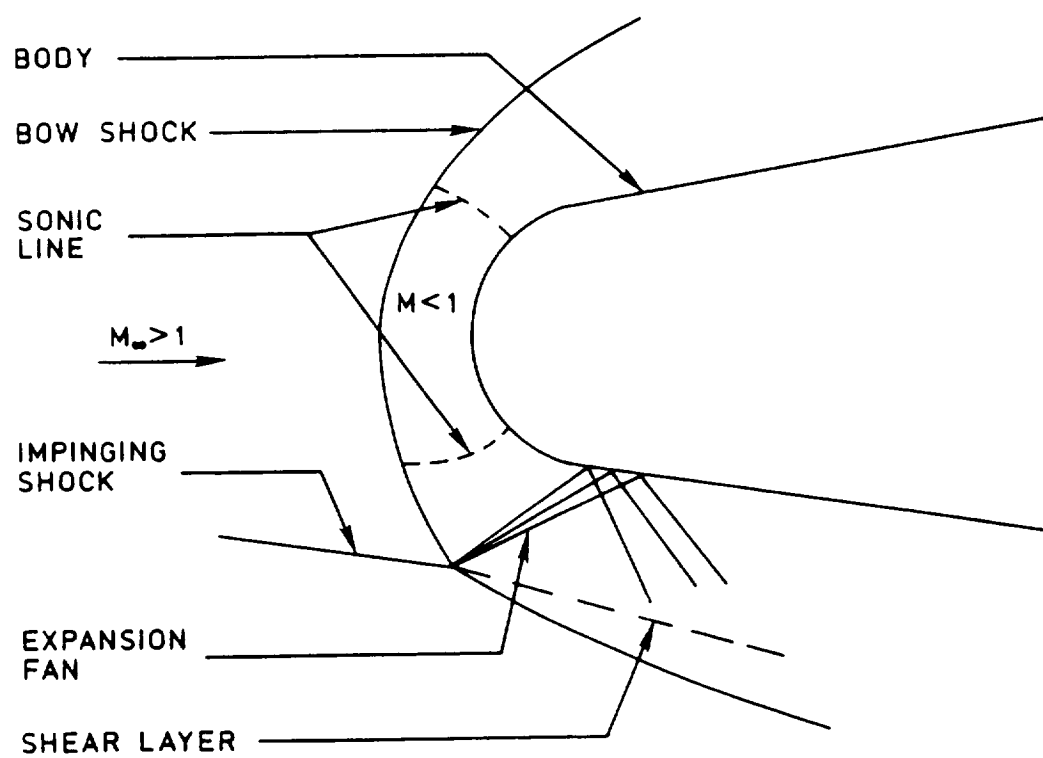


Fig. 4.8 Type VI shock-shock interaction.

When the oblique shock intersects the bow shock just below the lower sonic line (Fig.4.7), Type V interaction is produced. In this case, the shocks are of the the same family. The interaction produces a thin supersonic jet and a shear layer. It is very similar to the Type II interaction.

A Type VI interaction occurs, when the two weak shocks of the same family interact; these shocks are weaker than Type V interaction. Such a situation exists when a weak impinging shock intersects the bow shock well below the lower sonic line. An expansion fan is produced from the intersection point, which causes decrease in pressure and heating rates.

4.2 Governing Equations

The Navier-Stokes equations in cartesian coordinates describing three dimensional, unsteady compressible flow in the absence of external body force can be written in differential form as [51]

$$\frac{\partial Q}{\partial t} + \frac{\partial(E - E_v)}{\partial x} + \frac{\partial(F - F_v)}{\partial y} + \frac{\partial(G - G_v)}{\partial z} = 0 \quad (4.1)$$

where

$$Q = \begin{bmatrix} \rho \\ \rho u \\ \rho v \\ \rho w \\ e \end{bmatrix}$$

$$E = \begin{bmatrix} \rho u \\ \rho u^2 + p \\ \rho uv \\ \rho uw \\ (e + p)u \end{bmatrix}, \quad E_v = \begin{bmatrix} 0 \\ \tau_{xx} \\ \tau_{xy} \\ \tau_{xz} \\ \tau_{xx}u + \tau_{xy}v + \tau_{xz}w - \dot{q}_x \end{bmatrix}$$

$$F = \begin{bmatrix} \rho v \\ \rho vu \\ \rho v^2 + p \\ \rho vw \\ (e + p)v \end{bmatrix}, \quad F_v = \begin{bmatrix} 0 \\ \tau_{xy} \\ \tau_{yy} \\ \tau_{yz} \\ \tau_{xy}u + \tau_{yy}v + \tau_{yz}w - \dot{q}_y \end{bmatrix}$$

$$G = \begin{bmatrix} \rho w \\ \rho w u \\ \rho w v \\ \rho w^2 + p \\ (e + p)w \end{bmatrix}, \quad G_v = \begin{bmatrix} 0 \\ \tau_{xx} \\ \tau_{yx} \\ \tau_{zx} \\ \tau_{xx}u + \tau_{yx}v + \tau_{zx}w - \dot{q}_x \end{bmatrix}$$

$$\tau_{x_i x_j} = \frac{M_\infty}{Re_L} \left[\mu \left(\frac{\partial u_i}{\partial x_j} + \frac{\partial u_j}{\partial x_i} \right) + \lambda \frac{\partial u_k}{\partial x_k} \delta_{ij} \right]$$

$$\dot{q}_{x_i} = - \left[\frac{\mu M_\infty}{Re_L Pr(\gamma - 1)} \right] \frac{\partial T}{\partial x_i}$$

The molecular viscosity is calculated from the Sutherland's law and the Stoke's hypothesis for bulk viscosity, $\lambda + \frac{2\mu}{3} = 0$ is invoked. The perfect gas equation of state is used to define the pressure p via the internal energy as

$$p = (\gamma - 1) \left[e - \rho(u^2 + v^2 + w^2)/2 \right] \quad (4.2)$$

4.2.1 Nondimensionalization

Equation(4.1) is nondimensionalized as follows

$$\begin{aligned} \rho &= \frac{\tilde{\rho}}{\tilde{\rho}_\infty} \\ u &= \frac{\tilde{u}}{\tilde{a}_\infty} \\ v &= \frac{\tilde{v}}{\tilde{a}_\infty} \\ w &= \frac{\tilde{w}}{\tilde{a}_\infty} \\ e &= \frac{\tilde{e}}{a_\infty^2 \tilde{\rho}_\infty} \\ p &= \frac{\tilde{p}}{a_\infty^2 \tilde{\rho}_\infty} \\ T &= \frac{\tilde{T}}{\tilde{T}_\infty} \end{aligned}$$

In the above equations tilde denotes the dimensional quantity and the subscript ∞ denotes the freestream quantity.

4.2.2 Coordinate Transformation

The governing equations are transformed to the body-fitted coordinate system (ξ, η, ζ) using a steady transformation of the type

$$\xi = \xi(x, y, z)$$

$$\eta = \eta(x, y, z)$$

$$\zeta = \zeta(x, y, z)$$

The Jacobian of the transformation is denoted by J and is given by

$$\begin{aligned} J &= \frac{\partial(\xi, \eta, \zeta)}{\partial(x, y, z)} \\ &= \begin{bmatrix} x_\xi y_\eta z_\zeta + x_\zeta y_\xi z_\eta + x_\eta y_\zeta z_\xi - x_\xi y_\zeta z_\eta - x_\eta y_\xi z_\zeta - x_\zeta y_\eta z_\xi \end{bmatrix} \end{aligned} \quad (4.3)$$

Using the chain rule of partial differentiation, the transformation metrics are defined as follows [51]

$$\xi_x/J = y_\eta z_\zeta - z_\eta y_\zeta$$

$$\xi_y/J = z_\eta x_\zeta - x_\eta z_\zeta$$

$$\xi_z/J = x_\eta y_\zeta - y_\eta x_\zeta$$

$$\eta_x/J = z_\xi y_\zeta - y_\xi z_\zeta$$

$$\eta_y/J = x_\xi z_\zeta - z_\xi x_\zeta$$

$$\eta_z/J = y_\xi x_\zeta - x_\xi y_\zeta$$

$$\zeta_x/J = y_\xi z_\eta - z_\xi y_\eta$$

$$\zeta_y/J = z_\xi x_\eta - x_\xi z_\eta$$

$$\zeta_z/J = x_\xi y_\eta - y_\xi x_\eta$$

After applying the generalized coordinate transformation to Eq.(4.1), it can be expressed in the strong conservation-law form as

$$\frac{\partial \hat{Q}}{\partial t} + \frac{\partial(\hat{E} - \hat{E}_v)}{\partial \xi} + \frac{\partial(\hat{F} - \hat{F}_v)}{\partial \eta} + \frac{\partial(\hat{G} - \hat{G}_v)}{\partial \zeta} = 0 \quad (4.4)$$

where the new variables are defined as

$$\begin{aligned}\hat{Q} &= Q/J \\ \hat{E} - \hat{E}_v &= \frac{|\Delta\xi|}{J} \left[\hat{\xi}_x(E - E_v) + \hat{\xi}_y(F - F_v) + \hat{\xi}_z(G - G_v) \right] \\ \hat{F} - \hat{F}_v &= \frac{|\Delta\eta|}{J} \left[\hat{\eta}_x(E - E_v) + \hat{\eta}_y(F - F_v) + \hat{\eta}_z(G - G_v) \right] \\ \hat{G} - \hat{G}_v &= \frac{|\Delta\zeta|}{J} \left[\hat{\zeta}_x(E - E_v) + \hat{\zeta}_y(F - F_v) + \hat{\zeta}_z(G - G_v) \right]\end{aligned}$$

for $k = (\xi, \eta, \zeta)$ respectively.

$$\begin{aligned}(\hat{k}_x, \hat{k}_y, \hat{k}_z) &= \frac{(k_x, k_y, k_z)}{|\Delta k|} \\ |\Delta k| &= \left[k_x^2 + k_y^2 + k_z^2 \right]^{\frac{1}{2}}\end{aligned}$$

The inviscid and viscous flux vectors in generalized coordinate system can now be defined as

$$\begin{aligned}\hat{E} &= \frac{1}{J} \begin{bmatrix} \rho U \\ \rho U u + \xi_x p \\ \rho U v + \xi_y p \\ \rho U w + \xi_z p \\ (e + p)U \end{bmatrix}, \quad E_v = \frac{1}{J} \begin{bmatrix} 0 \\ \xi_x \tau_{xx} + \xi_y \tau_{xy} + \xi_z \tau_{xz} \\ \xi_x \tau_{yx} + \xi_y \tau_{yy} + \xi_z \tau_{yz} \\ \xi_x \tau_{zx} + \xi_y \tau_{zy} + \xi_z \tau_{zz} \\ \xi_x b_x + \xi_y b_y + \xi_z b_z \end{bmatrix} \\ \hat{F} &= \frac{1}{J} \begin{bmatrix} \rho V \\ \rho V u + \eta_x p \\ \rho V v + \eta_y p \\ \rho V w + \eta_z p \\ (e + p)V \end{bmatrix}, \quad F_v = \frac{1}{J} \begin{bmatrix} 0 \\ \eta_x \tau_{xx} + \eta_y \tau_{xy} + \eta_z \tau_{xz} \\ \eta_x \tau_{yx} + \eta_y \tau_{yy} + \eta_z \tau_{yz} \\ \eta_x \tau_{zx} + \eta_y \tau_{zy} + \eta_z \tau_{zz} \\ \eta_x b_x + \eta_y b_y + \eta_z b_z \end{bmatrix} \\ \hat{G} &= \frac{1}{J} \begin{bmatrix} \rho W \\ \rho W u + \zeta_x p \\ \rho W v + \zeta_y p \\ \rho W w + \zeta_z p \\ (e + p)W \end{bmatrix}, \quad G_v = \frac{1}{J} \begin{bmatrix} 0 \\ \zeta_x \tau_{xx} + \zeta_y \tau_{xy} + \zeta_z \tau_{xz} \\ \zeta_x \tau_{yx} + \zeta_y \tau_{yy} + \zeta_z \tau_{yz} \\ \zeta_x \tau_{zx} + \zeta_y \tau_{zy} + \zeta_z \tau_{zz} \\ \zeta_x b_x + \zeta_y b_y + \zeta_z b_z \end{bmatrix}\end{aligned}$$

where U , V , and W are contravariant velocities and are given as,

$$U = \xi_x u + \xi_y v + \xi_z w$$

$$V = \eta_x u + \eta_y v + \eta_z w$$

$$W = \zeta_x u + \zeta_y v + \zeta_z w$$

and

$$b_{z_i} = u_j \tau_{z_i z_j} - \dot{q}_{z_i} \quad (4.5)$$

For two-dimensional calculations, E and E_v were set equal to zero, thus reducing the governing equations to two-dimensions with ζ normal to the surface and η along it. For three-dimensional case, viscous terms were dropped in ξ and η directions due to coarse grids in axial and circumferential directions.

4.2.3 Finite Volume Formulation

Equation (4.4) is solved using a finite volume method. In this method, the integral formulation of the conservation laws is discretized directly in the physical space. The direct discretization ensures that mass, momentum and energy are conserved at discrete levels. It remains valid in the presence of discontinuities in the flow field such as shocks and contact surfaces. Eq.(4.4) is expressed in the integral form as

$$\frac{\partial}{\partial t} \int \int \int_V Q dV + \int \int_S \vec{F} \cdot \hat{n} dS = 0 \quad (4.6)$$

where $\vec{F} = (E - E_v)\hat{i} + (F - F_v)\hat{j} + (G - G_v)\hat{k}$, and $\hat{n} = n_x\hat{i} + n_y\hat{j} + n_z\hat{k}$ is the unit normal vector pointing outward from the surface S bounding the volume V . A semi-discrete finite volume representation of Eq.(4.4) leads to

$$\begin{aligned} & \left(\frac{\partial \hat{Q}}{\partial t} \right)_{i,j,k} + (\hat{E} - \hat{E}_v)_{i+\frac{1}{2},j,k} - (\hat{E} - \hat{E}_v)_{i-\frac{1}{2},j,k} \\ & + (\hat{F} - \hat{F}_v)_{i,j+\frac{1}{2},k} - (\hat{F} - \hat{F}_v)_{i,j-\frac{1}{2},k} \\ & + (\hat{G} - \hat{G}_v)_{i,j,k+\frac{1}{2}} - (\hat{G} - \hat{G}_v)_{i,j,k-\frac{1}{2}} = 0 \end{aligned} \quad (4.7)$$

It can be shown that Eq.(4.6) can be written in a form identical to Eq.(4.7) by writing the surface integrals as the sum of the contribution from six faces of the hexagonal cell. In the computational domain (ξ, η, ζ) ,

$$\Delta\xi = \xi_{i+\frac{1}{2}} - \xi_{i-\frac{1}{2}} = 1$$

Similarly,

$$\Delta\eta = \Delta\zeta = 1$$

The fluxes are evaluated at the cell boundaries defined by the grid points as is shown in Fig. 4.9. So far the method of solution has been identical to the finite difference method. In most of the finite difference methods the transformation matrices and Jacobian is calculated by using the two point central difference formulas. This leads to inconsistency in the volume and surface normal calculations such that the geometric conservation laws are not satisfied and hence the scheme fails to capture the freestream when evaluated on arbitrary meshes. In the present method, geometrical interpretation of the Jacobian and transformation terms is made. The Jacobian is calculated as inverse of the cell volume, the vector $\Delta\mathbf{k}/J$ is the directed area of the cell surface to a $k = \text{constant}$ coordinate direction and $|\Delta\mathbf{k}|/J$ is the area of the cell interface. Here k represents ξ , η , and ζ , respectively.

The volume of a cell is defined by its eight vertex points and is calculated as the sum of six pentahedrons. Each pentahedron is formed by one of the six cell faces and the average point in the cell volume. The directed area of the cell interface is calculated as one half of the vector cross product of two diagonal vectors joining the four vertex points. In general, all four vertex points do not lie in the same plane. So the directed area so formed corresponds to the planar surface obtained by passing a least square plane through the four points and then projecting them into the plane. This approach satisfies the geometrical conservation laws and makes the numerical scheme compatible with the finite volume formulation.

4.3 Method of Solution

Over the past few years, upwind space discretization methods have become a popular alternative to the central space discretization methods. The basic

- Q evaluated at cell centers, ijk

- x Fluxes evaluated on the cell faces, e.g. $\hat{F}_{i+1/2, j, k}$

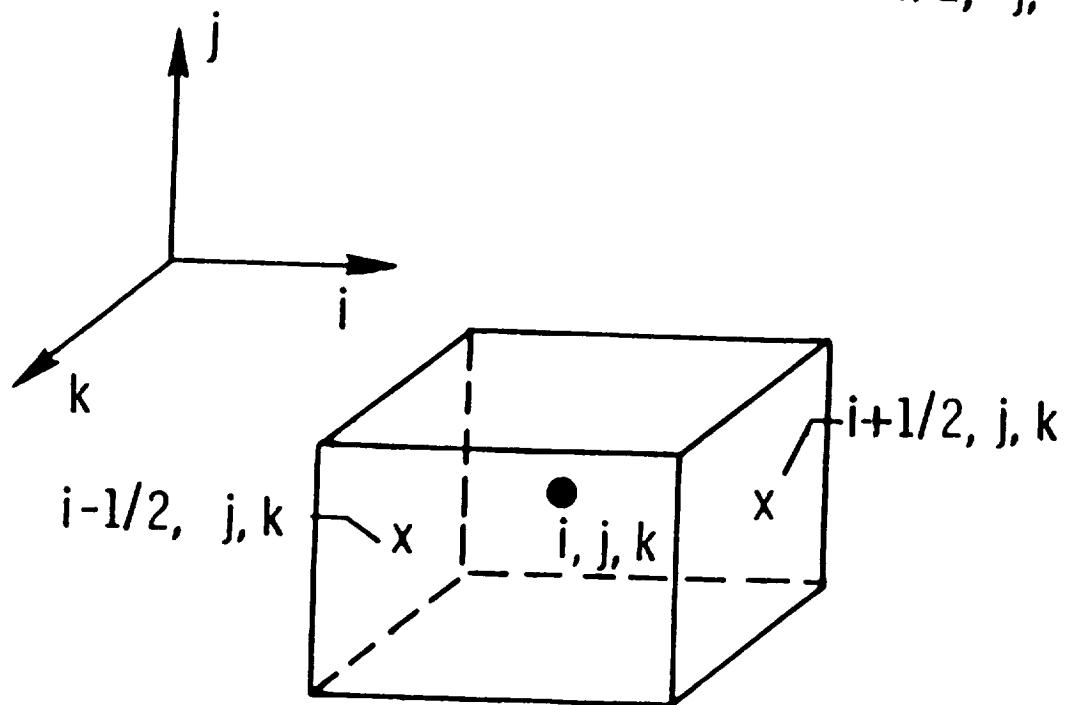


Fig. 4.9 Finite volume formulation.

idea behind the development of upwind scheme is that they try to mimic the directional dependence by applying asymmetric space discretization with a bias toward the direction from which the information is propagating. The upwind differencing reflects the predominant nature of the Navier-Stokes equations in the limit as $Re \rightarrow \infty$ (hyperbolic) and $Re \rightarrow 0$ (parabolic). This improvement in physical treatment comes with increased computational work per iteration but the total number of iterations is reduced thus offsetting the increased computation time per iteration. These methods are naturally dissipative and therefore no artificial viscosities with problem dependent coefficients are needed.

The Navier-Stokes equations consist of inviscid (pressure and convective) terms and viscous (diffusive) terms. In the upwind methods, the inviscid fluxes are split into positive and negative components based on eigen values, and then spatially differenced by backward or forward differencing. The differencing could be first order, second order fully upwind or third order upwind biased. First order upwind differencing have a large amount of numerical dissipation which makes it unsuitable for meaningful calculations. The second order upwind schemes have second order truncation error; the leading term of this truncation error is dispersive and the leading numerical dissipative term is actually a third order, fourth derivative term. Even for third order differencing the scheme is actually second order because of the second order treatment of diffusion terms. Hence, the numerical dissipation of the second order upwind scheme is of the same order as the central difference scheme. The central difference schemes have been shown to be superior than upwind schemes in the viscous zone [62].

Various upwind algorithms are available in the literature. These are λ scheme [63], split coefficient method (SCM) [64], flux difference methods [65] - [68] and flux vector differencing [69] and [70]. For the physical problem of shock-shock interaction, various schemes were tried. The first scheme tried was explicit

MacCormack [71] with central differencing. The solution had excessive oscillation at high Mach numbers and required proper tuning of damping coefficient, also due to explicit nature of the scheme, the time step was very restrictive for the grid employed. The flux differencing algorithm developed by Roe [68] gave physically incorrect solution even for unimpinged blunt body flows. The bow shock had a dimple near the stagnation point. For some cases, the shock did not even stabilize but continued to move upstream until stopped by the inflow boundary. The peak pressure value was not at the stagnation point but rather away from it. The same type of phenomenon has been observed for the Roe's scheme by Perry et al. [45]. The critical Mach number around which this phenomenon starts is about 6.0 [72]. This phenomenon is not fully understood yet, and therefore no rigorous correction to Roe's scheme to eliminate this problem is available. However, some progress has been made for simple flows by adding eigen value smoothing [45]. van Leer's [70] flux vector splitting method gave the best results for this problem. Consequently, this method has been used for two-and three-dimensional shock-shock interactions.

4.3.1 Flux Vector Splitting

Steger and Warming in 1981 [69], realizing the homogeneity property of the Euler equation, proposed a novel way of splitting the inviscid fluxes into positive and negative subvectors based on the eigen values. The positive subvector is associated with the non-negative eigen values and negative subvector is associated with the non-positive eigen values. The split fluxes are then spatially discretized using one sided upwind differencing. The splitting is not unique and various combinations are possible as long as the sum of two subvectors is the same as the original vector. The details of this splitting and its implementation into Euler equation is available in [69]. The main drawback of this type of splitting is that forward and backward fluxes although continuous, are not differentiable when an eigen value changes sign.

Such phenomena occurs at stagnation and sonic points. This causes small glitches in the solution near these points. van Leer in 1982 [70] proposed a similar splitting but with continually differentiable fluxes by introducing additional requirements that the Jacobian must be a continuous function of the Mach number. As mentioned earlier, upwind differencing is applied to inviscid fluxes only, the viscous fluxes are centrally differenced.

Splitting the fluxes in ξ direction,

$$\hat{E} = \hat{E}^+ + \hat{E}^- \quad (4.8)$$

where

$$\begin{aligned} \hat{E}^+ &= \hat{E} \quad , \quad \hat{E}^- = 0 \quad \text{for } M_\xi \geq +1 \\ \hat{E}^- &= \hat{E} \quad , \quad \hat{E}^+ = 0 \quad \text{for } M_\xi \leq -1 \end{aligned}$$

Here M_ξ is the contravariant Mach number along ξ and is given as

$$M_\xi = \bar{u}/c \quad , \quad \bar{u} = U/|\Delta\xi|$$

For subsonic flows. $|M_\xi| < 1$, the split fluxes are obtained as follows

$$\hat{E}^\pm = \frac{\Delta\xi}{J} \begin{bmatrix} f_1^\pm \\ f_1^\pm \{\hat{k}_x(-\bar{u} \pm 2c)/\gamma + u\} \\ f_1^\pm \{\hat{k}_y(-\bar{u} \pm 2c)/\gamma + v\} \\ f_1^\pm \{\hat{k}_z(-\bar{u} \pm 2c)/\gamma + w\} \\ f_5^\pm \end{bmatrix} \quad (4.9)$$

where

$$f_1^\pm = \pm \rho c (M_\xi \pm 1)^2 / 4$$

$$f_5^\pm = f_1^\pm \left[\{-(\gamma - 1)\bar{u}^2 \pm 2(\gamma - 1)\bar{u}c + 2c^2\}/(\gamma^2 - 1) + (u^2 + v^2 + w^2)/2 \right]$$

The conserved state variables on the cell interface are obtained as

$$\begin{aligned} Q_{i+\frac{1}{2}}^- &= Q_i + \frac{1}{4}\phi_\xi \left[(1 - \kappa_\xi) \nabla_\xi + (1 + \kappa_\xi) \Delta_\xi \right] Q_i \\ Q_{i+\frac{1}{2}}^+ &= Q_{i+1} - \frac{1}{4}\phi_\xi \left[(1 + \kappa_\xi) \nabla_\xi + (1 - \kappa_\xi) \Delta_\xi \right] Q_{i+1} \end{aligned} \quad (4.10)$$

where

$$\Delta_{\xi} Q_i = Q_{i+1} - Q_i$$

$$\nabla_{\xi} Q_i = Q_i - Q_{i-1}$$

The switch ϕ is zero for the first order differencing and unity for higher order differencing. The parameter κ determines the order of differencing; $\kappa_{\xi} = -1$ corresponds to the fully upwind second order, $\kappa_{\xi} = 0$ corresponds to second order upwind biased, $\kappa_{\xi} = +1$ to second order central differencing, and $\kappa_{\xi} = +1/3$ to the third order upwind biased. Having obtained the value of Q at cell interfaces, the split flux differences are implemented as follows

$$\delta_{\xi} \hat{E}_i = \delta_{\xi} \hat{E}_i^- + \delta_{\xi} \hat{E}_i^+ \quad (4.11)$$

$$= \hat{E}^+(Q^-)_{i+\frac{1}{2}} - \hat{E}^+(Q^-)_{i-\frac{1}{2}} + \hat{E}^-(Q^+)_{i+\frac{1}{2}} - \hat{E}^-(Q^+)_{i-\frac{1}{2}}$$

The term $\hat{E}^+(Q^-)_{i+\frac{1}{2}}$ denotes the forward flux evaluated at the cell interface $i + \frac{1}{2}$. It should be noted that MUSCLE (monotonic upstream-centered scheme for conservation laws) approach is used. The conservation variable Q is obtained first at the cell interface and then the split fluxes E^{\pm} are obtained. This is in contrast to obtaining E^{\pm} first at the cell center and then interpolating it to get the cell interface value. The former approach has been shown superior than the latter as the split fluxes are less differentiable than conserved variables when transitioning through sonic and stagnation points. Similarly, the fluxes can be split in η and ζ directions also.

4.3.2 Algorithm

For the present calculations, the algorithm developed by Thomas et al. [73] - [75] has been used. The algorithm is outlined for three-dimensional flows and can be specialized for two-dimensional flow as necessary. As noted previously,

viscous terms have been dropped in ξ and η direction; thus Eq.(4.4) can be written as

$$\frac{\partial \hat{Q}}{\partial t} + \frac{\partial \hat{E}}{\partial \xi} + \frac{\partial \hat{F}}{\partial \eta} + \frac{\partial (\hat{G} - \hat{G}_v)}{\partial \zeta} = 0 \quad (4.12)$$

Applying the Euler implicit time integration scheme and linearizing it, one obtains

$$\left(\frac{I}{J\Delta t} - \frac{\partial R^n}{\partial Q} \right) \Delta Q^n = R(Q^n) \quad (4.13)$$

where

$$R(Q^n) = -[\delta_\xi \hat{E} + \delta_\eta \hat{F} + \delta_\zeta (\hat{G} - \hat{G}_v)]^n$$

and

$$\frac{\partial R}{\partial Q} \Delta Q = -[\delta_\xi \left(\frac{\partial \hat{E}^n}{\partial Q} \Delta Q^n \right) + \delta_\eta \left(\frac{\partial \hat{F}^n}{\partial Q} \Delta Q^n \right) + \delta_\zeta \left(\frac{\partial \hat{G}^n}{\partial Q} \Delta Q^n \right) - \delta_\zeta \left(\frac{\partial \hat{G}_v^n}{\partial Q} \Delta Q^n \right)]$$

Equation(4.12) represents a large banded block 5 x 5 matrix equation, the band width depends upon the grid size and choice of spatial discretization. Using second order accurate spatial discretization, it can be expanded as

$$\begin{aligned} & \left(\frac{I}{J\Delta t} + C_\xi + C_\eta + C_\zeta \right) \Delta Q^n + \\ & + A_\xi \Delta Q_{i-2}^n + B_\xi \Delta Q_{i-1}^n + D_\xi \Delta Q_{i+1}^n + H_\xi \Delta Q_{i+2}^n \\ & + A_\eta \Delta Q_{j-2}^n + B_\eta \Delta Q_{j-1}^n + D_\eta \Delta Q_{j+1}^n + H_\eta \Delta Q_{j+2}^n \\ & + A_\zeta \Delta Q_{k-2}^n + B_\zeta \Delta Q_{k-1}^n + D_\zeta \Delta Q_{k+1}^n + H_\zeta \Delta Q_{k+2}^n = R(Q^n) \end{aligned} \quad (4.14)$$

where A,B,C,D and H are 5x5 block matrices associated with implicit spatial differencing in the ξ , η , and ζ directions. The solution of Eq.(4.14) involves inversion of a block pentadiagonal matrix equation. The computational effort is reduced if the implicit-spatial discretization is taken as first order accurate. This does not affect the steady state accuracy which is determined by the spatial differencing of $R(Q)$.

Then, $A_\xi, A_\eta, A_\zeta, H_\xi, H_\eta$, and H_ζ are equal to zero and

$$B_\xi = -\left(\frac{\partial \hat{E}^+}{\partial Q} \right)_{i-1/2}$$

$$\begin{aligned}
C_\xi &= \left(\frac{\partial \hat{E}^+}{\partial Q} \right)_{i+1/2} - \left(\frac{\partial \hat{E}^-}{\partial Q} \right)_{i-1/2} \\
D_\xi &= - \left(\frac{\partial \hat{E}^-}{\partial Q} \right)_{i+1/2}
\end{aligned} \tag{4.15}$$

Similar expressions can be developed in η and ζ directions also.

Using Eq.(4.16), Eq(4.14) can be written as

$$\begin{aligned}
& \left(\frac{I}{J\Delta t} + C_\xi + C_\eta + C_\zeta \right) \Delta Q^n + B_\xi \Delta Q_{i-1}^n + D_\xi \Delta Q_{i+1}^n \\
& + B_\eta \Delta Q_{j-1}^n + D_\eta \Delta Q_{j+1}^n + B_\zeta \Delta Q_{k-1}^n + D_\zeta \Delta Q_{k+1}^n = R(Q^n)
\end{aligned} \tag{4.16}$$

Relaxation is implemented in the streamwise direction and the approximate factorization is implemented in the cross flow planes.

For first order implicit space discretization, the algorithm is stable regardless of the sweep direction. With higher order spatial differencing, alternate forward and backward sweeps are required. For a forward relaxation sweep, ΔQ_{i-1}^n is known and $\Delta Q_{i+1}^n = 0$, then Eq.(4.16) becomes

$$\begin{aligned}
& \left(\frac{I}{J\Delta t} + C_\xi + C_\eta + C_\zeta \right) \Delta Q^n + B_\eta \Delta Q_{j-1}^n + D_\eta \Delta Q_{j+1}^n \\
& + B_\zeta \Delta Q_{k-1}^n + D_\zeta \Delta Q_{k+1}^n = R(Q_{i-2}^{n+1}, Q_{i-1}^{n+1}, Q_i^n, Q_{i+1}^n, Q_{i+2}^n)
\end{aligned} \tag{4.17}$$

Equation(4.17) is written in a compact form as

$$\left[M + \delta_\eta \frac{\partial \hat{F}}{\partial Q} + \delta_\zeta \left(\frac{\partial \hat{G}}{\partial Q} - \frac{\partial \hat{G}_v}{\partial Q} \right) \right] \Delta Q^n = R(Q_{i-2}^{n+1}, Q_{i-1}^{n+1}, Q_i^n, Q_{i+1}^n, Q_{i+2}^n) \tag{4.18}$$

where

$$M = \frac{I}{J\Delta t} + C_\xi$$

Equation (4.18) is approximately factored in η and ζ directions as

$$\begin{aligned}
& \left[M + \delta_\eta \frac{\partial \hat{F}}{\partial Q} \right] M^{-1} \left[M + \delta_\zeta \left(\frac{\partial \hat{G}}{\partial Q} - \frac{\partial \hat{G}_v}{\partial Q} \right) \right] \Delta Q^n \\
& = R(Q_{i-2}^{n+1}, Q_{i-1}^{n+1}, Q_i^n, Q_{i+1}^n, Q_{i+2}^n)
\end{aligned} \tag{4.19}$$

The solution of Eq.(4.19) then involves the solution of two block tridiagonal equations

$$\begin{aligned} [M + \delta_\eta \frac{\partial \hat{F}}{\partial Q}] \phi &= R(Q_{i-2}^{n+1}, Q_{i-1}^{n+1}, Q_i^n, Q_{i+1}^n, Q_{i+2}^n) \\ [M + \delta_\zeta (\frac{\partial \hat{G}}{\partial Q} - \frac{\partial \hat{G}_v}{\partial Q})] \Delta Q^n &= \phi \\ Q^{n+1} &= Q^n + \Delta Q^n \end{aligned} \quad (4.20)$$

For the cowl afterbody calculations the algorithm has been modified so that the downstream influence of the subsonic part of the boundary layer in an otherwise supersonic flow is suppressed by restricting the streamwise pressure gradient. A parabolized solution is then obtained by marching downstream and iterating locally in each plane until convergence. The Vigneron [53] technique as described previously in Chap. 3 is used to modify the algorithm. The details of modified algorithm are available in [74]. The forward flux vector \hat{E} is now modified as

$$\hat{E} = \frac{1}{J} \begin{bmatrix} \rho U \\ \rho U u + \omega \xi_x p \\ \rho U v + \omega \xi_y p \\ \rho U w + \omega \xi_z p \\ (e + p)U \end{bmatrix} \quad (4.21)$$

where ω is the Vigneron factor and was defined in Eq. (3.16). The additional terms due to the explicit lagging of the streamwise terms are neglected, then the procedure is not subjected to the departure solution for arbitrary streamwise mesh spacing. The modified flux and flux Jacobian are split as

$$\begin{aligned} \hat{E}^+(Q^-)_{i\pm 1/2} &= \hat{E}(Q)_{i\pm 1/2} \\ \frac{\partial \hat{E}^+(Q^-)}{\partial Q}_{i\pm 1/2} &= \frac{\partial \hat{E}(Q)}{\partial Q}_{i\pm 1/2} \end{aligned} \quad (4.22)$$

and

$$\begin{aligned} \hat{E}^-(Q^+)_{i\pm 1/2} &= 0 \\ \frac{\partial \hat{E}^-(Q^+)}{\partial Q}_{i\pm 1/2} &= 0 \end{aligned} \quad (4.23)$$

The solution from the (i-1) station is used as initial guess at ith station and is iterated locally to obtain the converged solution and the process is repeated at the next (i+1) station. The resulting algorithm is fully second order accurate. The value of κ is taken as -1 in order to have fully upwind algorithm.

In order to eliminate the overshoots and undershoots near the shocks, Van Albada type continuous differentiable flux limiter has been used in the present calculations. It reduces the scheme to fully one sided. The limiters modify the upwind biased interpolation and are implemented by modifying Eq.(4.10) as follows

$$\begin{aligned} Q_{i+\frac{1}{2}}^- &= Q_i + \frac{s}{4} \left[(1 - s\kappa_\xi) \nabla_\xi + (1 + s\kappa_\xi) \Delta_\xi \right] Q_i \\ Q_{i+\frac{1}{2}}^+ &= Q_{i+1} - \frac{s}{4} \left[(1 + s\kappa_\xi) \nabla_\xi + (1 - s\kappa_\xi) \Delta_\xi \right] Q_{i+1} \end{aligned} \quad (4.24)$$

where

$$s = \frac{2 \Delta_\xi \nabla_\xi + \epsilon}{\Delta_\xi^2 + \nabla_\xi^2 + \epsilon}$$

and $\epsilon = 10^{-6}$ is a small number to prevent the division by zero in the region of zero gradients.

4.4 Grid Generation

The first step in any numerical solution is the discretization of the governing equations from a continuous domain to a set of discrete points (called grid points). The choice of grid points is not an arbitrary one but is governed by physics of the problem. Grid generation is a procedure for orderly distribution of the sampling stations over a physical field in such a way that all physical phenomena in the entire region of interest may be represented with sufficient accuracy by this finite number of sampling stations. Since the computer memory and speed limit the number of grid points, it is very crucial to make best use of the available resources. The grid points should conform to the boundaries and be concentrated in the regions of high gradients such as shocks and boundary layers in order to properly resolve

the flow field. They must also be oriented in such a way that grid is as close to orthogonal as possible.

The grids can be generated by either numerically solving the partial differential equations or algebraic equations. In the present study, an algebraic method is used. In this method, the grid is generated by algebraic interpolation from the boundaries. Here an explicit functional relationship between the computational and physical domain is known. It is much faster than the differential equation approach and offers an easy control of grid spacing and distribution. For the present calculations, various types of grids were employed. For the first set of calculations, an outer boundary consisting of a circular arc was defined. Since the shock capturing algorithm has been employed, the outer boundary was chosen in such a way that there were sufficient number of points between the shock and outer boundary. The grid points were clustered normal to the body using the exponential stretching

$$f(\eta) = \frac{e^{k\eta} - 1}{e^\eta - 1}$$

to resolve the boundary layer. Since the heat transfer and skin friction are strong functions of grid spacing, it is very important to properly resolve the gradients. For the impingement case the shock moves closer to the body on one side and away from the body on the other. Thus a lot of grid points are wasted. In order to alleviate this problem, a semi adaptive grid was used. Figure 4.10 shows this grid, in this case the outer boundary is made to conform with the shape of distorted bow shock, which was obtained by coarse mesh calculations where no attempt was made to resolve the gradients. This type of grid, reduced the wastage of grid points but it requires a new grid every time either freestream conditions are changed or the type of interaction changes. The solution obtained by using this type of grid was much better resolved near the shock region but in the case of impingement where we have a supersonic jet enclosed within subsonic flow and extremely high gradients, the resolution was still less than desired, as will be shown in Chap. 5.

In order to improve upon the solution, adaptive grid system has been used, which adapts the grids during the course of the solution in order to follow the developing gradients in the physical solution. The grid points move as the solution develops, concentrating the points where they are needed the most. The total number of points were kept constant. The final adapted grid for Mach 8.03 case is shown in Fig. 4.11. For this, the method developed by Abolhassani et al. [76] has been used and is explained in Appendix B. It is a very general method with capability to adapt the grids with various variables such as pressure, Mach number, shear stress etc. and is based upon the variational approach. Since the solution varies predominantly in the normal direction, the grids were adapted in only one direction.

The grid for three-dimensional calculations is shown in Figure 4.12. The grid points were clustered near the body in normal direction as well as near the shock impingement location to resolve the gradients. As in the previous case, the outer boundary was moved far enough so as to avoid any interference between the shock and the outflow boundary.

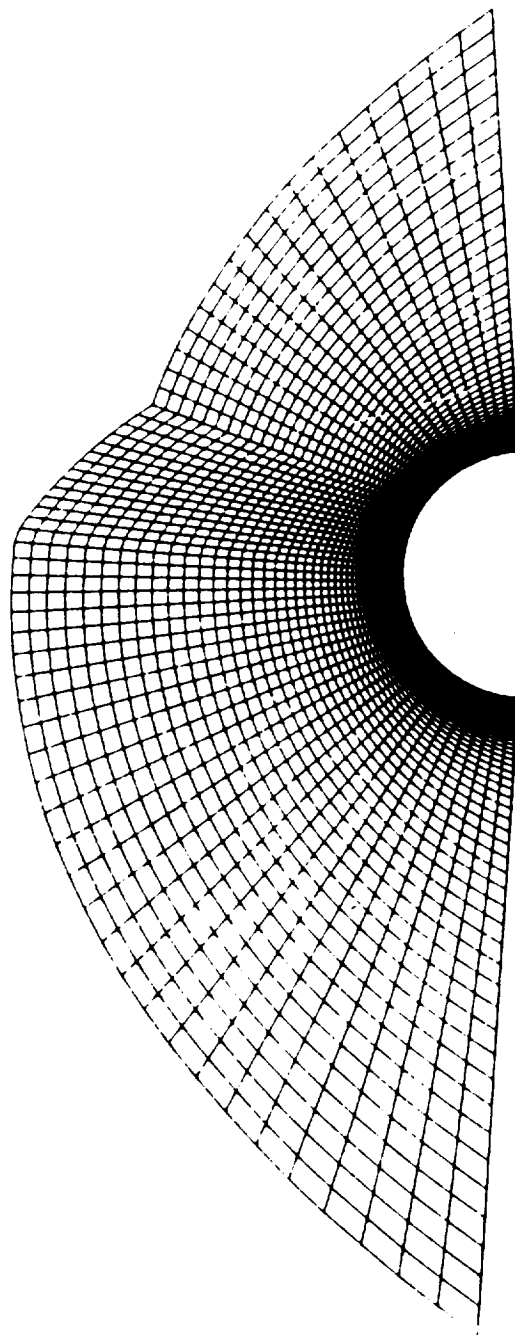


Fig. 4.10 Unadapted grid for two-dimensional calculations.

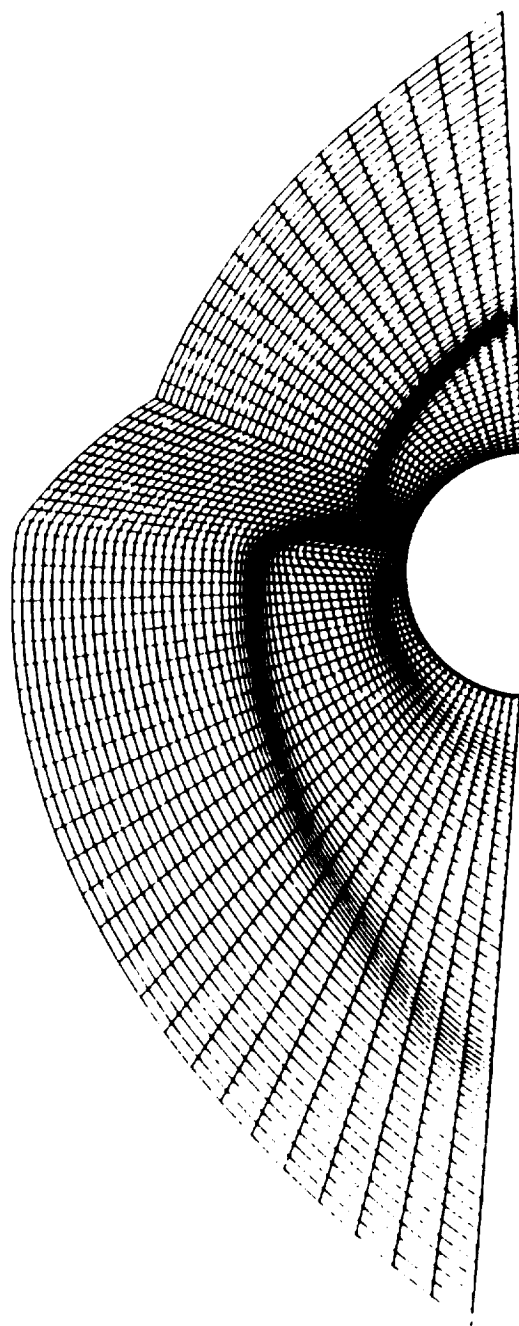


Fig. 4.11 Adapted grid for two-dimensional calculations.

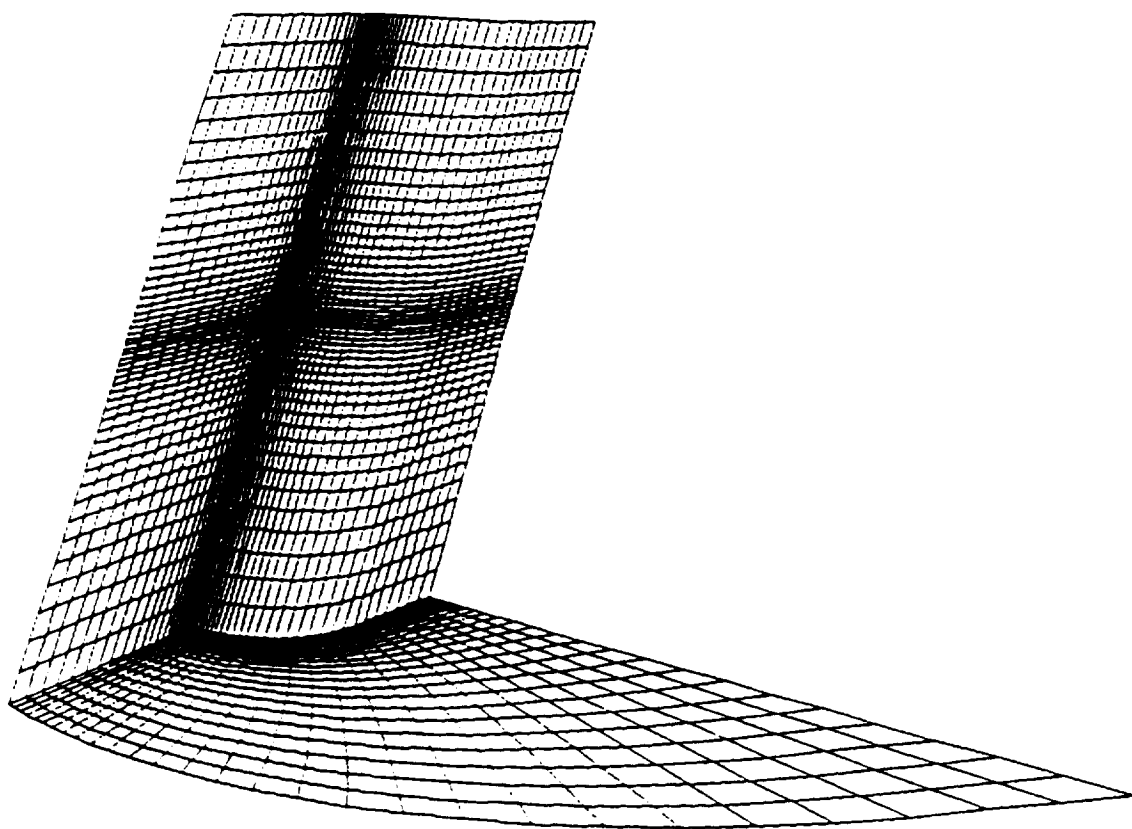


Fig. 4.12 Grid for three-dimensional calculations.

Chapter 5

RESULTS AND DISCUSSION

The numerical schemes described in Chaps. 3 and 4 are applied to obtain steady state results for the forebody and the shock-shock interaction on the cowl plate and inlet sidewalls. All calculations were performed under the assumption of a laminar flow. For the forebody, the flow is calculated by the parabolized Navier-Stokes equations with the starting solution for the nose section provided by the full Navier-Stokes equations. For two-dimensional shock-shock interaction, the full Navier-Stokes equations are used and for three-dimensional interaction, the thin-layer Navier-Stokes equations are used. Results for the nose bluntness effects on the forebody are discussed first followed by the results for the shock-shock interaction on the cowl plate and inlet sidewalls.

5.1 Parametric Study of Nose Bluntness Effects

The parametric studies were conducted to determine the extent of downstream effects of nose bluntness for various freestream conditions given in Table 5.1 for three different values of nose bluntness. The blunted cone with the smallest nose radius is considered as a sharp cone and the effects of leading edge bluntness are compared with respect to this cone. When the surface quantities fall within five percent of the sharp cone values, the effect of bluntness is assumed to have vanished. The same criterion is used for the case of ogive also.

First, the results for a 5° sharp cone at Mach 10 are compared in Figs. 5.1 - 5.4 with the results of inviscid and laminar theory to validate the numerical procedure as well as to justify the assumption of smallest nose radius cone as a sharp cone. Next the results for the wall quantities are presented for various Mach numbers and cone angles in Figs. 5.5 - 5.12. The effects of Reynolds number on the wall quantities are presented in Figs. 5.13 - 5.16. Similar results for ogives are presented in Figs. 5.17 - 5.23 for wall and flow field quantities.

The numerical results are validated by comparing the surface pressure and shock standoff distance with the inviscid theory in Figs. 5.1 and 5.2. The pressure has been nondimensionalized with respect to the freestream pressure and the shock standoff distance with respect to the nose radius. The x distance is measured from the virtual tip of the sharp cone. The results are plotted from the tangency point onward. The skin friction and the heat transfer coefficient are compared with the laminar theory in Figs. 5.3 and 5.4. These figures show an excellent comparison. The theoretical results are valid for sharp nose cone only, while the numerical calculations were performed for smallest nose radius cone. Except very close to the nose, the results agree with the sharp cone results. So the assumption of smallest nose radius as sharp cone is valid slightly downstream of the nose.

Figures 5.5 - 5.8 show the variation of surface quantities with the axial distance for a 5° cone with various degree of bluntness and for freestream Mach numbers of 10 and 20. The surface pressure distributions are presented in Fig. 5.5. In the stagnation region, the pressure is very high but as the flow moves downstream, the shock strength decreases thereby decreasing the pressure. The flow overexpands near the shoulder; the extent of overexpansion is a function of the bluntness and freestream conditions. The overexpanded flow then recompresses back to the sharp cone value. The distance it takes to reach the sharp cone value is also a function of the freestream conditions and nose bluntness. It should be

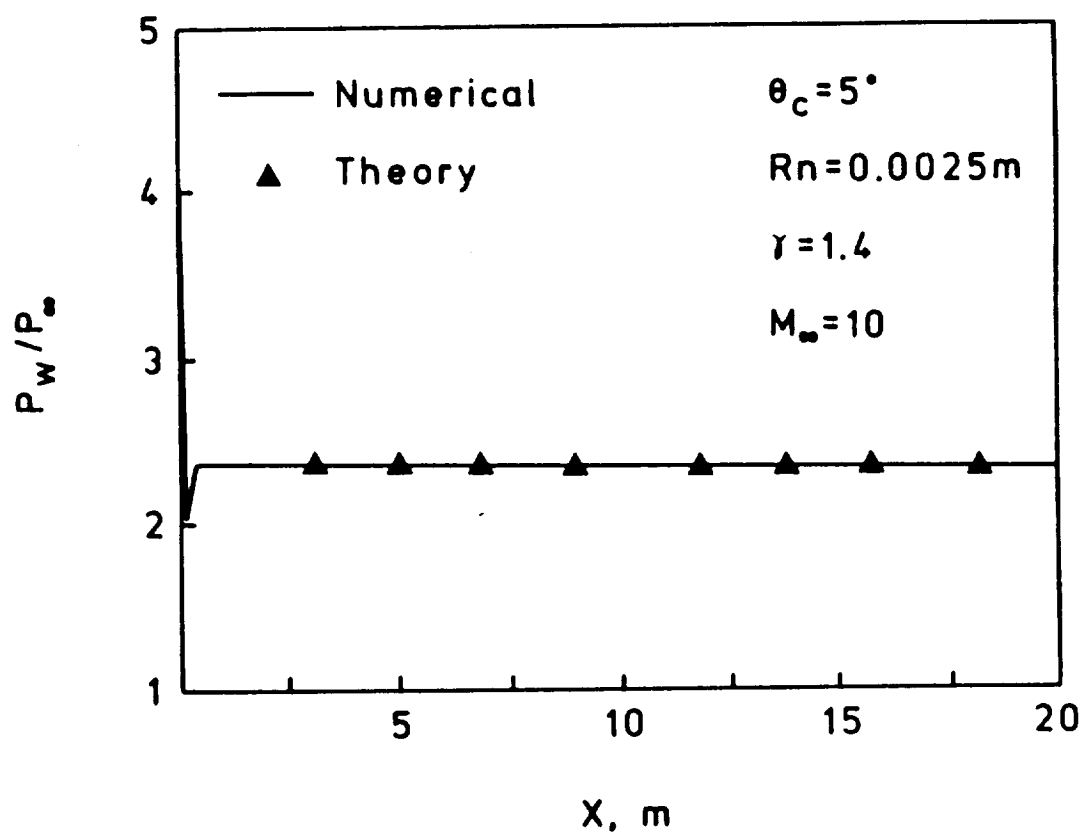


Fig. 5.1 Comparison of wall pressure with the inviscid theory.

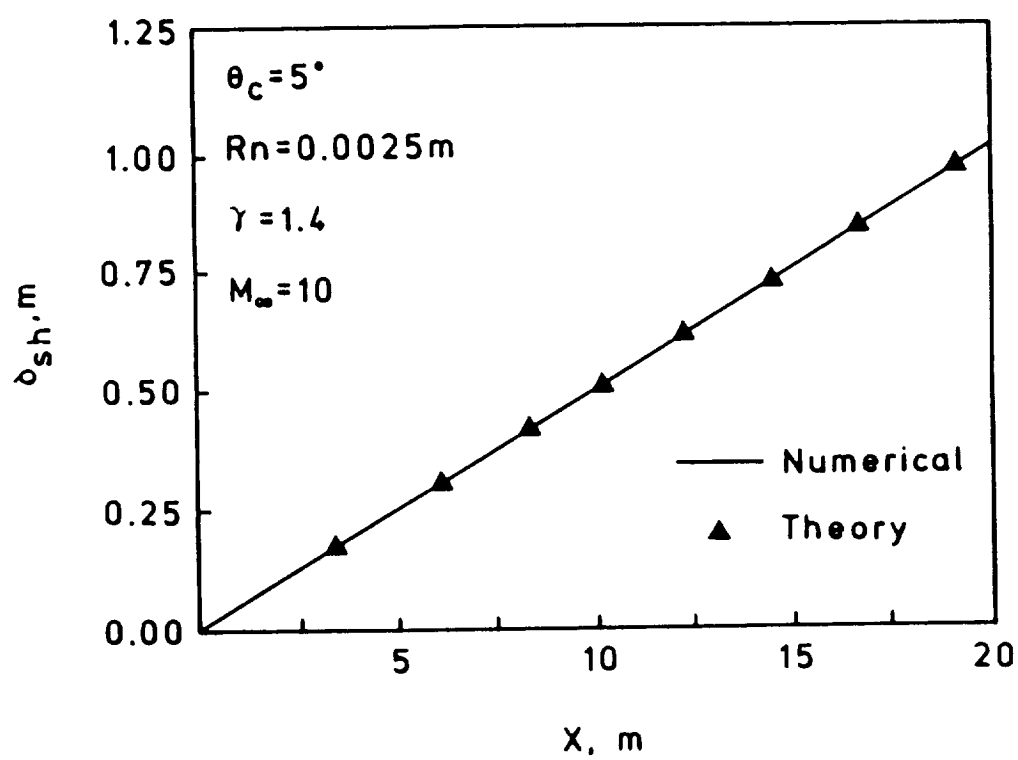


Fig. 5.2 Comparison of shock standoff distance with the inviscid theory.

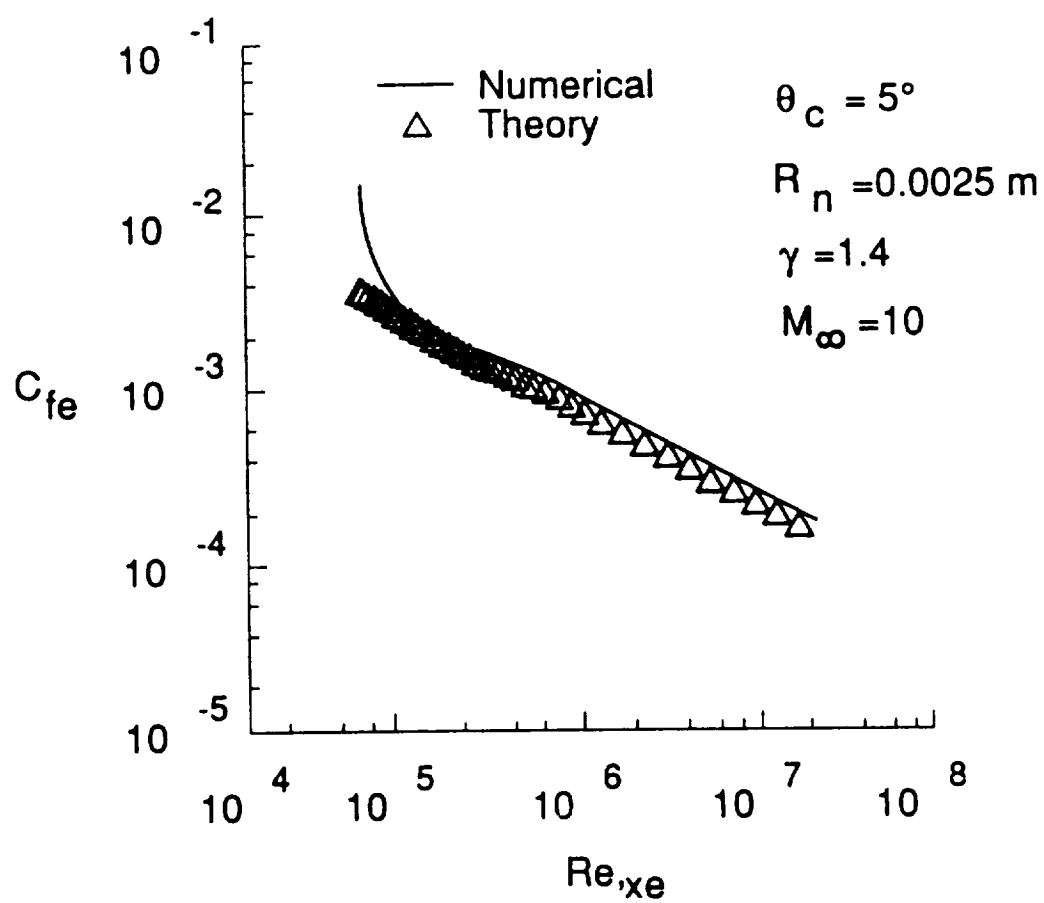


Fig. 5.3 Comparison of skin friction coefficient with the laminar theory.

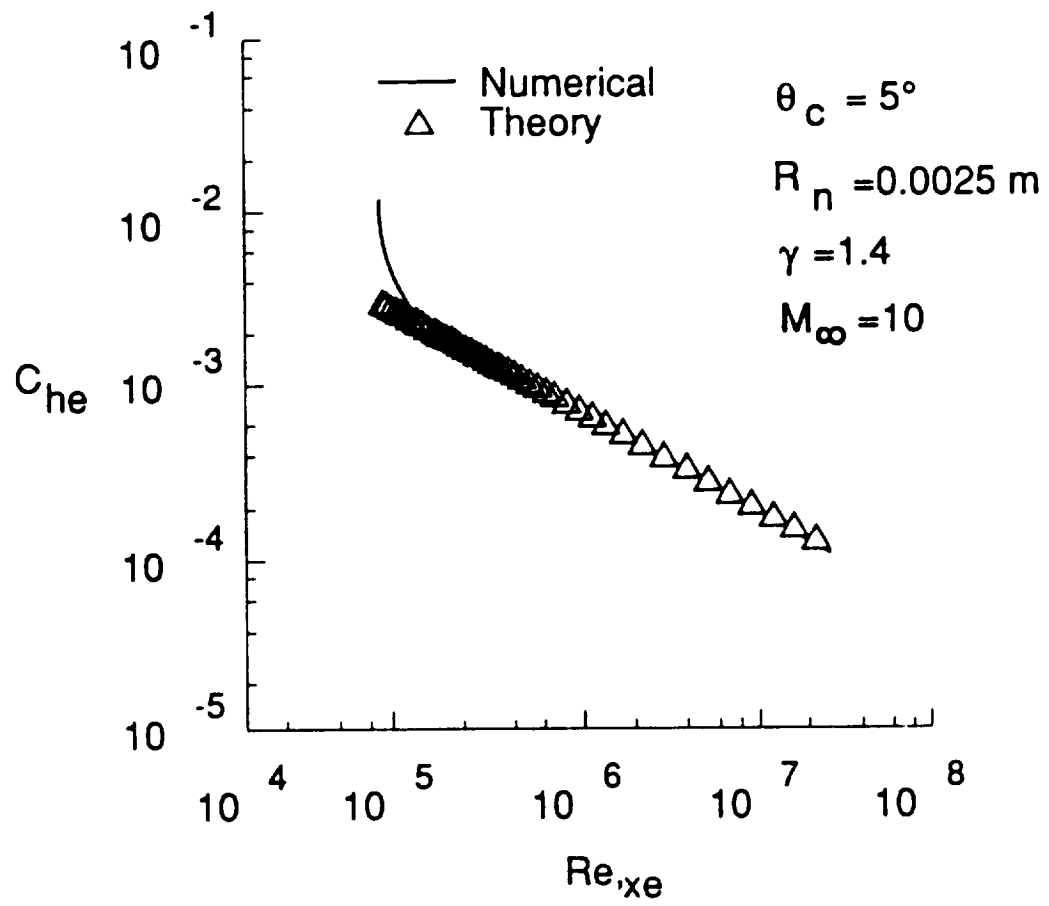


Fig. 5.4 Comparison of heat transfer coefficient with the laminar theory.

Table 5.1 Flow conditions for the forebody calculations

Quantity	$M_\infty = 10$	$M_\infty = 20$
$P_\infty, N/m^2$	404.7	171.0
T_∞, k	243.4	261.3
T_{wall}, k	1000	1000
Pr	0.72	0.72

noted that the pressure on the cone is influenced by the nose over a large portion of the afterbody and is lower than the conical pressure. For all values of leading edge bluntness considered, the surface pressures have reached the same value at about 160 nose radii downstream.

Figure 5.6 shows the variation of the shock standoff distance as a function of the axial distance. The shock standoff distances are measured from the body surface. Here the behavior of the shock shape is seen to be qualitatively similar to those observed by previous investigators [20]. The shock standoff distance is affected considerably by the leading edge bluntness. For the sharp cone, it is a straight line, while for blunted cones it is curved with inflection point about 50 nose radii downstream. For sufficiently large values of x , the shock shape becomes independent of the nose bluntness. At Mach 20, it takes less distance to attain conical value than at Mach 10.

The variation of the wall heat flux with axial distance is illustrated in Fig. 5.7 for various freestream conditions and bluntnesses. The wall heat flux has been nondimensionalized by $\rho_\infty U_\infty^3$. Figure 5.7 shows that the heating rates decrease over the body with increasing nose bluntness at a given Mach number. This is because heat transfer in the nose region is inversely proportional to the square root of the nose radius and decreases over the afterbody due to lower local pressure. The results again show that the sharp cone value is attained in a shorter distance for Mach 20 than for Mach 10. Comparing the distance it takes to attain the conical value for pressure and heat flux, it is noted that it takes almost the same distance for both. Since (to a reasonable accuracy) the pressure can be predicated analytically by using various correlations, it appears that the merging distance for heat transfer can be estimated without calculating the detailed flow field.

Variation of the skin friction coefficient with the axial distance is shown in Fig. 5.8. The skin friction is zero at the stagnation point, it increases around the

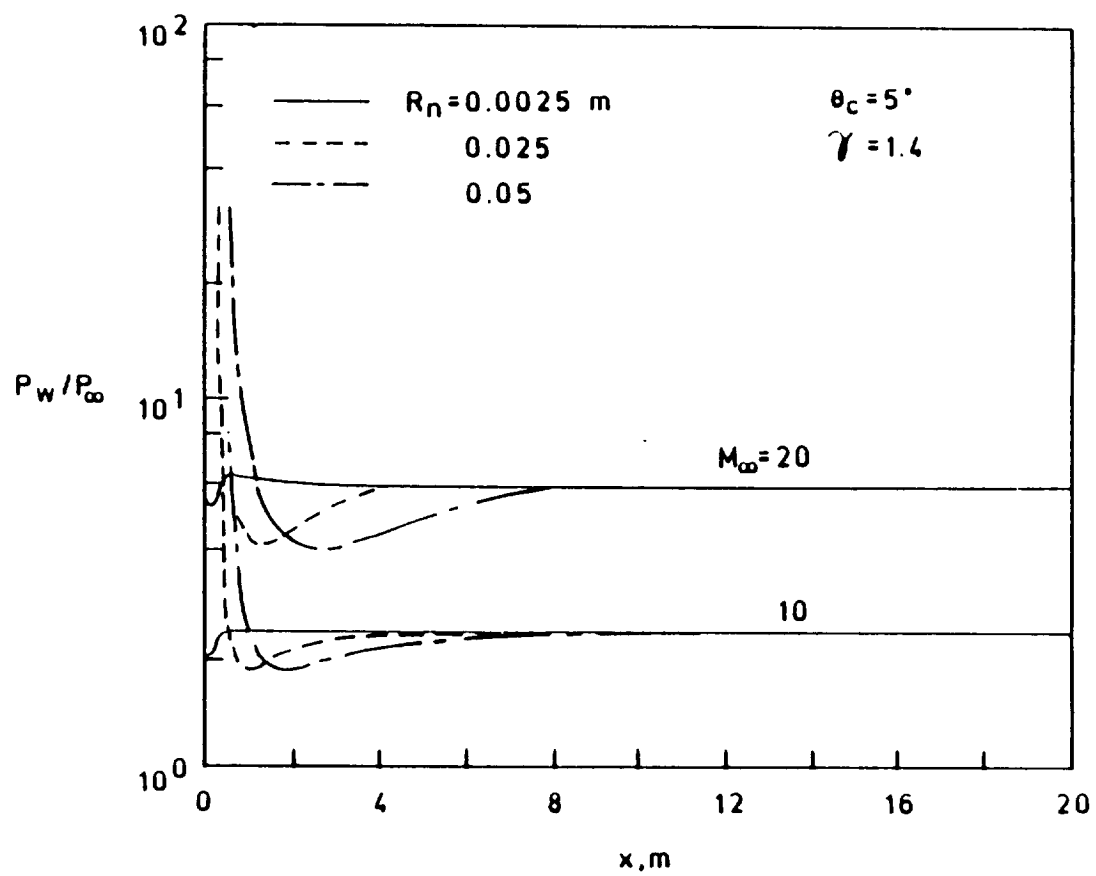


Fig. 5.5 Variation of wall pressure with the axial distance for $\theta_c = 5^\circ$ at various Mach numbers.

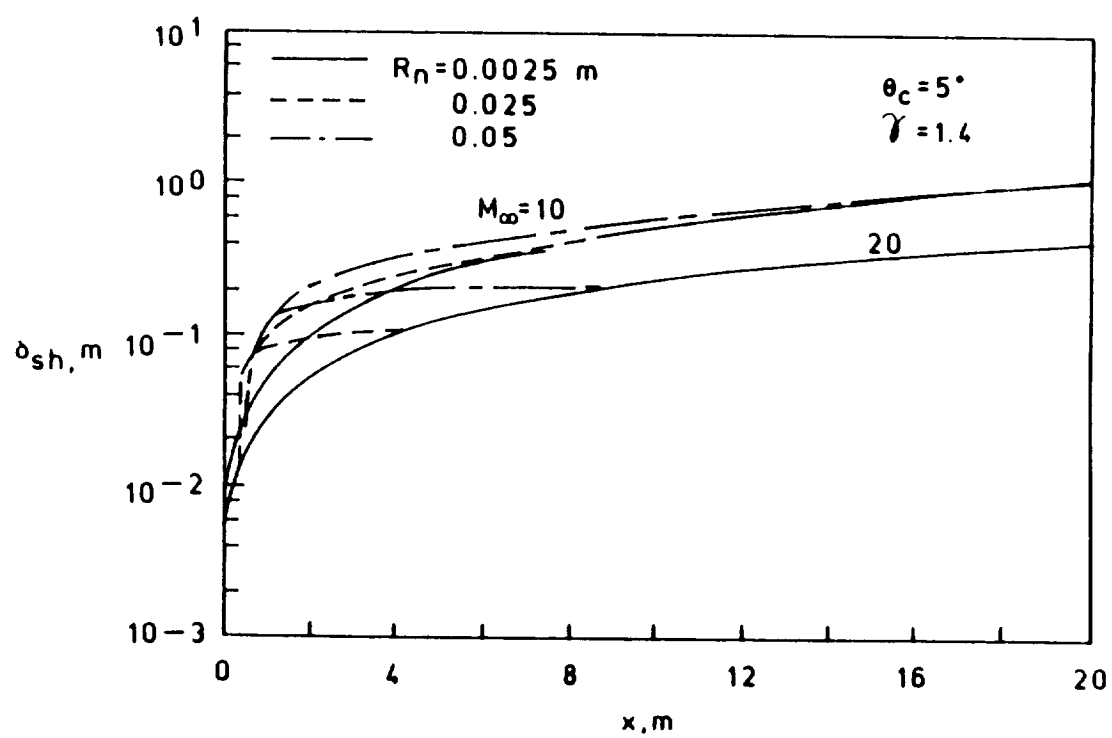


Fig. 5.6 Variation of shock standoff distance with the axial distance for $\theta_c = 5^\circ$ at various Mach numbers.

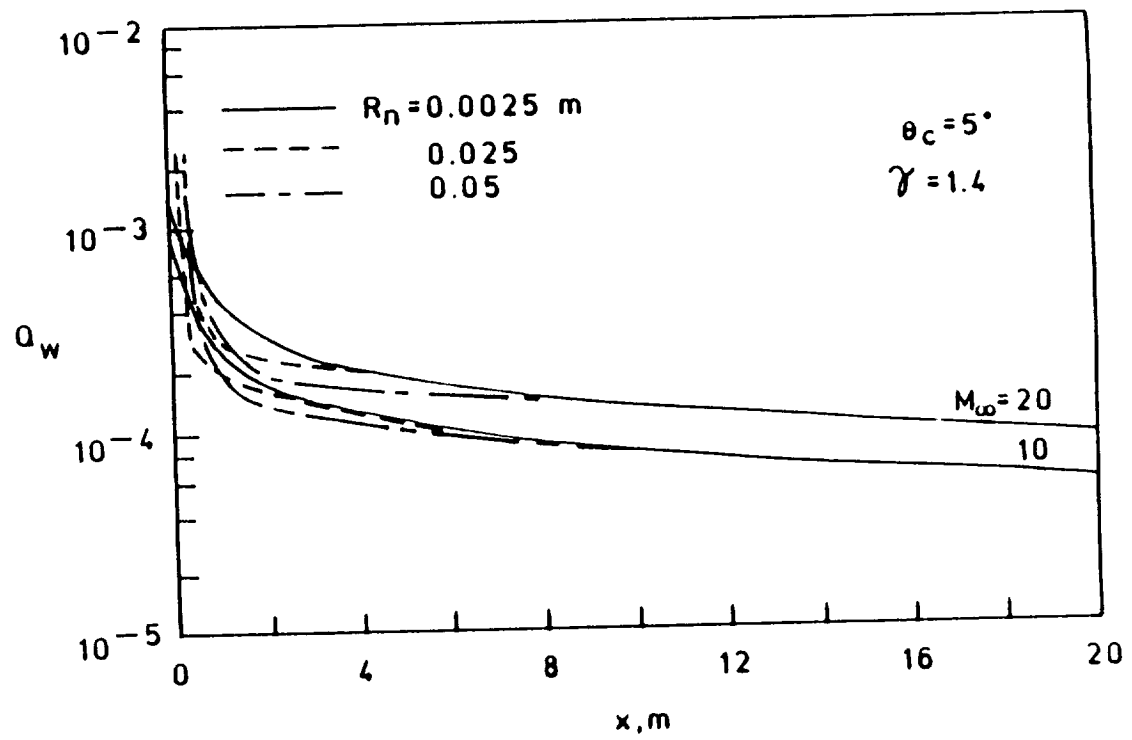


Fig. 5.7 Variation of wall heat transfer with the axial distance for $\theta_c = 5^\circ$ at various Mach numbers.

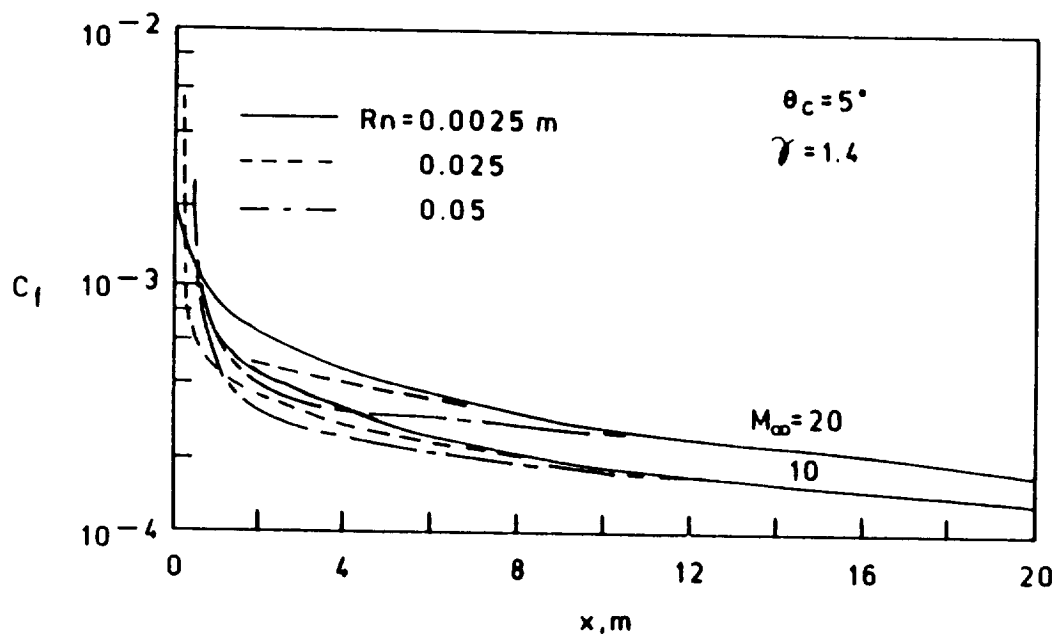


Fig. 5.8 Variation of skin friction with the axial distance for $\theta_c = 5^\circ$ at various Mach numbers.

nose, reaches a maximum and decreases further downstream. It follows the same general trend as the wall heat flux over the afterbody. Figure 5.8 shows that the skin friction decreases over the body with increasing nose bluntness at a given Mach number. This is because the entropy layer increases the thickness of the boundary layer, thereby reducing the gradients of velocity profile near the body. The skin friction is found to be most sensitive to the nose bluntness as it takes maximum distance to reach the sharp cone value among all the flow properties.

A comparison of the entropy swallowing distance with the results of Rotta [50] for Mach 10 freestream conditions (Table 5.1) is given in Table 5.2 for various nose bluntness and Reynolds numbers. The table shows a large difference between the present results and the empirical results of Rotta. This difference increases with the increasing bluntness. The calculated entropy swallowing distance agrees with the merging distance for skin friction, surface pressure, wall heat transfer and shock shape. As mentioned earlier, the discrepancy between the two is due to the assumption of constant pressure on the conical portion of the body. This causes the overestimation of the entropy swallowing distance. For small bluntness, the overexpansion can be neglected. Thus, Rotta's results are valid only for very small values of nose bluntness. The distances to attain conical values of surface pressure, shock standoff distance, wall heat transfer and skin friction are given in Tables 5.3 and 5.4. The effects of cone angle has been investigated for a freestream Mach number of 20 and cone angles of 5° , 10° and 20° . Some results for surface quantities are presented in Figs. 5.9 - 5.12. An interesting general trend is noticed from these figures. With a small increase in cone angle from 5° to 10° , the merging distances decrease dramatically. The merging distances decrease even more when the cone angle is increased from 10° to 20° . This decrease in merging distance can be attributed to the increase in shock angle with increasing cone angle thereby reducing the entropy layer thickness.

Table 5.2 Entropy swallowing distance (x/R_n) for 5° cone at $M_\infty = 10$

R_n	Reynolds No.	Present	Rotta
0.0025	2891	139	224
0.025	14454	206	375
	22908	243	470
	57816	286	590
0.05	57816	288	590

Table 5.3 Distance (x/R_n) up to which bluntness effect persist for $M_\infty = 10$

Quantity	R_n, m	$\theta_c = 5^\circ$	Ogive ($\gamma = 1.4$)
P_w	0.025	120	47
	0.05	160	48
δ_{sh}	0.025	209	63
	0.05	218	71
C_f	0.025	233	127
	0.05	267	154
Q_w	0.025	120	44
	0.05	160	48

Table 5.4 Distance (x/R_n) up to which bluntness effect persist for $M_\infty = 20$

Quantity	R_n, m	$\theta_c = 5^\circ$	$\theta_c = 10^\circ$	$\theta_c = 20^\circ$	Ogive ($\gamma = 1.4$)	Ogive (EQUIL)
P_w	0.025	123	38	9	48	38
	0.05	146	40	15	52	40
δ_{sh}	0.025	172	43	10	57	44
	0.05	182	45	11	67	50
C_f	0.025	165	80	25	87	65
	0.05	198	108	35	121	119
Q_w	0.025	126	37	10	46	36
	0.05	135	40	18	50	37

The variation in the wall pressure with axial distance for various cone angles is shown in Fig. 5.9. The wall pressure increases with the increasing cone angle due to increased shock strength. Also the overexpansion/recompression increases with the cone angle while the physical distance over which this takes place decreases. Thus a blunt cone with a larger cone angle will experience a constant wall pressure over most of its surface as compared to a cone with a smaller angle. Figure 5.10 shows the variation of shock standoff distance with the axial distance for 20° cone. The shock standoff distance decreases with the increasing cone angle over forward portion. Also the distance it takes to attain conical value decreases with the increasing cone angle. Figure 5.11 shows the variation of wall heat transfer for various cone angles. It is seen that the heat transfer on the wall increases with increasing cone angle while merging distances decrease. Thus larger angle cones will experience almost uniform heat transfer over most of the afterbody. Similar behavior can be seen for the skin friction in Fig. 5.12. These results indicate that as the cone angle increases the extent of effects of nose bluntness decreases.

The variation of the wall quantities with the Reynolds number is shown in Figs. 5.13 - 5.16. In order to change the Reynolds number, the nose bluntness is kept constant as 0.025m, while the freestream pressure is changed. The Reynolds number is based on the nose radius. The variation of wall pressure and shock standoff distance is shown in Figs. 5.13 and 5.14. As expected, these quantities were found to be independent of the Reynolds number. The variation of the wall heat transfer and the skin friction is shown in Figs. 5.15 and 5.16. A large variation can be seen with increasing Reynolds number. With increasing Reynolds number, the skin friction and the heat transfer decrease. This is in agreement with the laminar theory which states that C_f and C_h are inversely proportional to \sqrt{Re} .

Figures 5.17 - 5.23 show the effect of nose bluntness on ogive. Calculations have been made for three nose bluntnesses and two freestream conditions. Qualitatively,

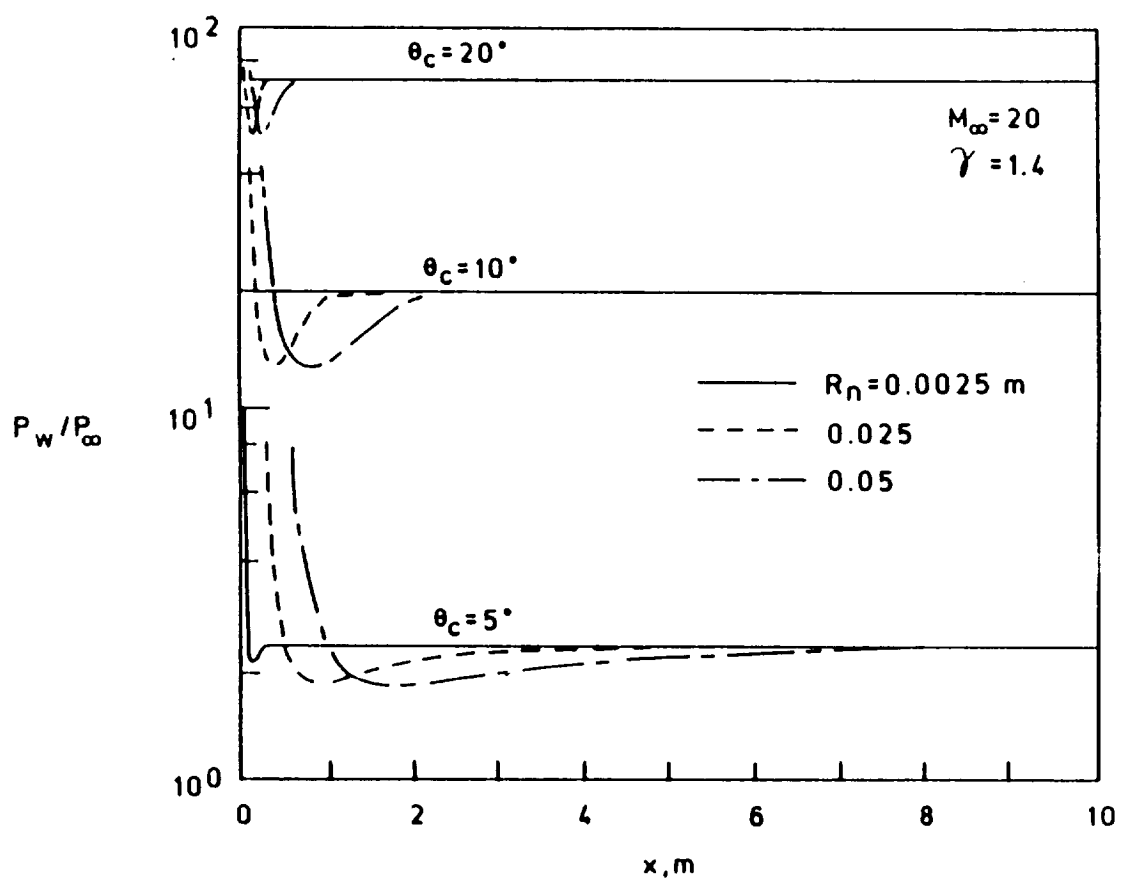


Fig. 5.9 Variation of wall pressure with the axial distance for $\theta_c = 5^\circ, 10^\circ$ and 20° at $M_\infty = 20$.

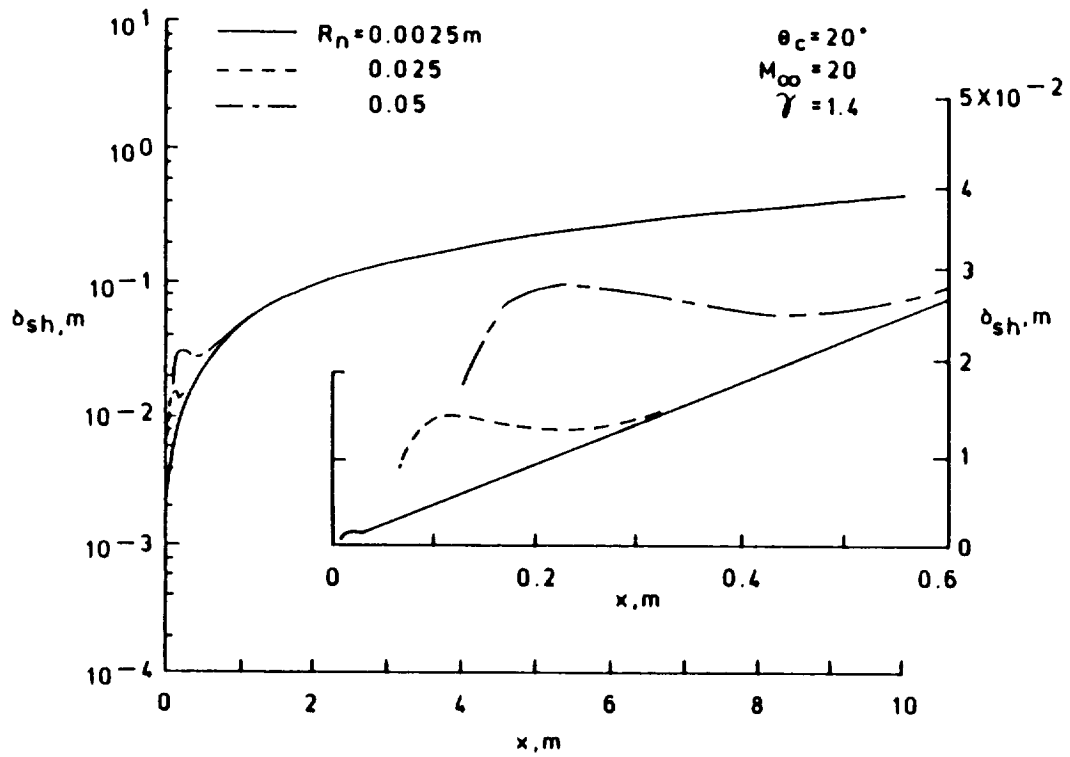


Fig. 5.10 Variation of shock standoff distance with the axial distance for $\theta_c = 20^\circ$ at $M_\infty = 20$.

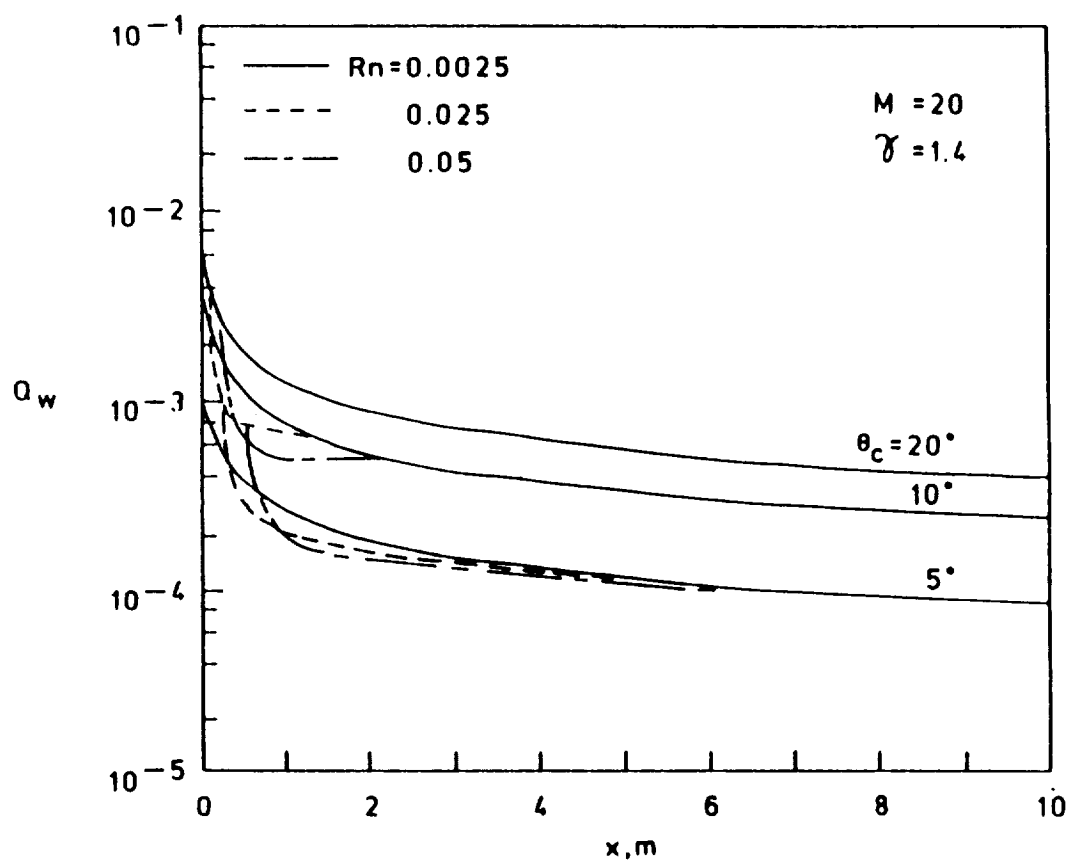


Fig. 5.11 Variation of wall heat transfer with the axial distance for $\theta_c = 5^\circ, 10^\circ$ and 20° at $M_\infty = 20$.

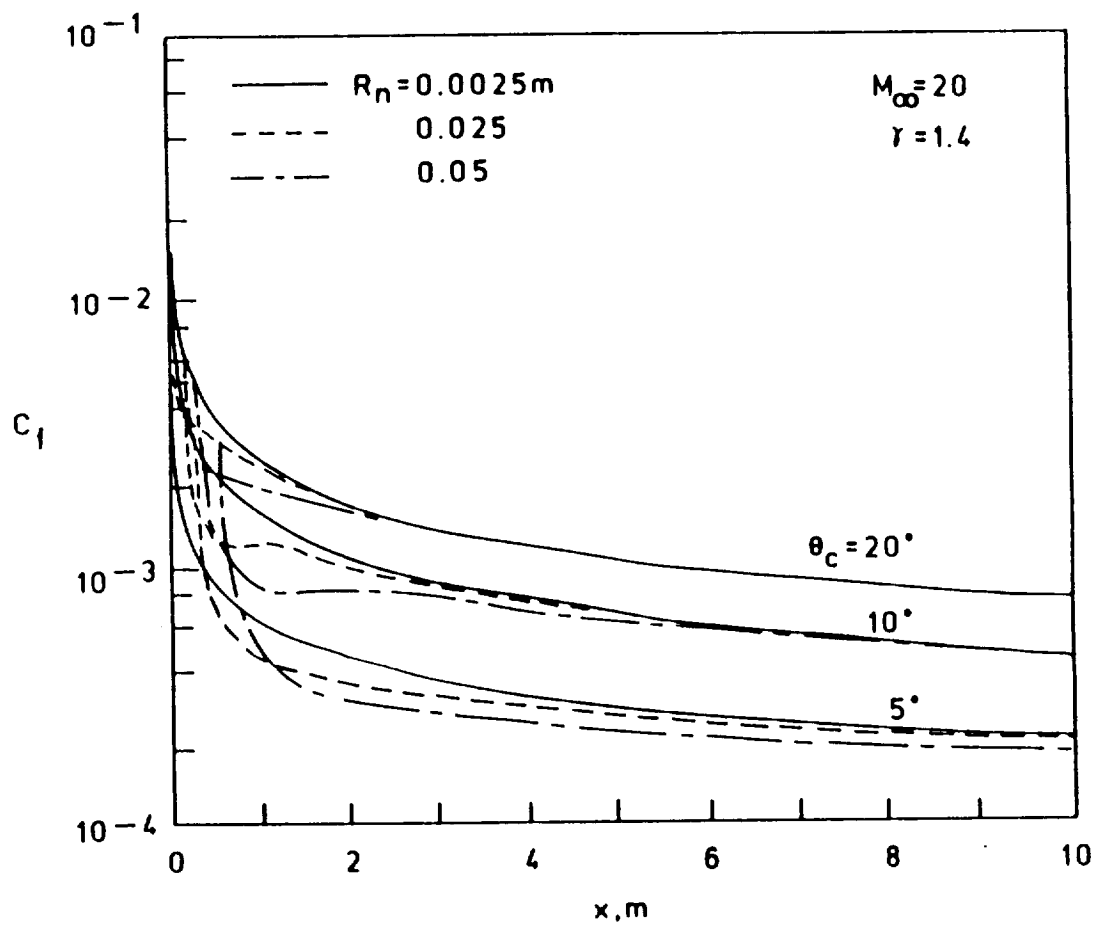


Fig. 5.12 Variation of skin friction with the axial distance for $\theta_c = 5^\circ, 10^\circ$ and 20° at $M_\infty = 20$.

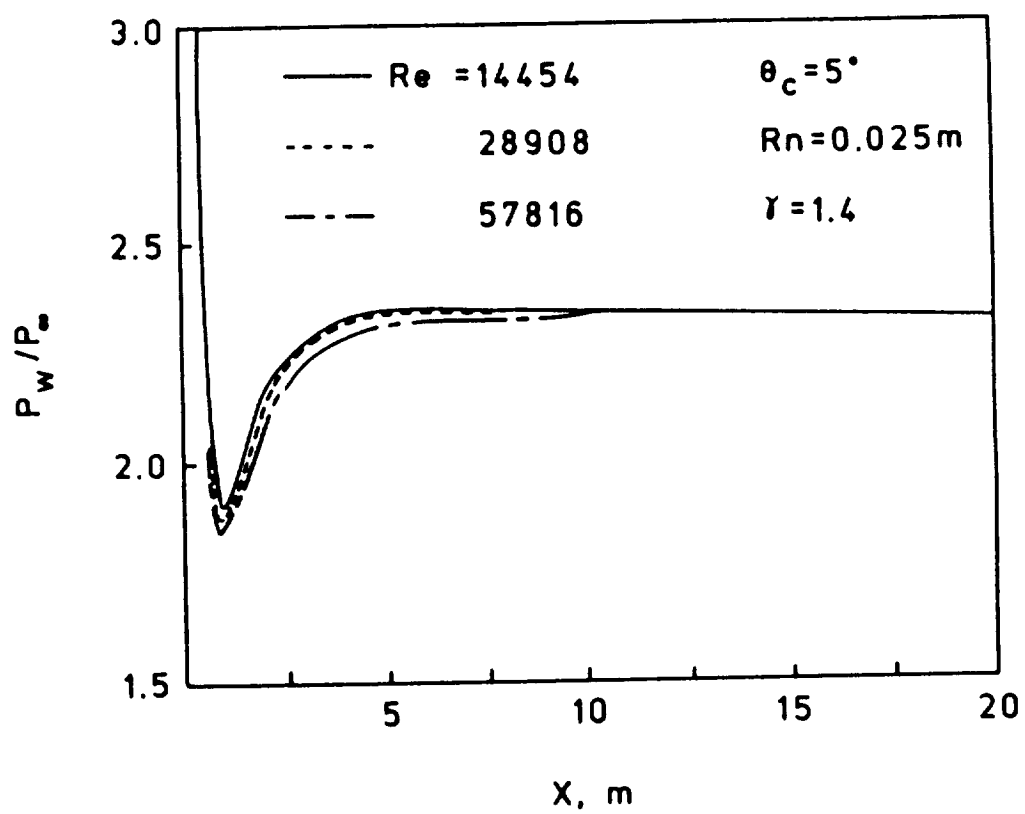


Fig. 5.13 Variation of wall pressure with the axial distance for $\theta_c = 5^\circ$ at various Reynolds numbers.

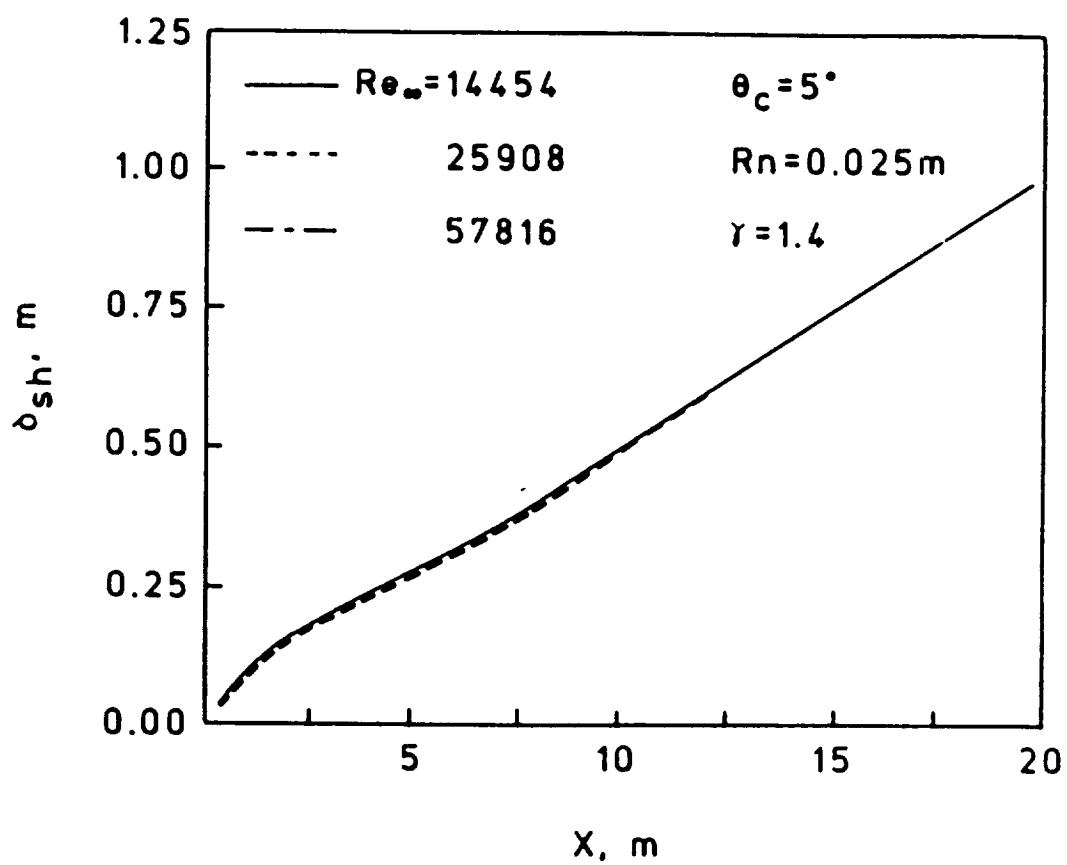


Fig. 5.14 Variation of shock standoff distance with the axial distance for $\theta_c = 5^\circ$ at various Reynolds numbers.

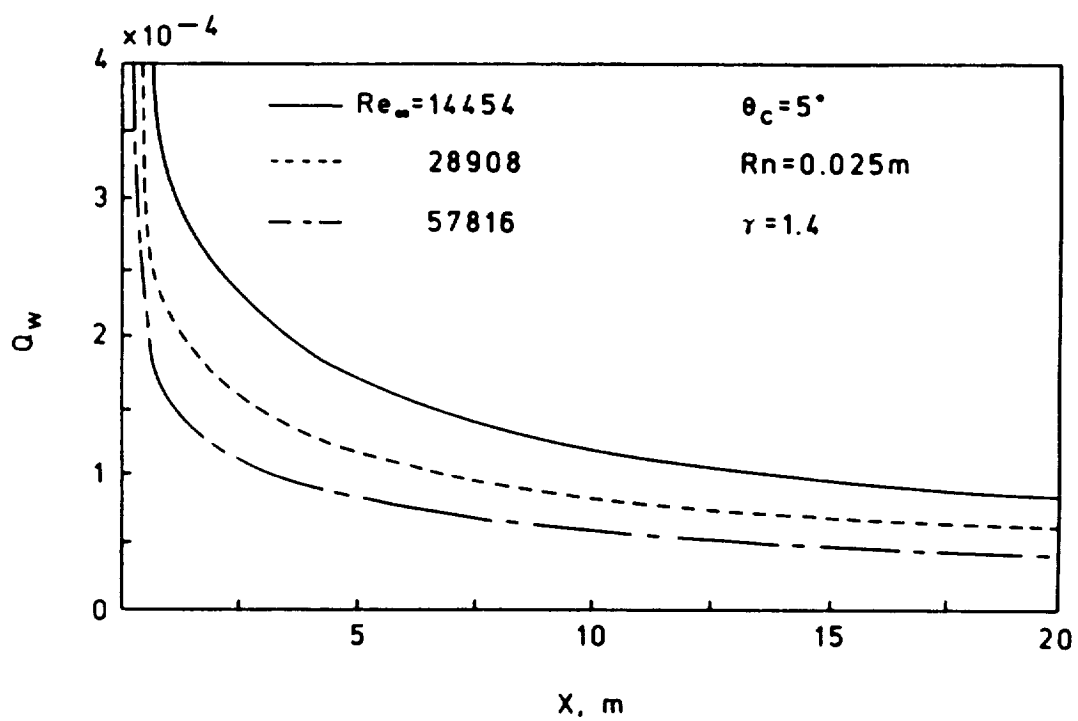


Fig. 5.15 Variation of wall heat transfer with the axial distance for $\theta_c = 5^\circ$ at various Reynolds numbers.

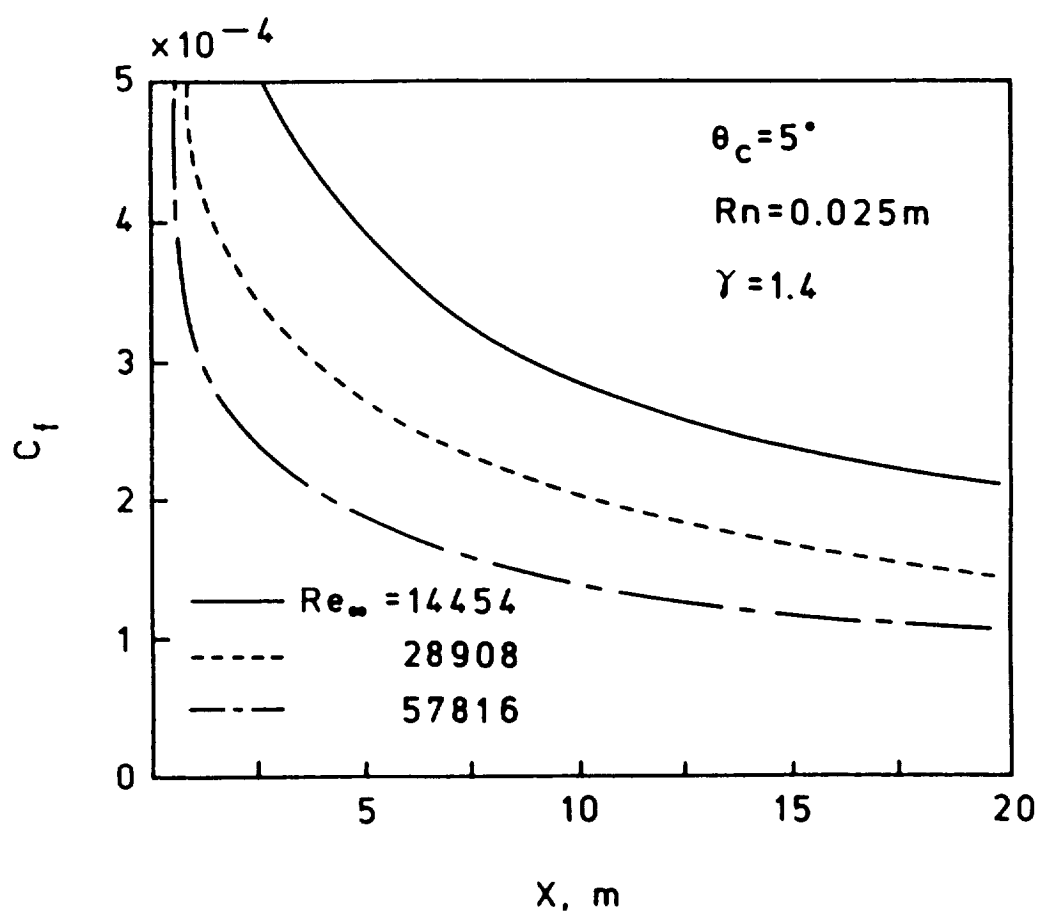


Fig. 5.16 Variation of skin friction with the axial distance for $\theta_c = 5^\circ$ at various Reynolds numbers.

these results are very similar to those for the cone, although the merging distances have decreased. These results are also given in Tables 5.3 and 5.4. The variation of wall pressure with axial distance is shown in Fig. 5.17. Here, the sharp ogive values are reached earlier than sharp cone values. Unlike cone, the pressure in this case does not attain a constant value but decreases gradually with a constant slope. The bluntness effects vanish earlier for Mach 20 than for Mach 10 and the region influenced by the nose has a lower pressure than that on a sharp body. Figure 5.18 shows the variation of the shock standoff distance. As expected, the shock is closer to the body for Mach 20 than for Mach 10. The skin friction and wall heat transfer are shown in Figs. 5.19 and 5.20 respectively. In this case also the skin friction is found to be most sensitive to the nose bluntness. It is the last quantity to attain the sharp ogive values.

Figure 5.21 compares the variation of the wall pressure at $M_\infty = 20$ for 5° and 10° cone with the ogive for two values of nose bluntnesses. The wall pressure for the cone attain a constant value irrespective of the cone angle and bluntness at certain distance downstream. But for the case of ogive, the pressure continuously decreases, i.e., it does not attain a constant value as in the case of cone for the range of axial distances considered in the present study.

Figures 5.22 and 5.23 show the variation of the streamwise velocity and temperature as a function of y distance for Mach 20 perfect gas flow over an ogive with various nose bluntnesses. It should be noted that since the shock fitting procedure is used, the normal profiles are plotted within the shock layer only. The velocity and temperature have been nondimensionalized with respect to their freestream values. The variation of streamwise velocity is shown in Fig. 5.22 for $x = 0.5, 1.0$, and 5.0 m. There is a significant difference between the profiles near the nose; differences tend to diminish with increasing axial distance. The figure shows that the thickness of the boundary layer increases with increasing bluntness and the shape of

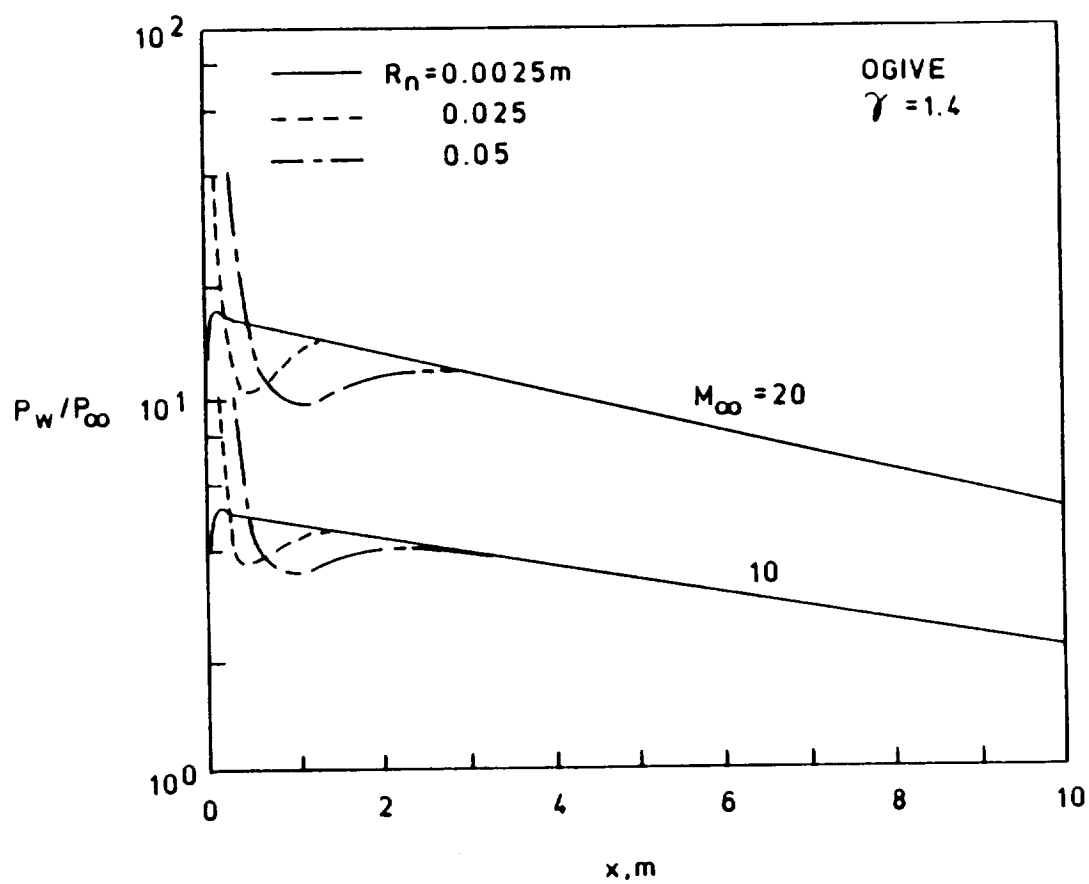


Fig. 5.17 Variation of wall pressure with the axial distance for ogive at various Mach numbers.

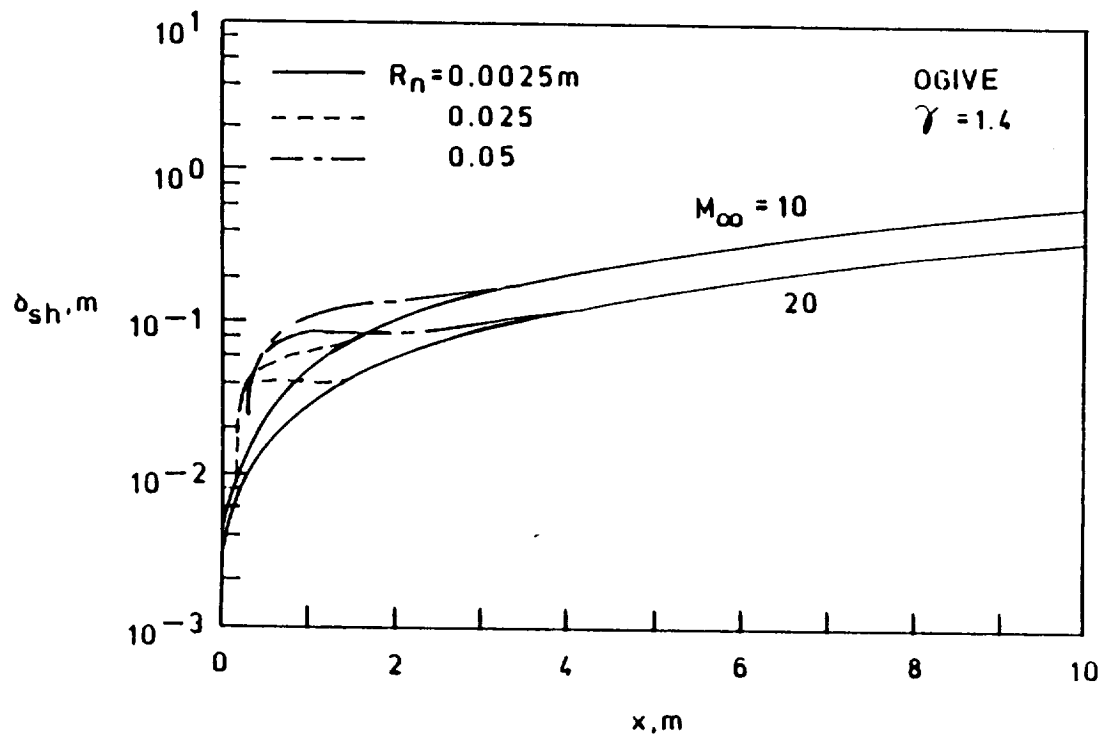


Fig. 5.18 Variation of shock standoff distance with the axial distance for ogive at various Mach numbers.

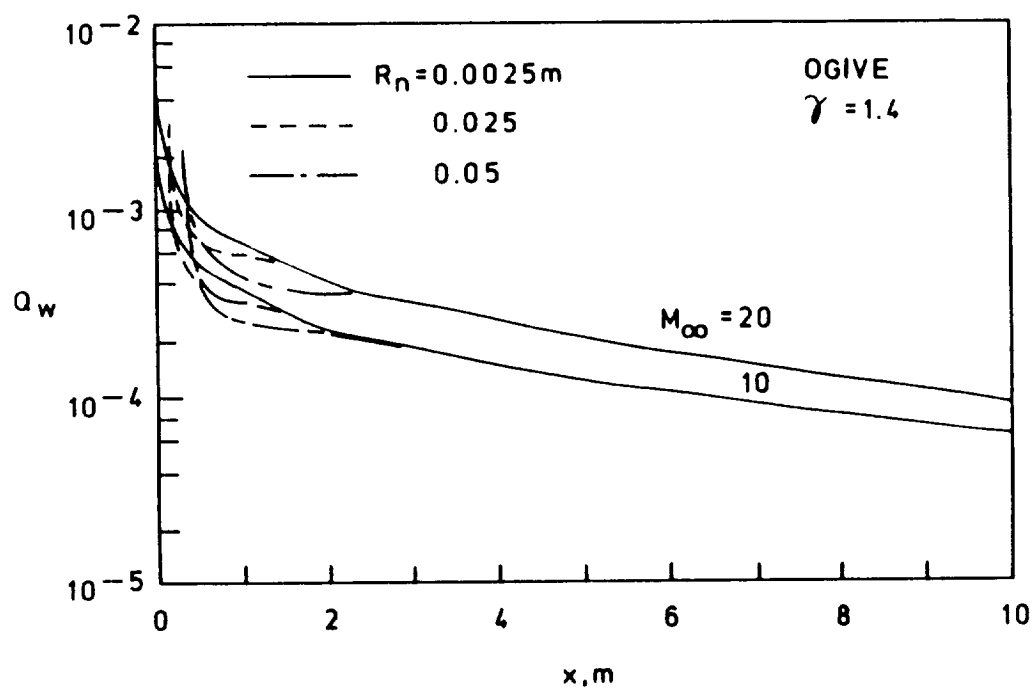


Fig. 5.19 Variation of wall heat transfer with the axial distance for ogive at various Mach numbers.

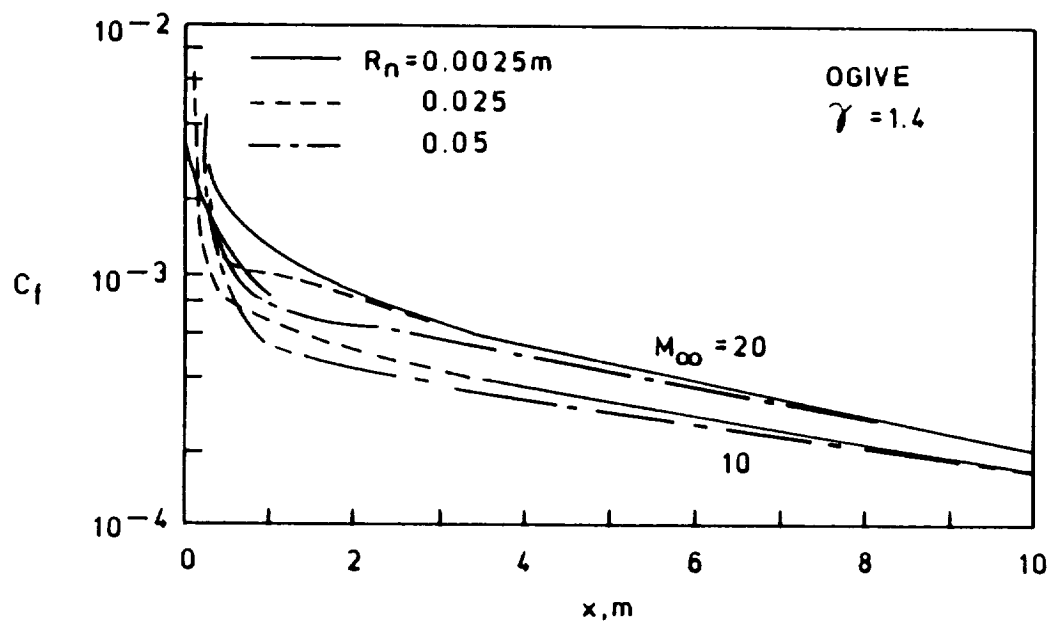


Fig. 5.20 Variation of skin friction with the axial distance for ogive at various Mach numbers.

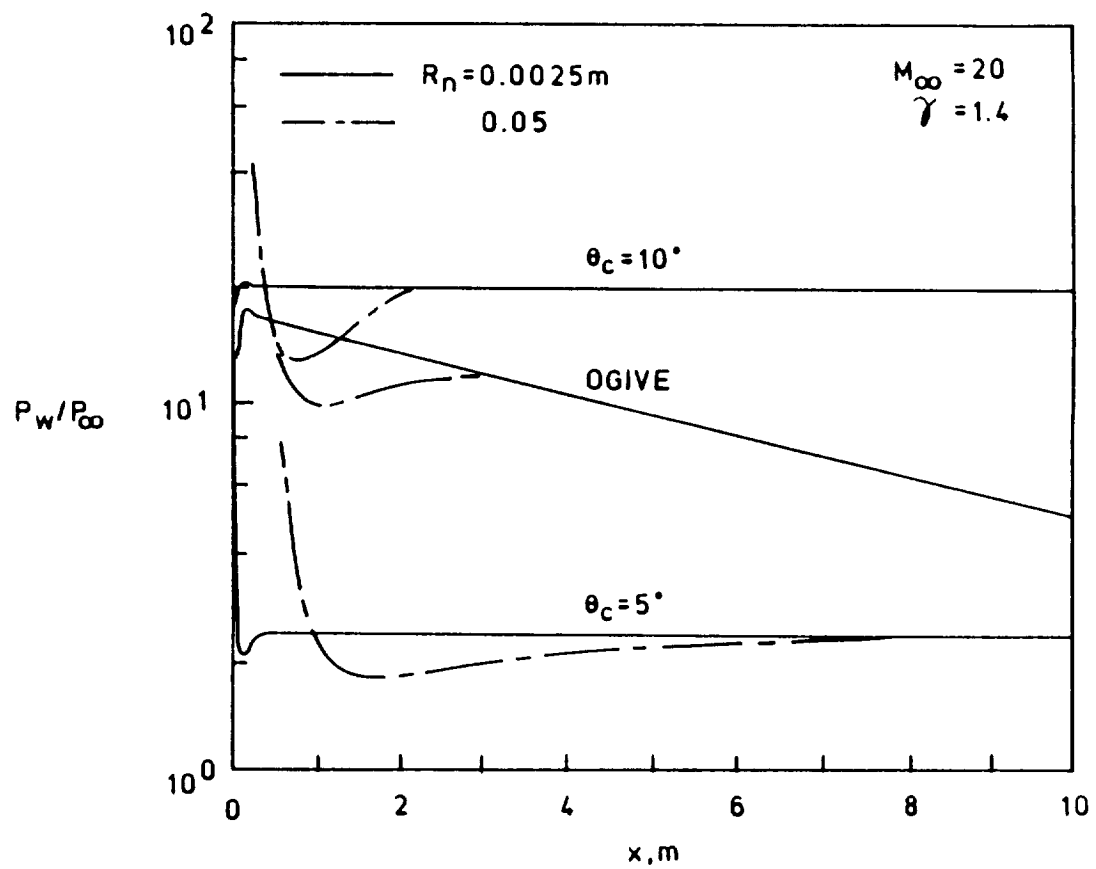


Fig. 5.21 Variation of wall pressure with the axial distance for $\theta_c = 10^\circ$, 20° and ogive at $M_\infty = 20$.

the profile is changed near the outer edge of the boundary layer. It is this difference which causes the wall values to be so different from the sharp cone values. The same type of effects can be seen in Fig. 5.23 where temperature profiles between the shock and the body are shown. Here again the differences decrease with the axial distance.

The results for perfect and equilibrium gas flows are shown in Figs. 5.24 - 5.28. The calculations were performed for Mach 10 and 20, but the results for Mach 10 were found to be identical for perfect and equilibrium gas, so only Mach 20 results are presented.

The variation of wall pressure, shock standoff distance, heat transfer, and skin friction at Mach 20 for ogive of 0.05m nose radius are shown in Figs. 5.24 - 5.27 for perfect and equilibrium gas flows. The equilibrium gas results do not show any dramatic differences from the perfect gas results although, as expected, there are some minor differences. The difference in two solutions tends to increase with increasing Mach number and bluntness. The most severe case is shown here. These figures show expected effects of equilibrium gas chemistry on the flow properties.

Figure 5.24 shows that the surface pressure variation is almost identical for the two cases, except in the recompression zone, where the equilibrium pressure is slightly higher than the perfect gas value due to higher density. The variation of shock standoff distance is shown in Fig. 5.25; the shock moves closer to the body for equilibrium flow calculations. The shock curvature is slightly reduced, thus the entropy generation is reduced too. This in turn, decreases the merging distances as can be seen in Table 5.4. The decrease in the shock standoff distance can be attributed to the increase in density of the gas behind the shock. The variation of the skin friction and the heat transfer is shown in Figs. 5.26 and 5.27 respectively. The skin friction is reduced slightly in the overexpansion zone but reverses its trend in the recompression zone before settling down to the perfect gas value where the

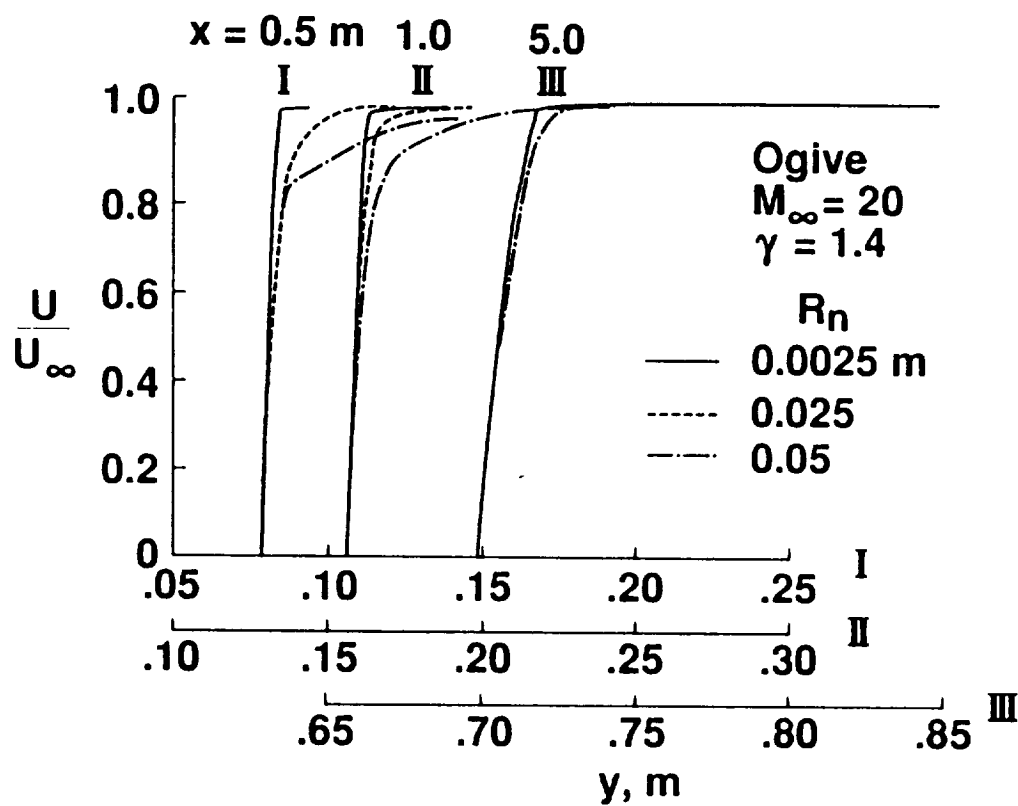


Fig. 5.22 Comparison of velocity profiles at $x = 0.5, 1.0$, and 5.0 m for ogive at Mach 20.

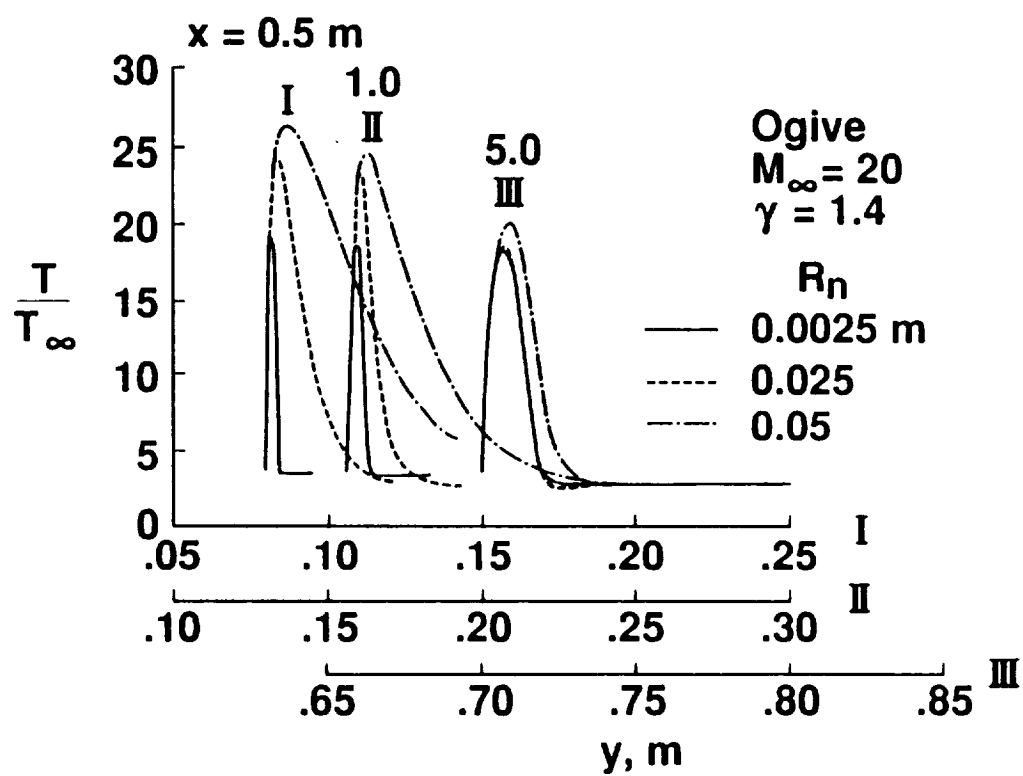


Fig. 5.23 Comparison of temperature profiles at $x = 0.5, 1.0$, and $5.0 m$ for ogive at Mach 20.

real gas effects are practically zero. In general, the real gas effects do not affect the wall quantities to any large extent for the present conditions. The only noticeable difference is for the case of shock standoff distance.

Figure 5.28 shows the effect of equilibrium gas chemistry on the temperature profile. It should be noted that even though the maximum temperature in the shock layer decreases for the equilibrium gas as compared to the perfect gas, the gradients near the wall do not change significantly and therefore the wall heat transfer is not affected much. The merging distances for these cases are given in Table 5.4. Due to the shock moving closer to the body, a small decrease in merging distances is noted for equilibrium flows.

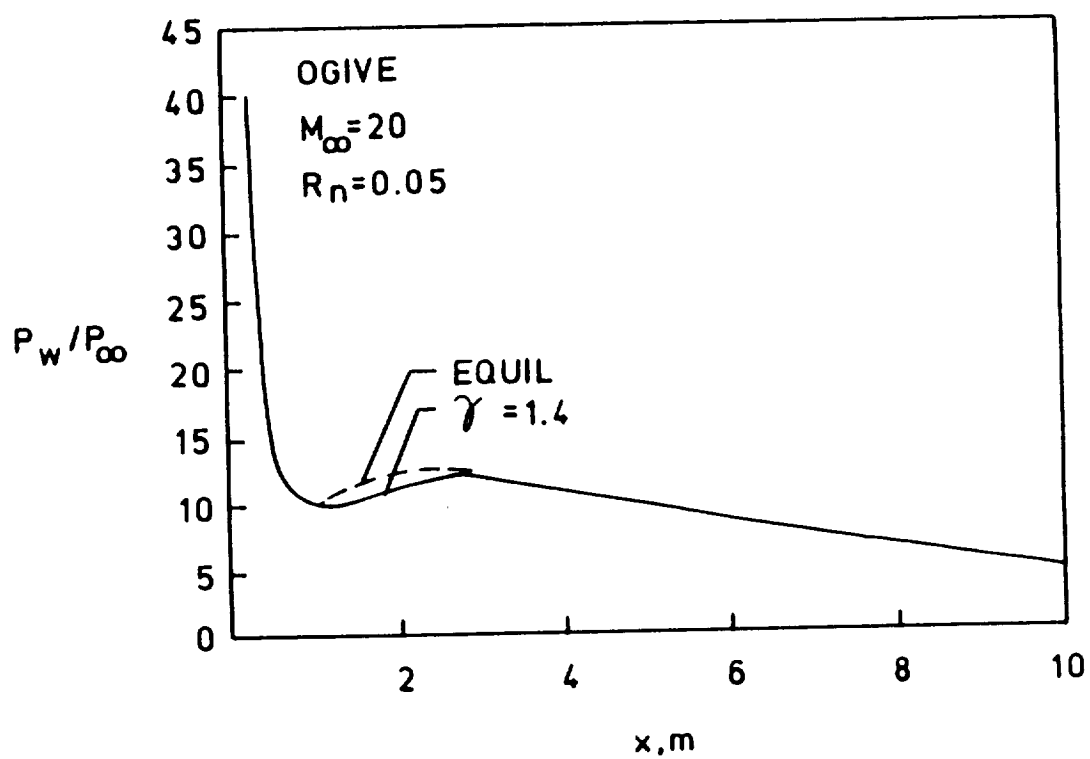


Fig. 5.24 Comparison of wall pressure for equilibrium and perfect gas.

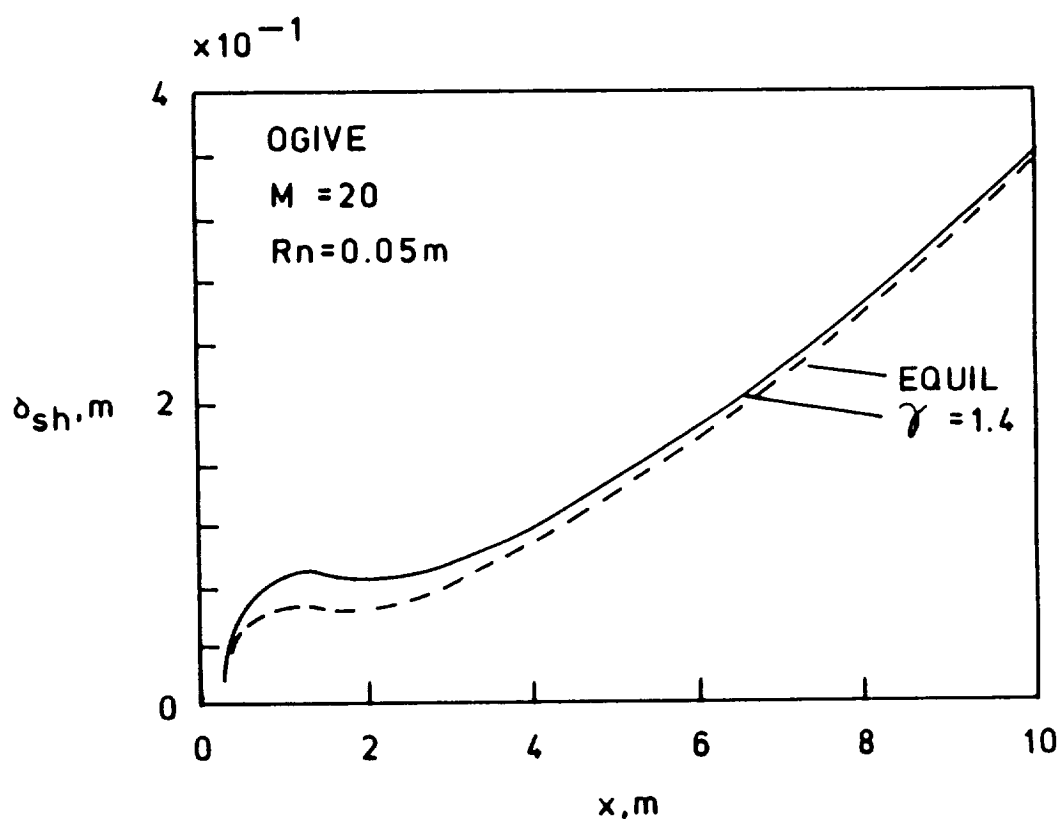


Fig. 5.25 Comparison of shock standoff for equilibrium and perfect gas.

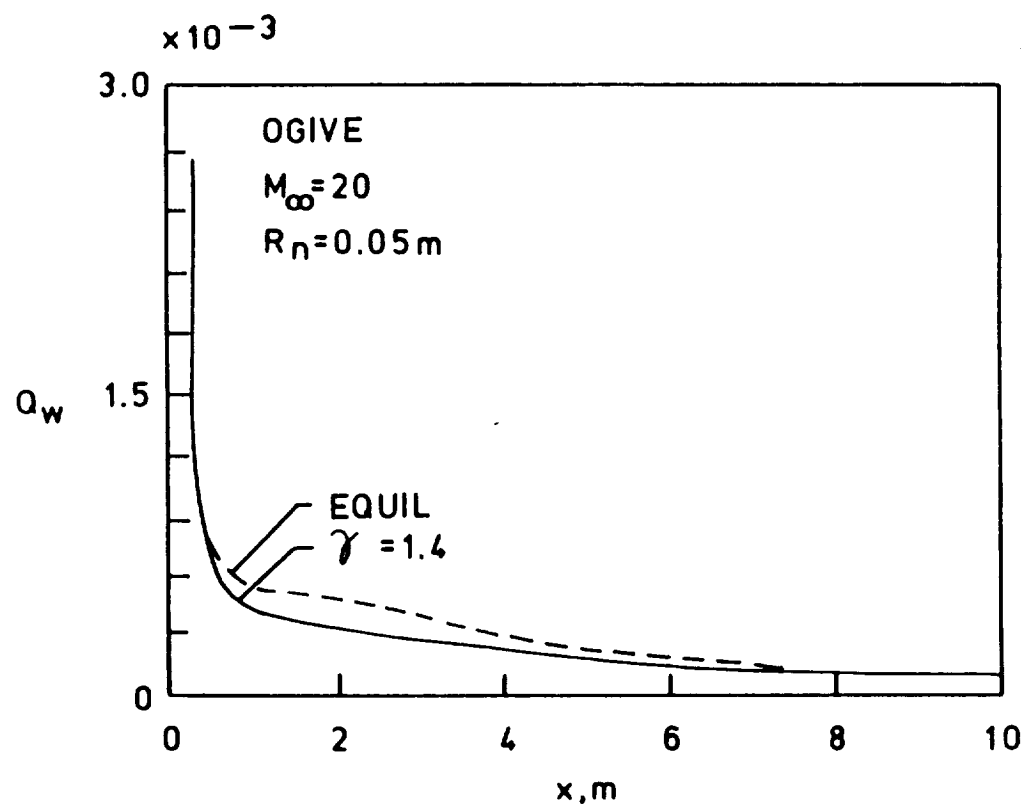


Fig. 5.26 Comparison of wall heat transfer equilibrium and perfect gas.

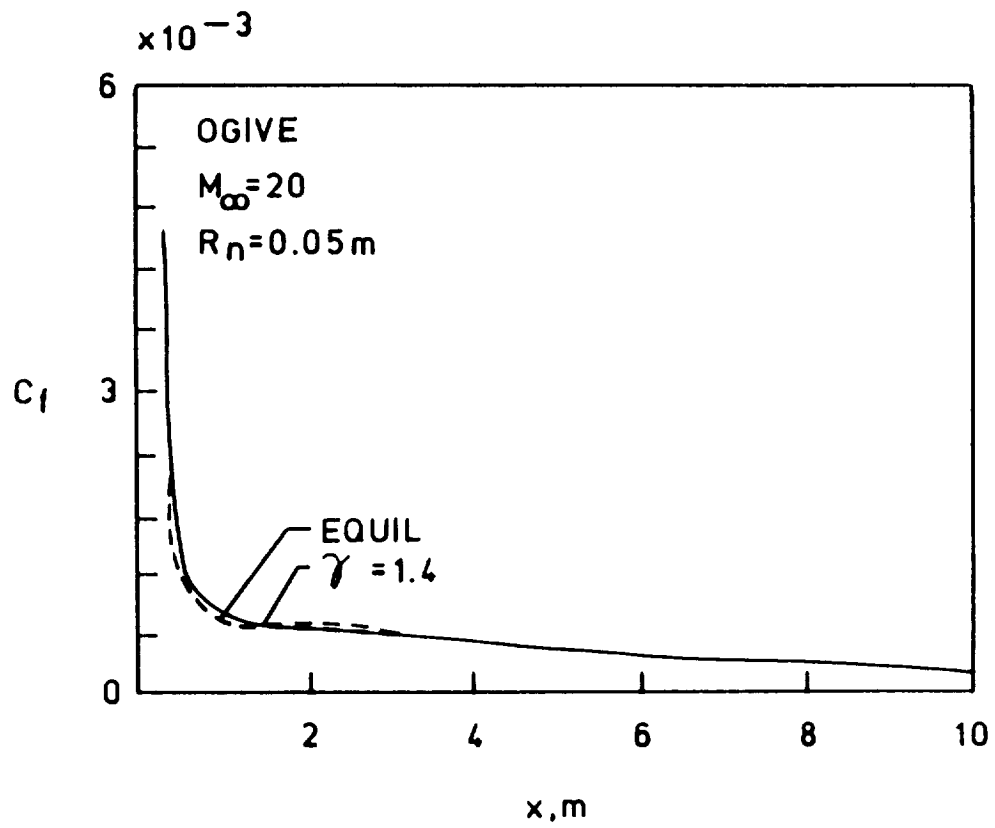


Fig. 5.27 Comparison of skin friction for equilibrium and perfect gas.

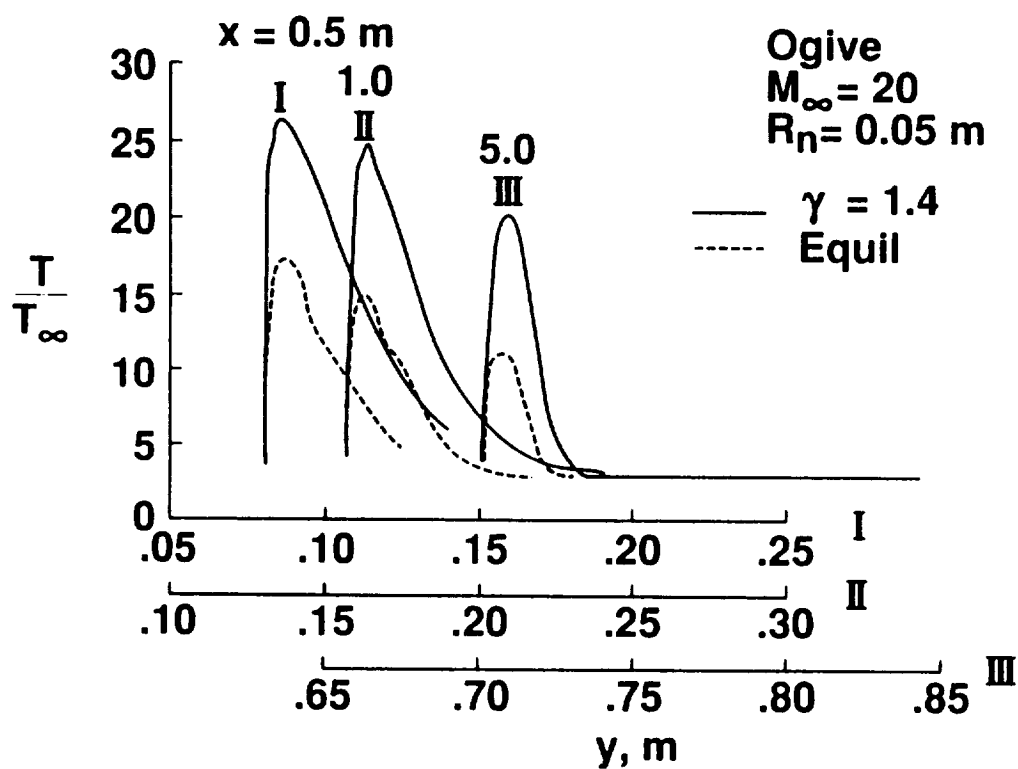


Fig. 5.28 Comparison of temperature profiles for equilibrium and perfect gas at $x = 0.5, 1.0$, and 5.0 m for ogive at Mach 20.

5.2 Forebody and the Cowl Shock Interaction

In this section the results of the forebody and the cowl shock interaction are discussed. A two-dimensional model is used to study the interaction. The computational domain is shown in Fig. 5.29; the solution over the whole domain is obtained in two steps. First, the cowl forebody solution is obtained using the Navier-Stokes equations. This solution is then used as the starting solution for the parabolized Navier-Stokes equations in the second step to calculate the extent of downstream effects of the shock-shock interaction into the inlet. Two sets of freestream conditions at Mach 8.03 and 5.94 (Table 5.5) are considered due to availability of the experimental data on the cowl forebody. However, no experimental data is available for the cowl afterbody. The results for Mach 8.03 are discussed first, followed by Mach 5.94 results. For all cases, the undisturbed blunt body flow was calculated first and this solution was then used as initial condition for shock impingement calculations. First the results are presented for unadapted grid and then with the adapted grid to show the importance of a suitable grid in obtaining improved solution.

Figures 5.30 - 5.33 show the temperature, Mach number, pressure, and density contours respectively for the cowl forebody at freestream Mach number 8.03 with unadapted grid shown previously in Fig. 4.10. The surface pressure and the heat transfer results are shown in Figs. 5.34 and 5.35 respectively. The improved results with adapted grid are shown in Figs. 5.36 - 5.43. The temperature and Mach number contours for the cowl afterbody are shown in Figs. 5.43 - 5.46. The variation of shock standoff and surface pressure on the cowl afterbody are shown in Figs. 5.47 and 5.48. The leeward and windward side computations were made independent of each other due to the two-dimensional nature of the flow. Similar calculations for Mach 5.94 are shown in Figs. 5.49 - 5.57. For this case the calculations were made for adapted grid only.

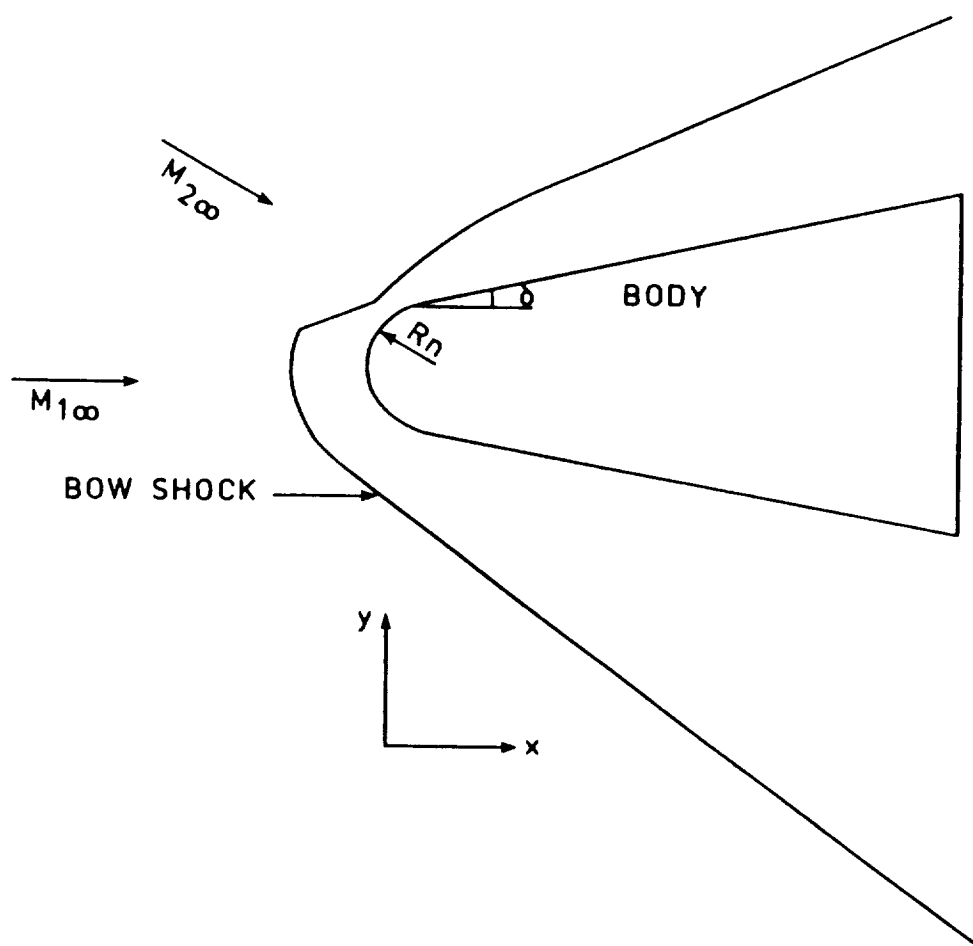


Fig. 5.29 Computational domain.

The temperature, Mach number, pressure, and density contours are shown in Figs. 5.30 - 5.33, respectively. The distorted bow shock is clearly evident in the figures. The bow shock has moved toward the body on the windward side and away from it on the leeward side. Here, the windward side is defined as the upper side where the flow passes through the impinging shock before encountering the body. The interaction of the bow shock and the impinging shock produces a supersonic jet surrounded by subsonic flows. The jet terminates with jet shocks and impinges on the body producing a local zone of very high pressure and heating rates. The stagnation point moves toward the windward side. The location of the stagnation point depends upon the strength and orientation of the impinging shock. Due to the coarseness of the grid away from the wall, the shocks and shear layers are smeared over several grid points.

The variation of wall pressure along the cowl forebody surface is shown in Fig. 5.34. The pressure is nondimensionalized by the stagnation point pressure for unimpinged blunt body flow. In order to properly visualize the effect of shock-shock interaction, the surface pressure for unimpinged blunt body flow (for the same freestream conditions) is also shown in the figure. The pressure on the windward side increases considerably with a localized zone of high pressure and falls below the surface pressure for unimpinged case on the leeward side. The peak value of pressure is about nine times the stagnation point value. The results compare very well with the experimental data of Wieting [34] and numerical calculations of Klopfer [44].

Figure 5.35 shows the heat transfer along the wall on the cowl forebody. The heating rates are nondimensionalized with respect to the stagnation point heating for unimpinged case. It shows similar behavior as the surface pressure, i.e., an increased heating on the windward side and decreased heating on the leeward side. A localized zone of intense heating is observed on the windward side. The results compare fairly well with the results of [44] but show poor comparison with the

Table 5.5 Freestream and stagnation point conditions for the cowl.

M_∞	Re_D	T_w/T_∞	D	δ	p_o/p_∞	$q_o(w/m^2)$
8.03	387500	2.382	0.0762	12.5	83.5	6.80 E + 5
5.94	186000	6.857	0.0254	15.0	45.8	2.16 E + 4

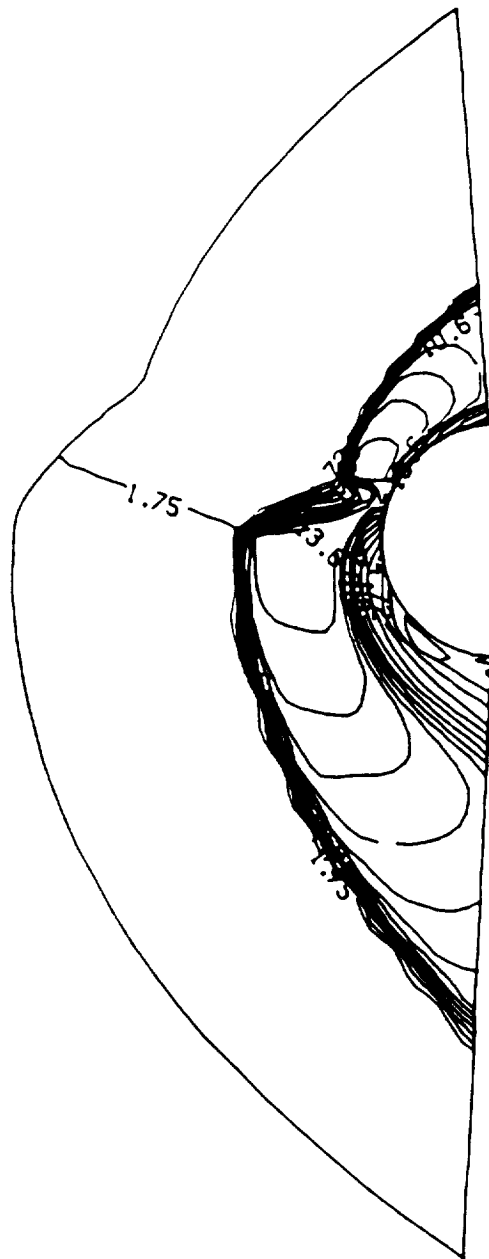


Fig. 5.30 Temperature contours for the cowl forebody, $M_\infty = 8.03$.

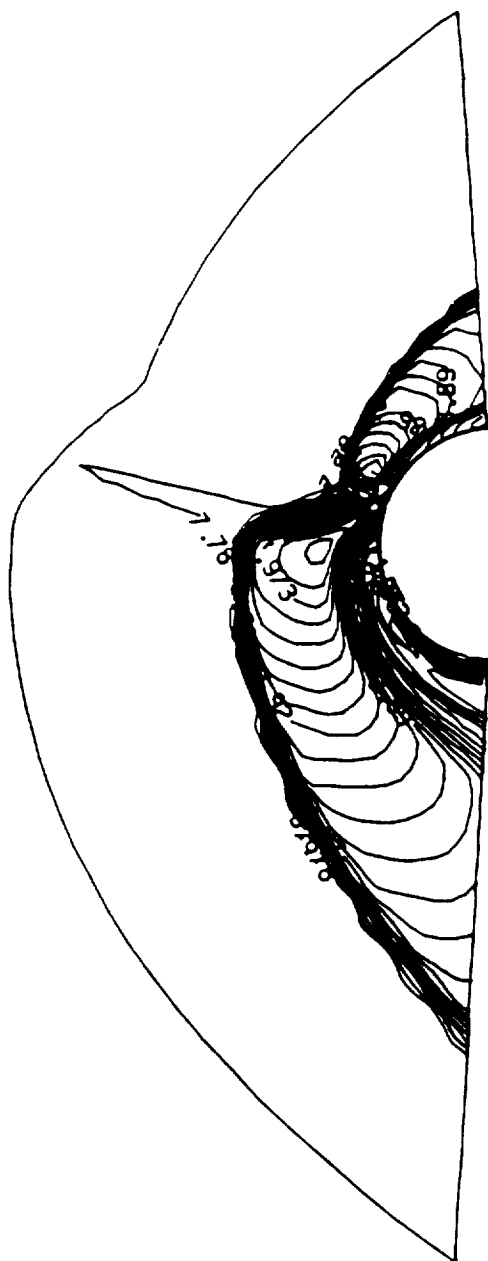


Fig. 5.31 Mach number contours for the cowl forebody, $M_\infty = 8.03$.

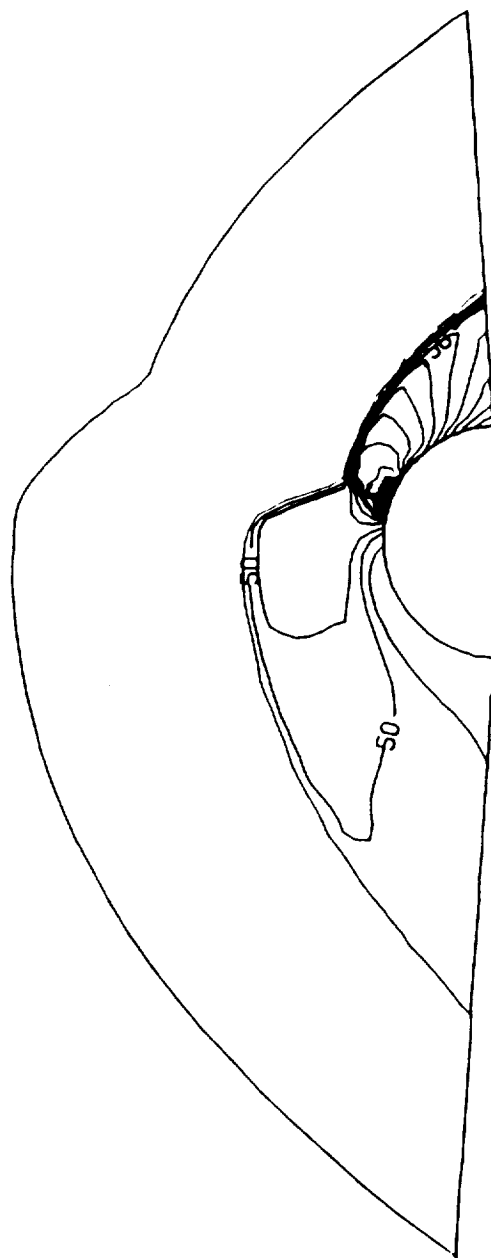


Fig. 5.32 Pressure number contours for the cowl forebody, $M_\infty = 8.03$.

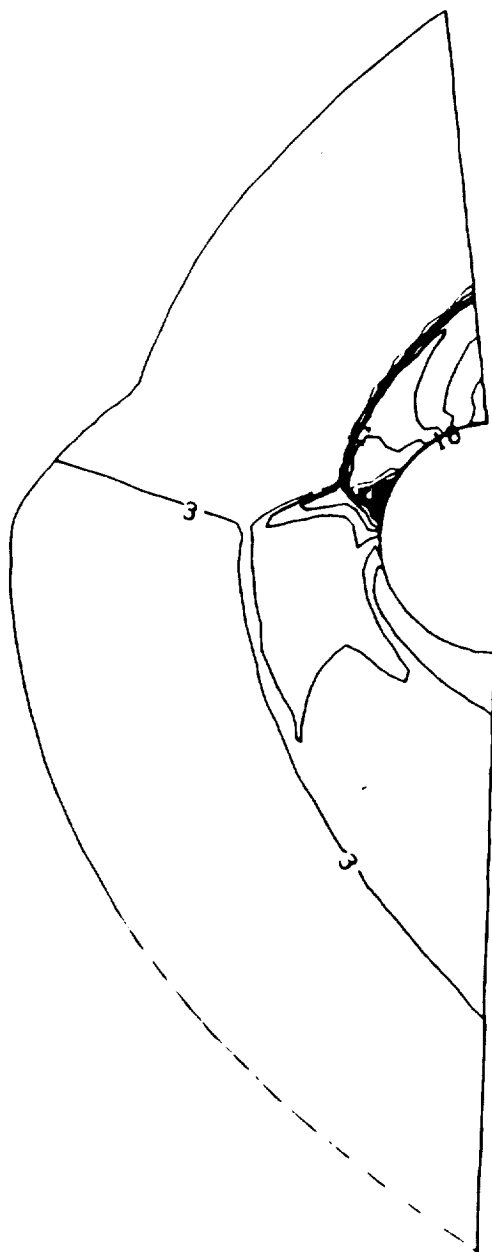


Fig. 5.33 Density contours for the cowl forebody, $M_\infty = 8.03$.

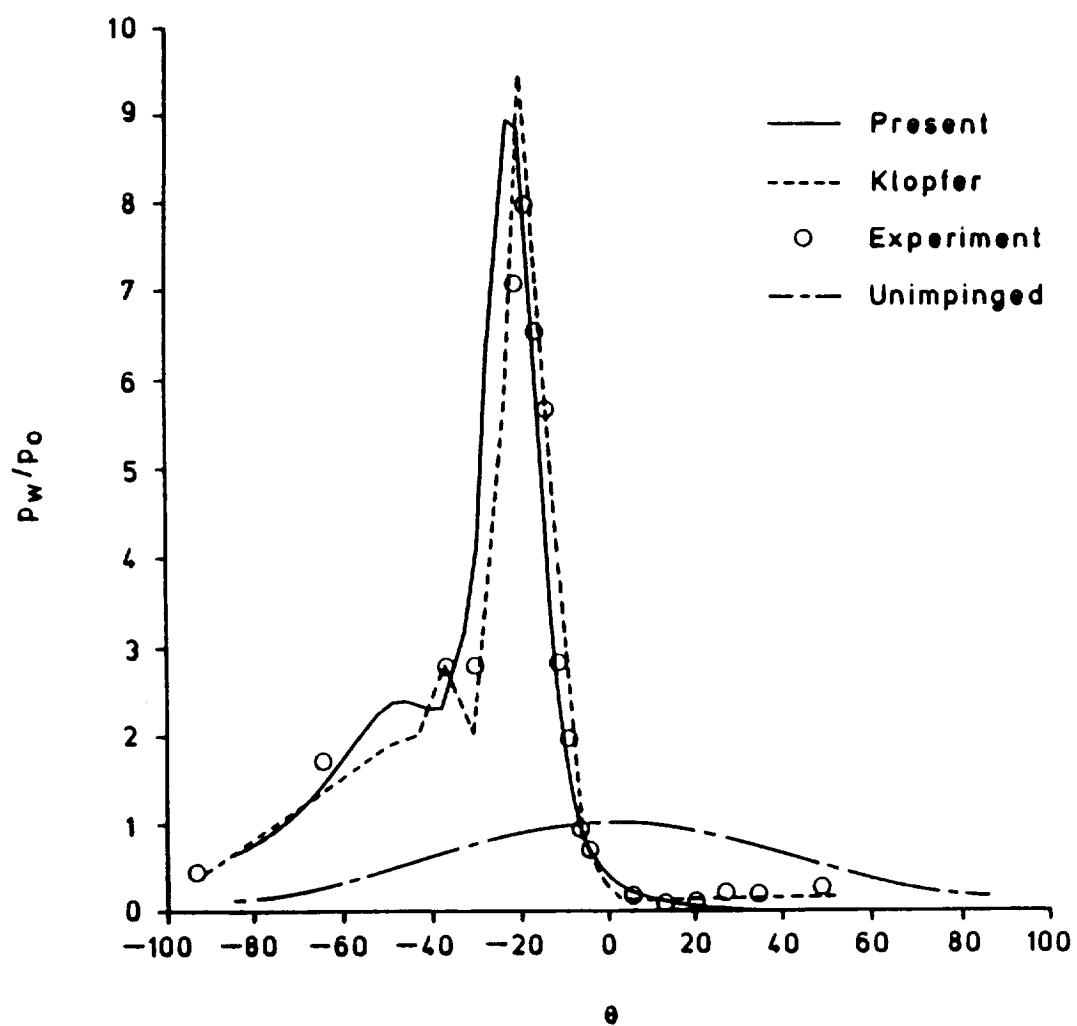


Fig. 5.34 Variation of surface pressure for the cowl forebody, $M_\infty = 8.03$.

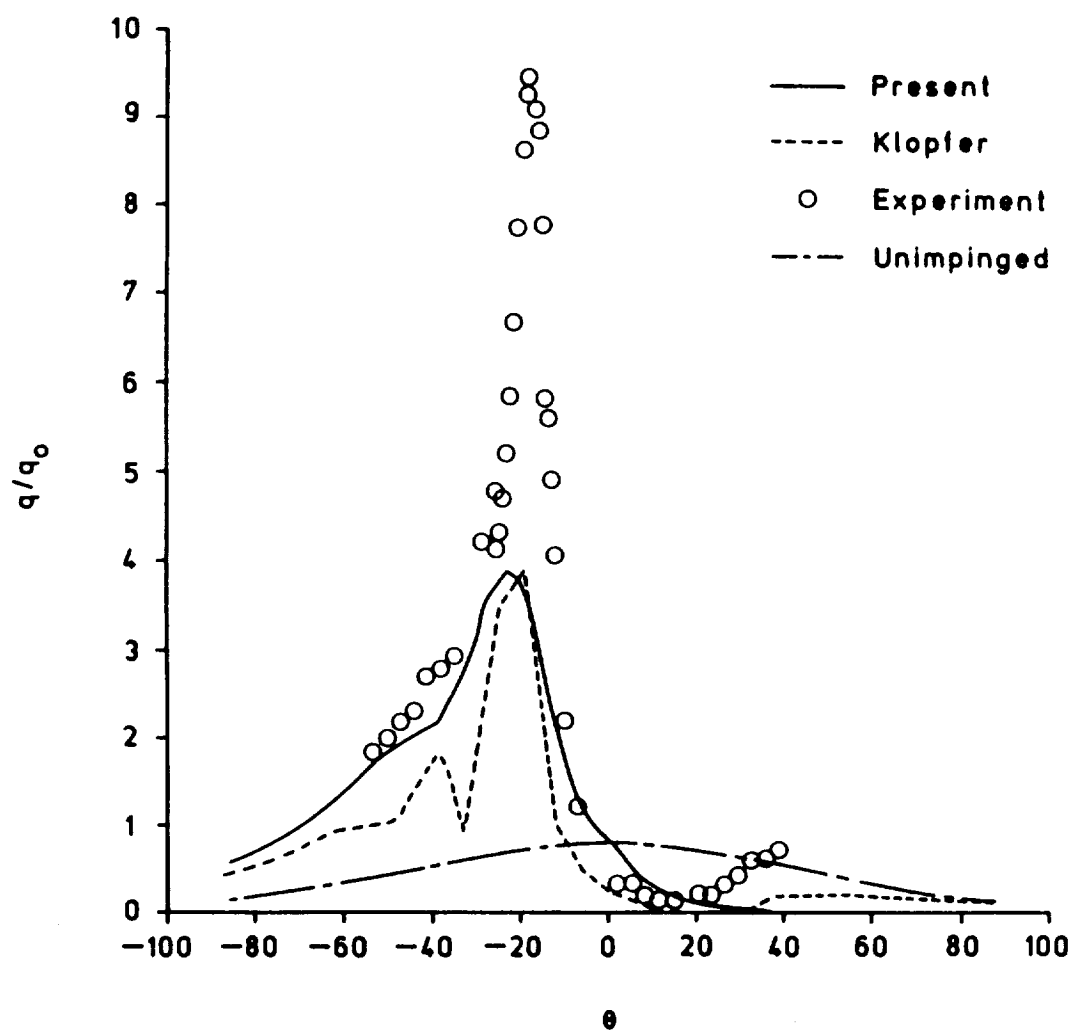


Fig. 5.35 Variation of surface heat transfer for the cowl forebody, $M_\infty = 8.03$.

experimental data. The trend is predicted but the magnitude is relatively lower, specially near the jet impingement location. It should be noted that for this case, the solution was found to be marginally unsteady as the residual did not go down more than three orders of magnitude. Also the jet oscillated slightly, thereby changing the location of the peak pressure and heating. Similar behavior was noted for the Type IV interaction in [44] and [45]. Due to poor comparison of heating rates and smearing of important flow features, it was decided to use adaptive grids thereby placing the grid points where they are needed the most. Body curvature, pressure and density were chosen as weight functions to adapt the grid to the solution. The body curvature clusters the grid points very close to the body while pressure and density attract the grid points near shocks and shear layers. Thirty percent of the points were allocated for adaptation by body curvature, forty percent by pressure and density and the rest of the points were used for creating uniformity of the grid so that the grid is not too coarse in any section. The adapted grid is shown in Fig. 4.10.

The temperature, Mach number, pressure and density contours are shown in Figs. 5.36 - 5.39, respectively for the adapted grid. Since the grid is fine near the shocks and shear layer, the flow features are now captured very well. The location of the stagnation point, jet and shear layer originating from the shock intersection can be seen clearly. The shear layer originating from the stagnation zone is much thicker on the leeward side as compared to the windward side.

Figure 5.40 shows the velocity vectors for the cowl forebody flow. Even though the flow is at zero angle of attack, its direction is changed as it passes through the impinging shock. The shear layer on the leeward side is seen clearly originating from the stagnation point.

The variations of pressure and heating rate along the cowl forebody surface are shown in Figs. 5.41 and 5.42, respectively. The general features of the pressure

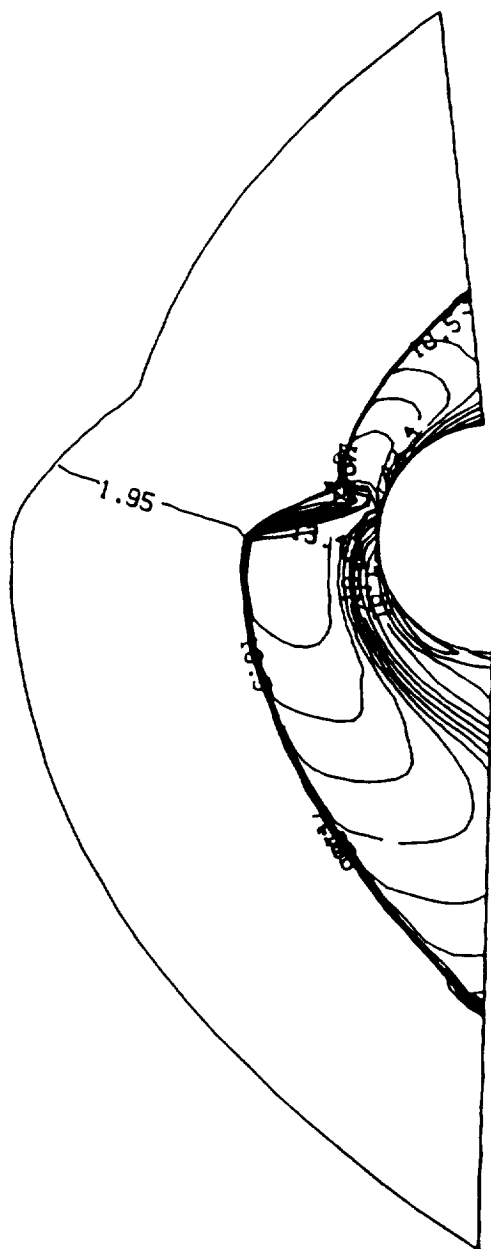


Fig. 5.36 Temperature contours for the cowl forebody for $M_\infty = 8.03$ with adapted grid.

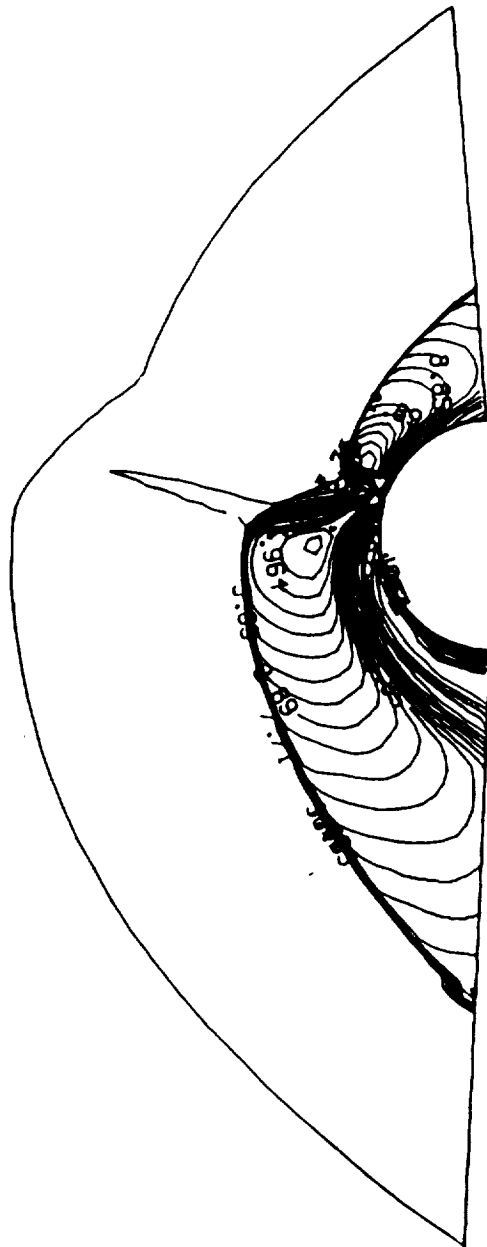


Fig. 5.37 Mach number contours for the cowl forebody, $M_\infty = 8.03$ with adapted grid

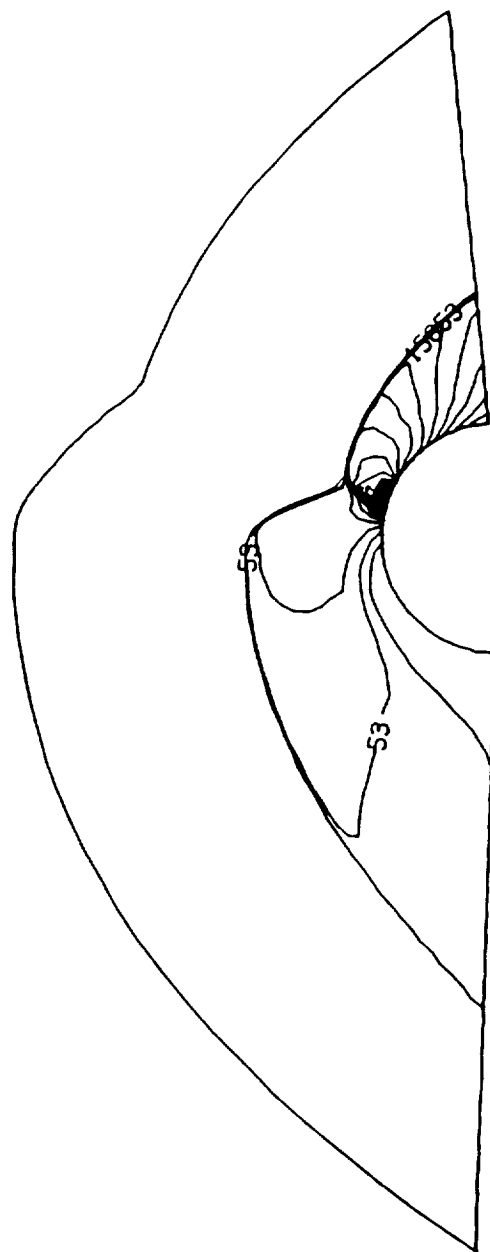


Fig. 5.38 Pressure contours for the cowl forebody for $M_\infty = 8.03$ with adapted grid.

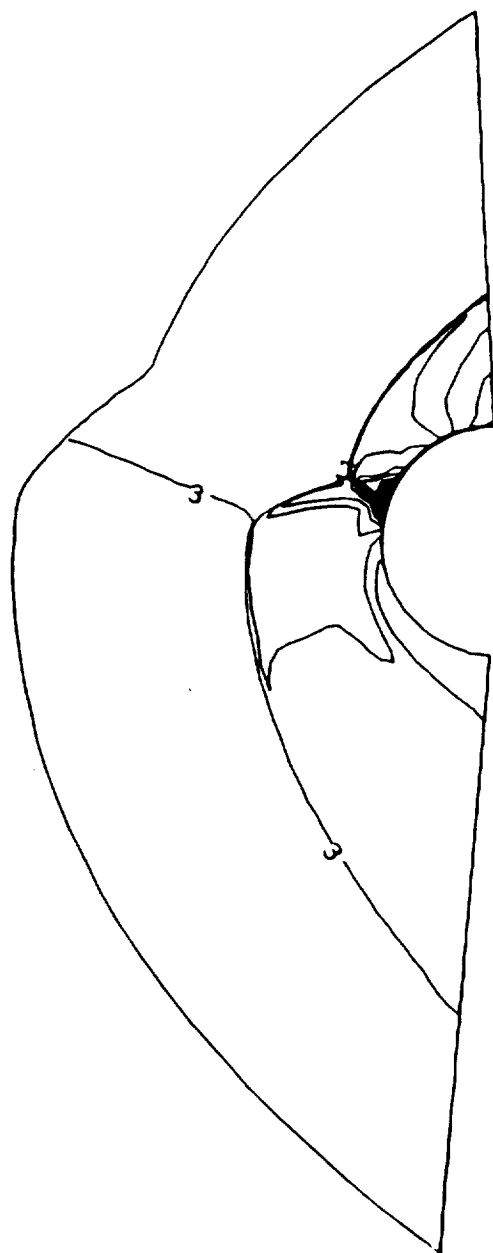


Fig. 5.39 Density contours for the cowl forebody, $M_\infty = 8.03$ with adapted grid

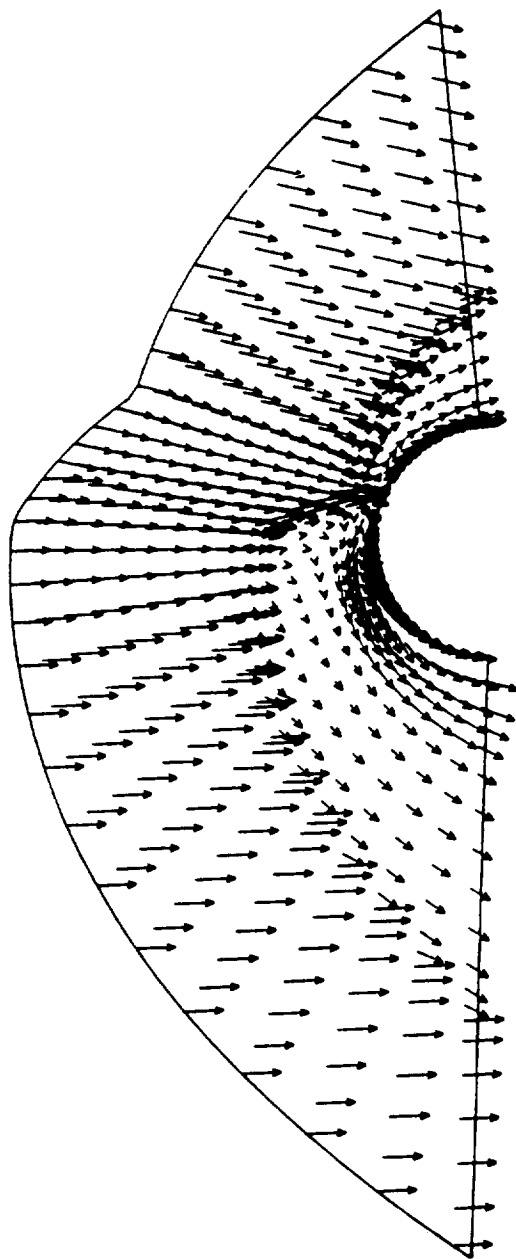


Fig. 5.40 Velocity vectors for the cowl forebody, $M_\infty = 8.03$ with adapted grid.

distribution are unchanged, except for the peak pressure which is now the same as obtained in [44]. It should be noted that for this case the location of the impinging shock was made to coincide with the experimental location by matching the peak pressure location. The heating rates show a remarkable improvement over the previous calculations. The results compare favorably with the experiment. The discrepancy in the peak values is probably due to the unsteadiness in the flow and/or the turbulent nature of the jet as indicated recently by Moon et al. [46]. The rate of convergence for this case was found to be slower than that for the unadapted grid case. The cowl of the scramjet engine is modeled by a 5° wedge. The cowl afterbody flow is computed by solving the parabolized Navier-Stokes equations using the van Leer scheme described previously. The initial plane solution, to initiate the marching procedure, is provided by the cowl forebody solution. The objective of carrying out the cowl afterbody calculation is to determine how the flow entering the engine inlet is affected by the shock-shock interactions.

Figures 5.43 and 5.44 show the temperature contours on the cowl afterbody for the windward and the leeward sides, respectively. The flow field on the windward side is quite different as compared to the leeward side. The flow on the windward side shows typical two-dimensional wedge flow features, such as rays of the constant Mach number and the shock attaining conical angle slightly downstream of the nose. The leeward side shows thick shear layer interacting with the boundary layer; this interaction again produces a weak shear layer whose strength diminishes rapidly with the axial distance. Similar behavior can also be seen in the Mach contours for the cowl afterbody in Figs. 5.45 and 5.46.

Figure 5.47 shows the variation of shock standoff distance along the cowl afterbody on leeward and windward sides for the impinged case. These are compared with the results for the unimpinged case. The shock moves closer to the body on the windward side and away from it on the leeward side as compared to

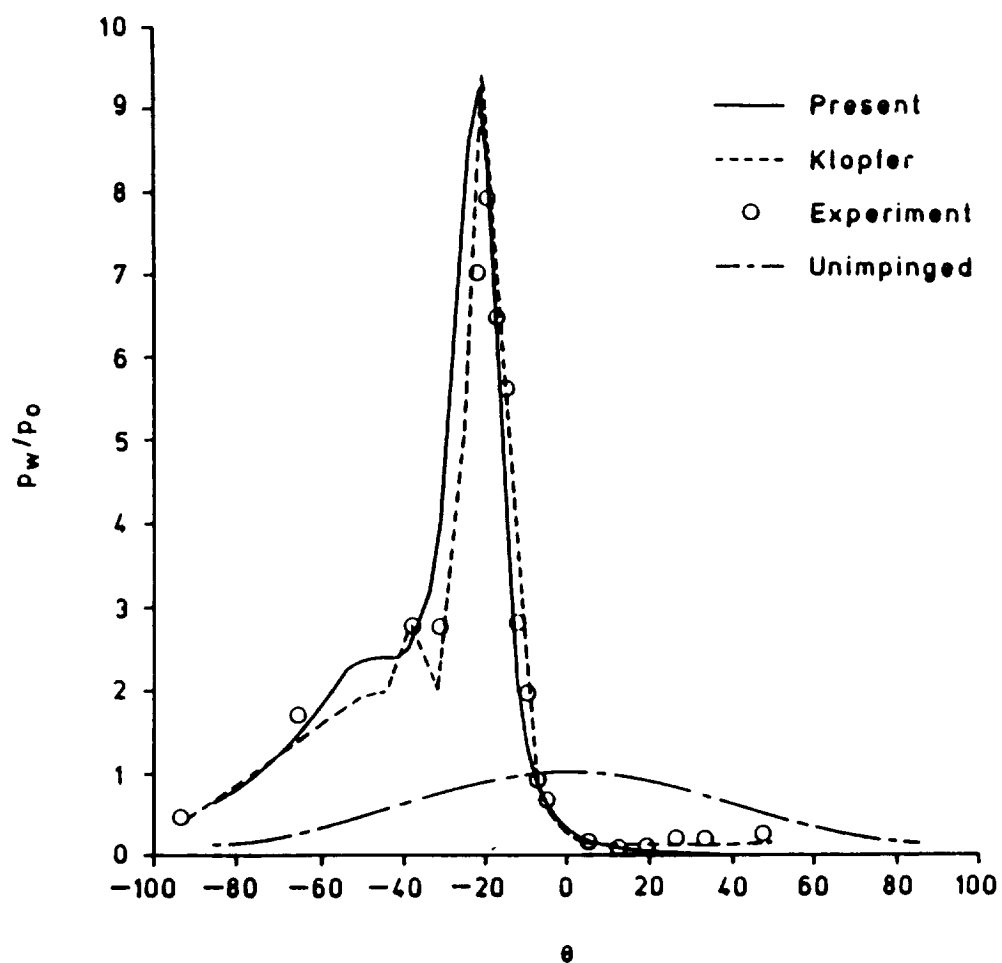


Fig. 5.41 Variation of surface pressure for the cowl forebody, $M_\infty = 8.03$ with adapted grid.

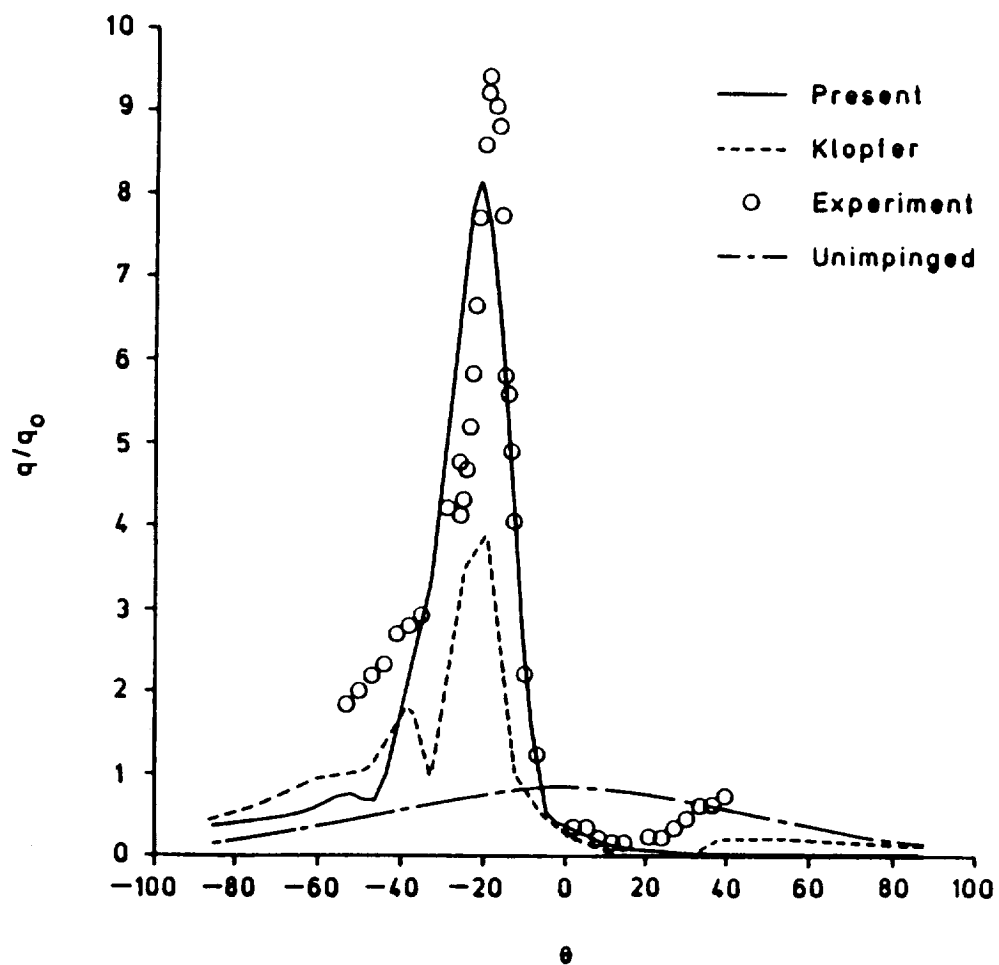


Fig. 5.42 Variation of surface heat transfer for the cowl forebody, $M_\infty = 8.03$ with adapted grid.

the unimpinged case. The calculations were carried out up to 40 nose radii downstream. The angle at which the shock enters the inlet is significantly changed due to the shock-shock interaction which can affect the inlet performance.

The variation of pressure on the cowl afterbody is shown in Fig. 5.48. The pressure on the windward side increases on the forward portion of the cowl afterbody; it reaches a peak value and then settles down to a constant value as the flow recompresses back after the expansion on the cowl forebody. On the leeward side also, the pressure increases and then gradually attains approximately the same value as for the unimpinged case. The rate of pressure increase on the forward portion of the leeward side is found to be slower than on the windward side.

Similar calculations were carried out for Mach 5.94 freestream conditions and the results are shown in Figs. 5.49 - 5.58. Qualitatively these results are very similar to the Mach 8.03 conditions. The grid for this case is generated in the same way as for the previous case. The temperature, Mach number, pressure and density contours are shown in Figs. 5.49 - 5.52 for the cowl forebody. As noted previously the shock moves toward the body on windward side and away from it on leeward side. The effects of jet are clearly visible in the figure. The variations of surface pressure and heat transfer are shown in Figs. 5.53 and 5.54, respectively. The numerical results are compared with the experimental data reported by Tannehill et al. [42] from an unpublished experiment by J. W. Keyes of NASA Langley. The computed values of surface pressure agree very well with the experimental data although the peak pressure is slightly lower than the experimental peak. Although not shown here, the peak value of the pressure matches with the numerical calculations of Tannehill et al. [42]. The variation of heat transfer on the cowl forebody is shown in Fig. 5.54. For heating rates, the experimental data was reported only at one point. The peak value of the heating rate is 6.4 times the stagnation point value, which is within the uncertainty range of the experiment.

The results for the cowl afterbody are shown in Figs. 5.55 - 5.58. The Mach number contours for the windward and the leeward sides on the afterbody are shown in 5.55 and 5.56. The shear layer on the leeward side is thinner as compared to the Mach 8.03 due to weaker strength of the interacting shocks. The variation of shock standoff distance for the cowl afterbody is shown in Fig. 5.57 and the variation of the wall pressure for the cowl afterbody is shown in Fig. 5.58. The results show the same trends as for the previous case.

ORIGINAL PAGE IS
OF POOR QUALITY

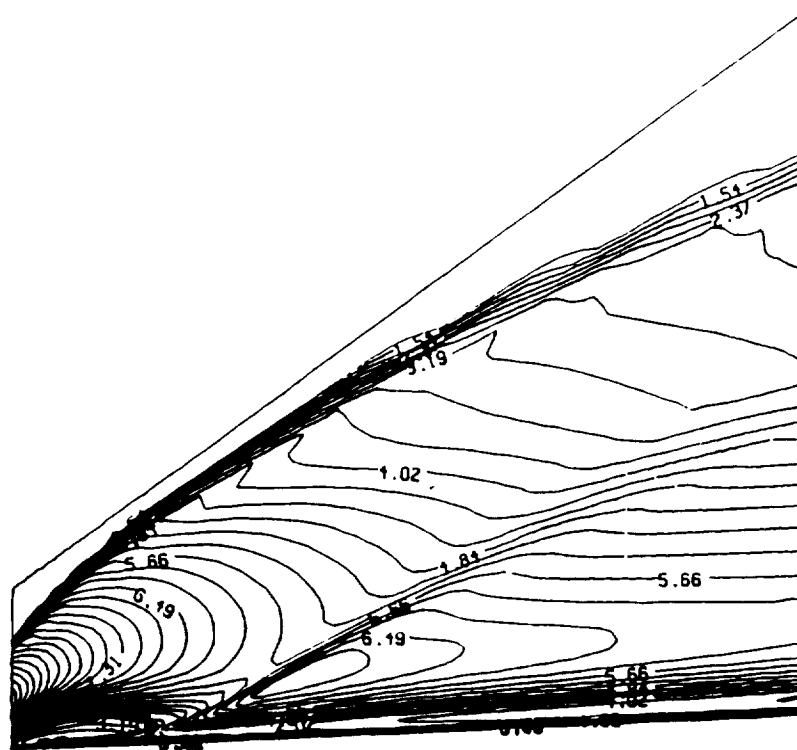


Fig. 5.44 Temperature contours on the leeward side of the cowl afterbody, $M_\infty = 8.03$.

ORIGINAL PAGE IS
OF POOR QUALITY

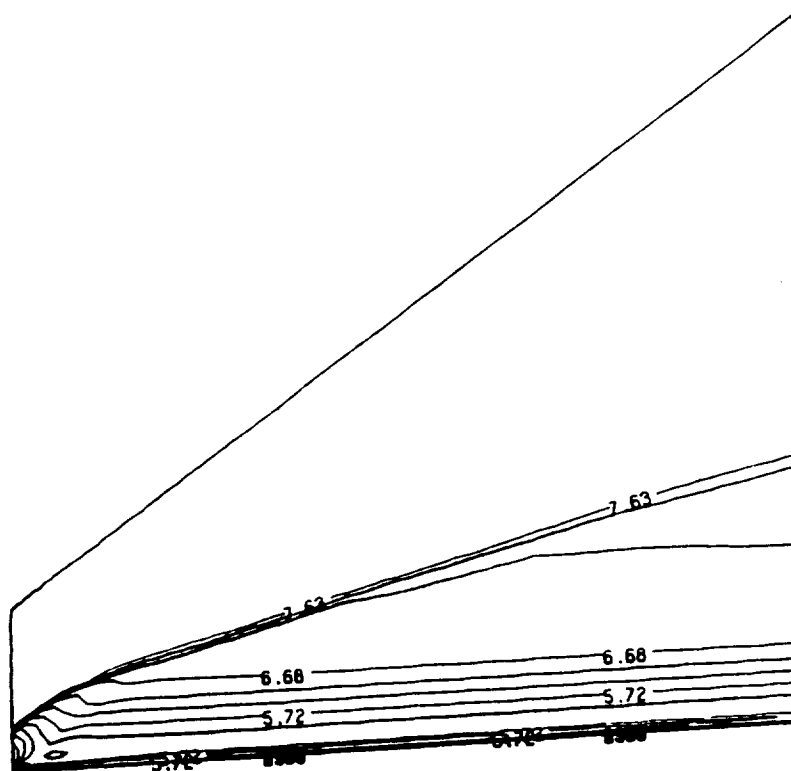


Fig. 5.45 Mach number contours on the windward side of the cowl afterbody,
 $M_{\infty} = 8.03$.

ORIGINAL PAGE IS
OF POOR QUALITY

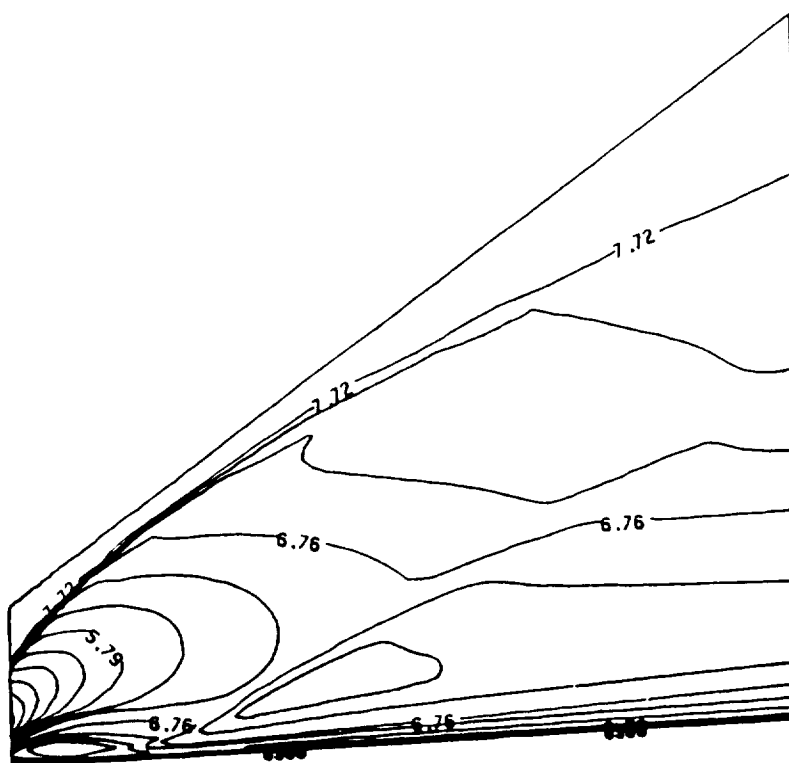


Fig. 5.46 Mach number contours on the leeward side of the cowl afterbody, $M_\infty = 8.03$.

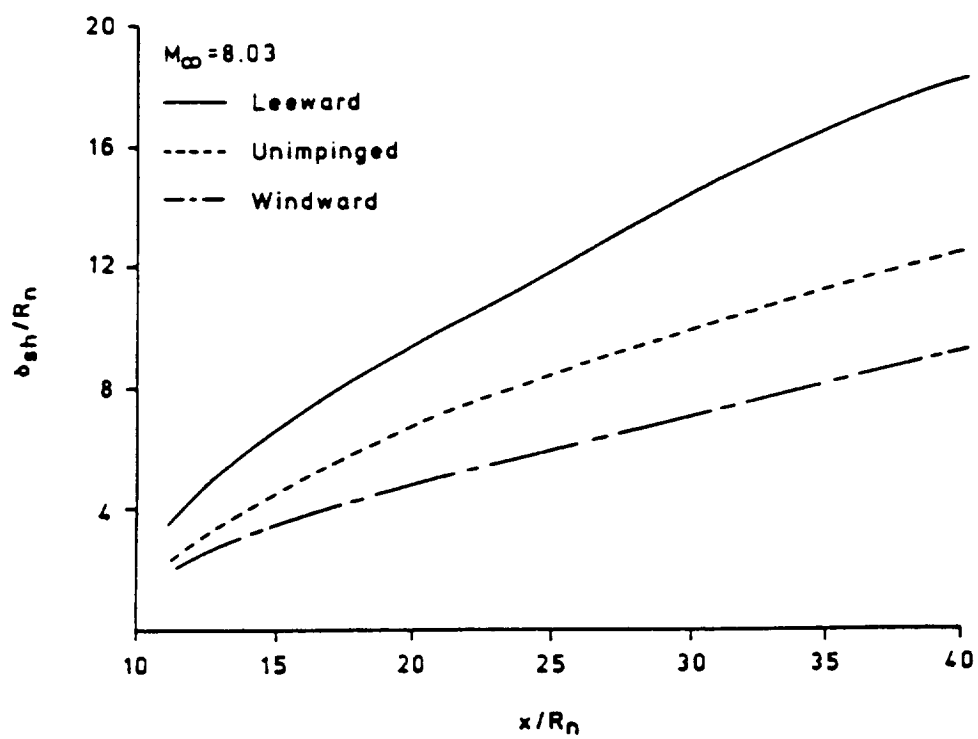


Fig. 5.47 Variation of shock standoff distance with axial distance for the cowl afterbody, $M_\infty = 8.03$

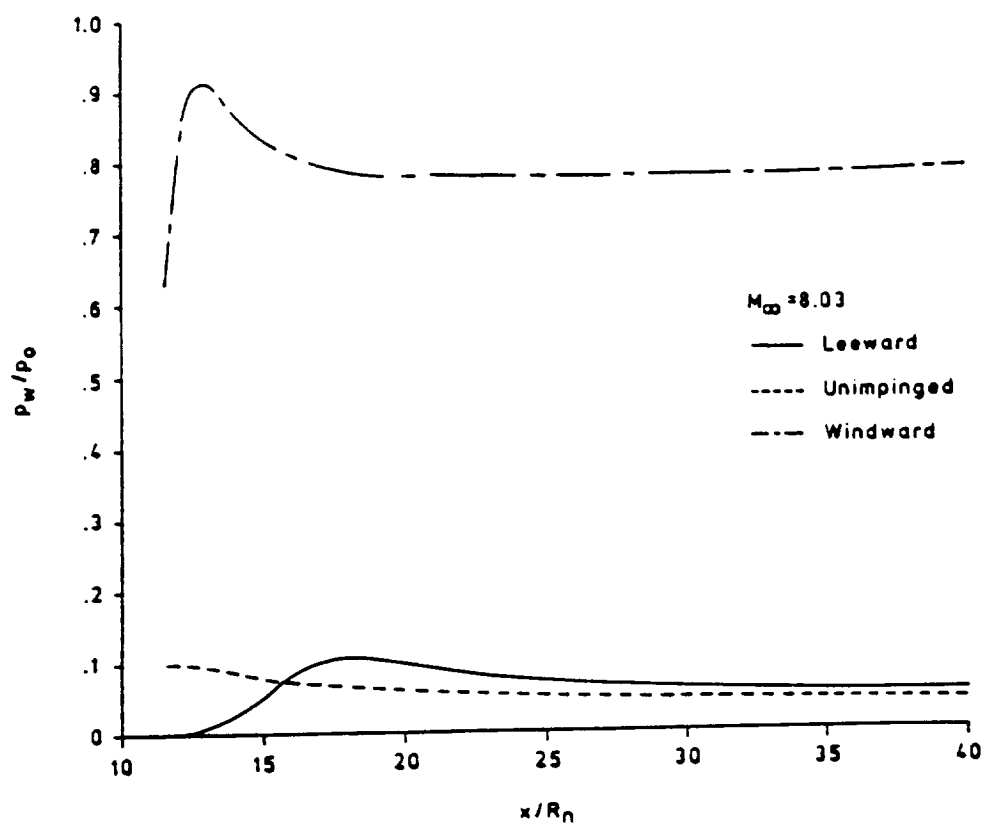


Fig. 5.48 Variation of surface pressure with axial distance for the cowl afterbody, $M_\infty = 8.03$

ORIGINAL PAGE IS
OF POOR QUALITY

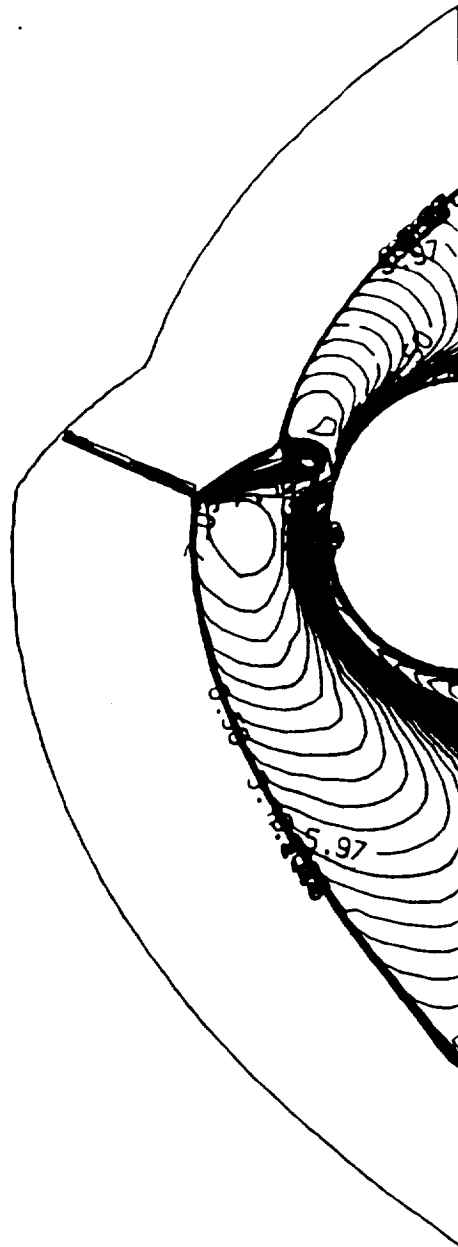


Fig. 5.49 Temperature for the cowl forebody, $M_\infty = 5.94$.

ORIGINAL PAGE IS
OF POOR QUALITY

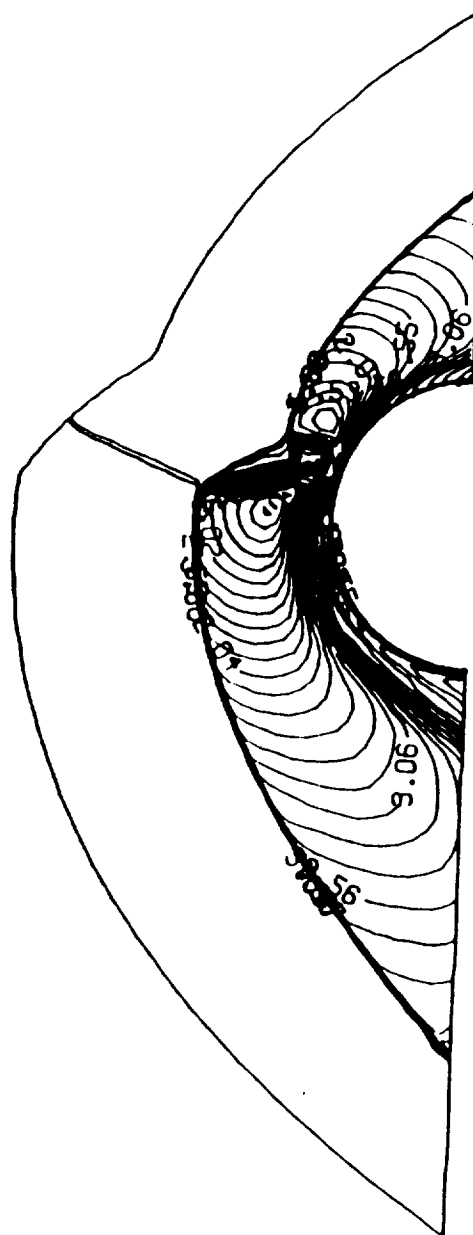


Fig. 5.50 Mach contours for the cowl forebody, $M_\infty = 5.94$.

ORIGINAL PAGE IS
OF POOR QUALITY

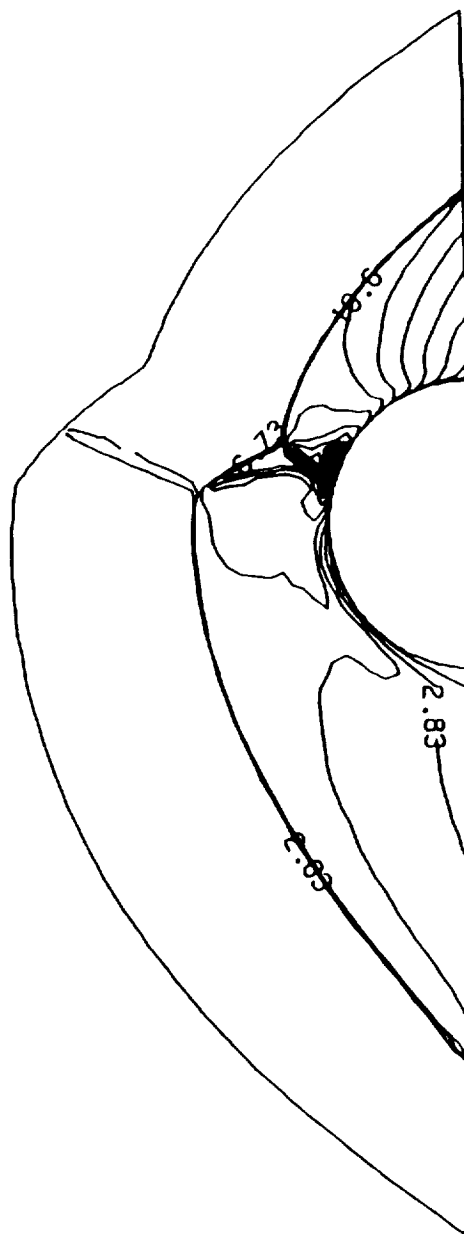


Fig. 5.52 Density contours for the cowl forebody, $M_\infty = 5.94$.

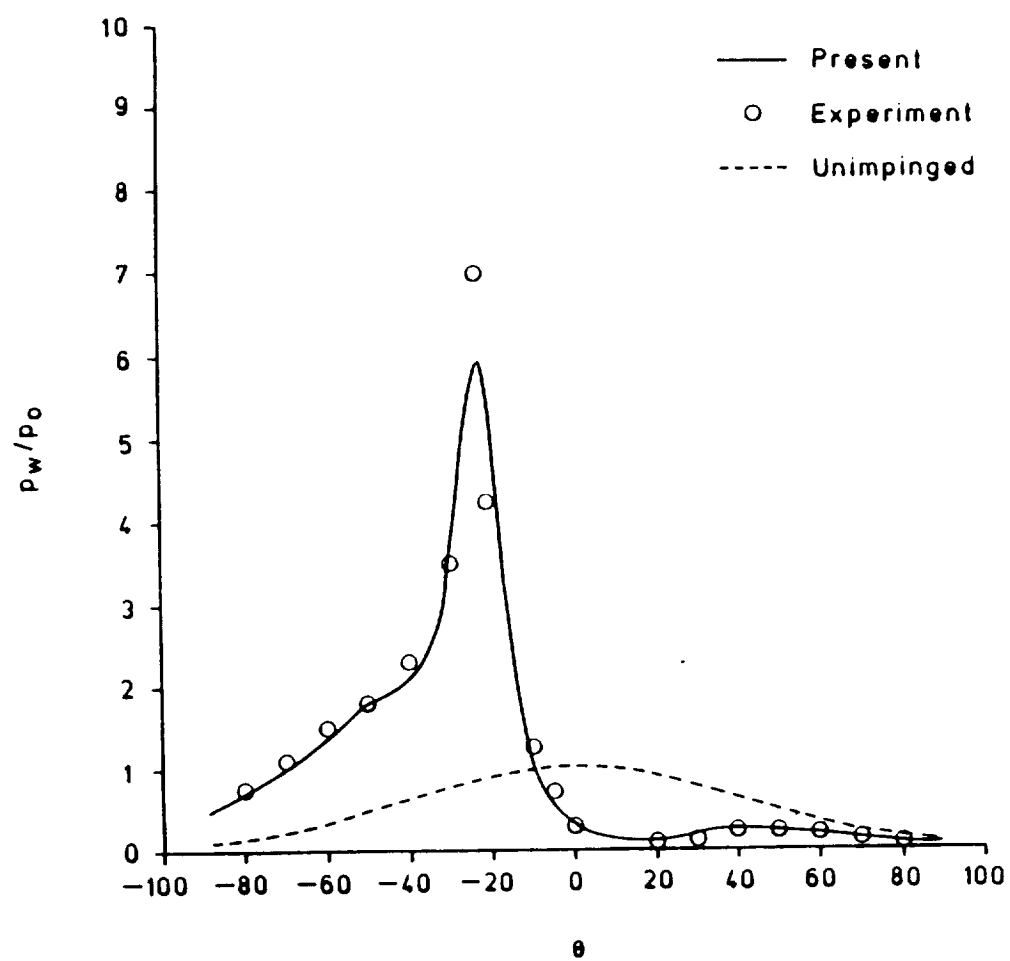


Fig. 5.53 Variation of surface pressure for the cowl forebody, $M_\infty = 5.94$

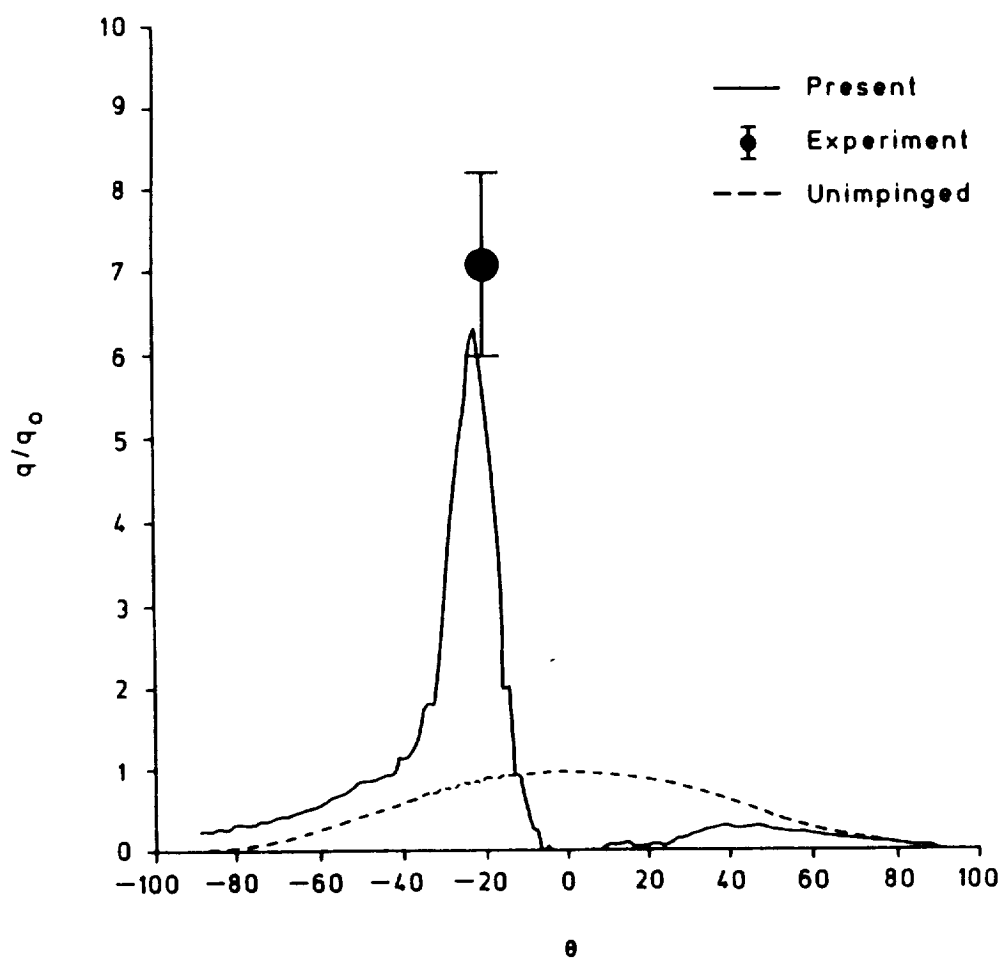


Fig. 5.54 Variation of surface heat transfer for the cowl forebody, $M_\infty = 5.94$.

ORIGINAL PAGE IS
OF POOR QUALITY

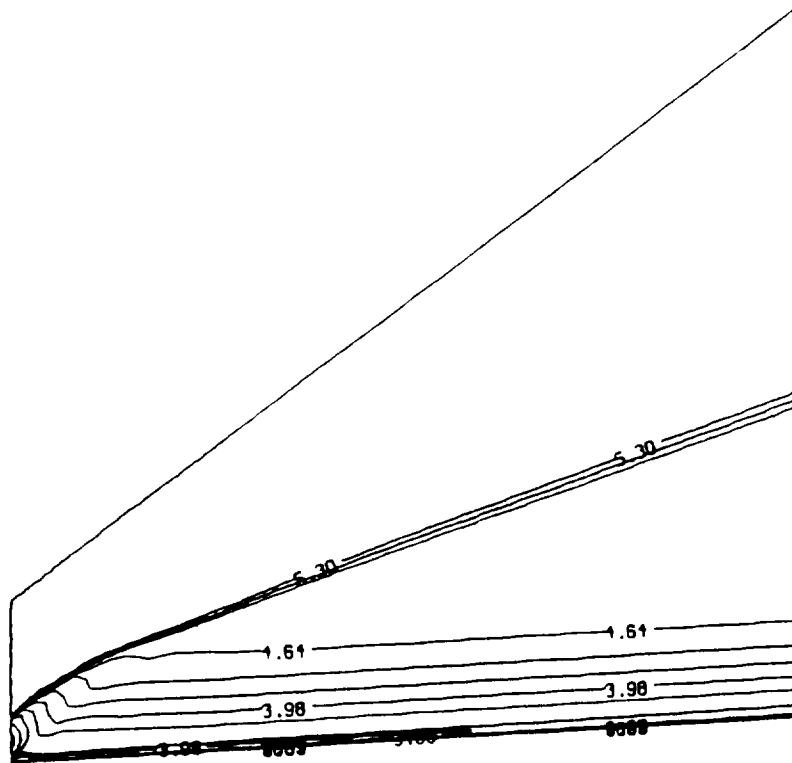


Fig. 5.55 Mach number contours on the windward side of the cowl afterbody,
 $M_{\infty} = 5.94$.

ORIGINAL PAGE IS
OF POOR QUALITY

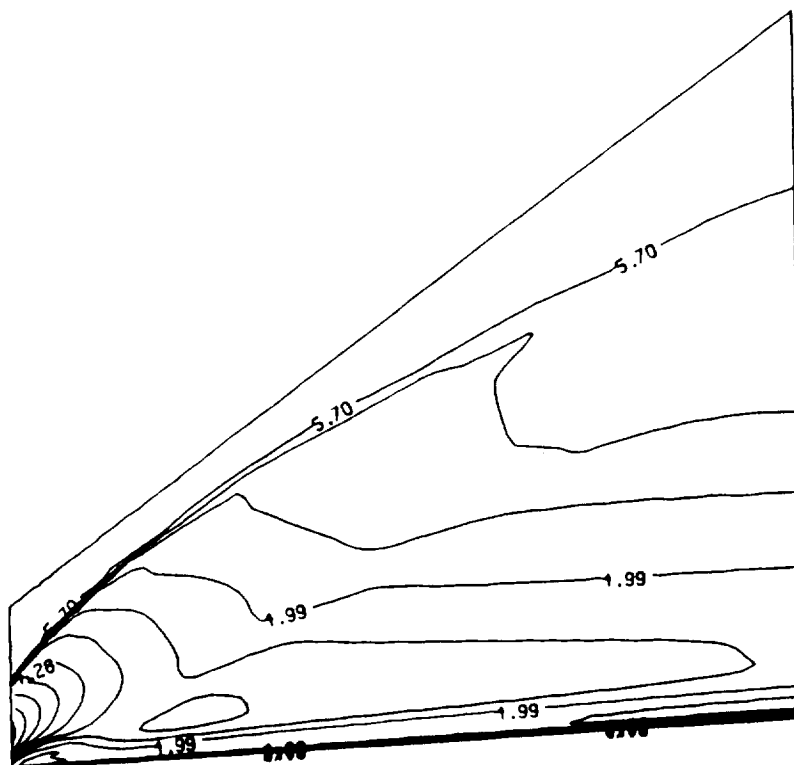


Fig. 5.56 Mach number contours on the leeward side of the cowl afterbody, $M_\infty = 5.94$.

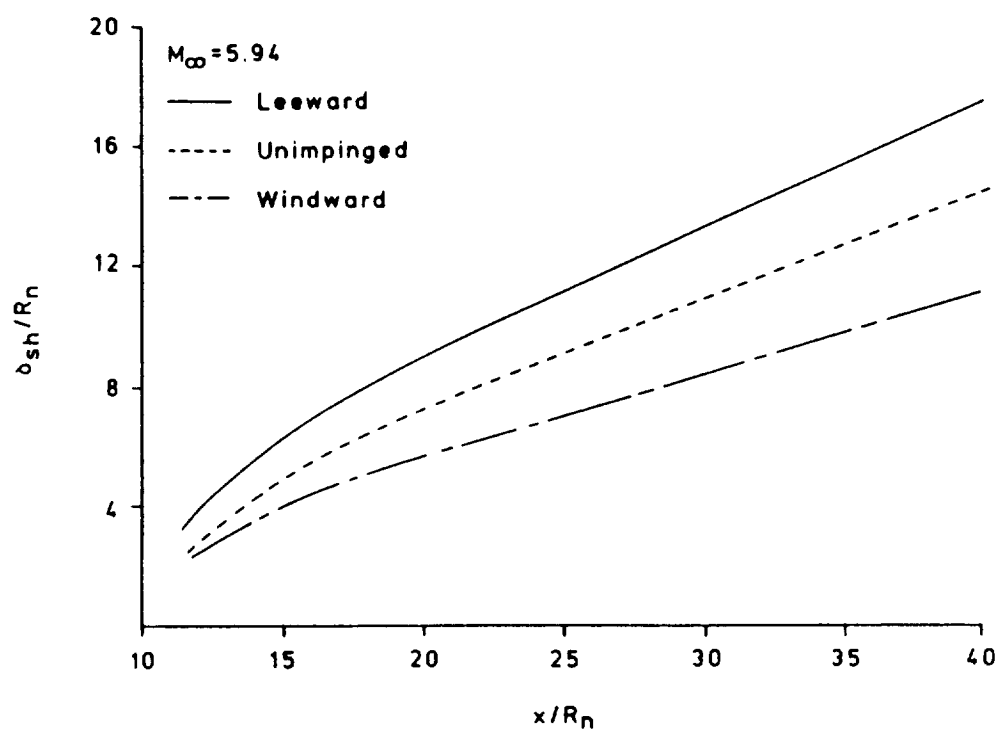


Fig. 5.57 Variation of shock standoff distance with axial distance for the cowl afterbody, $M_\infty = 5.94$

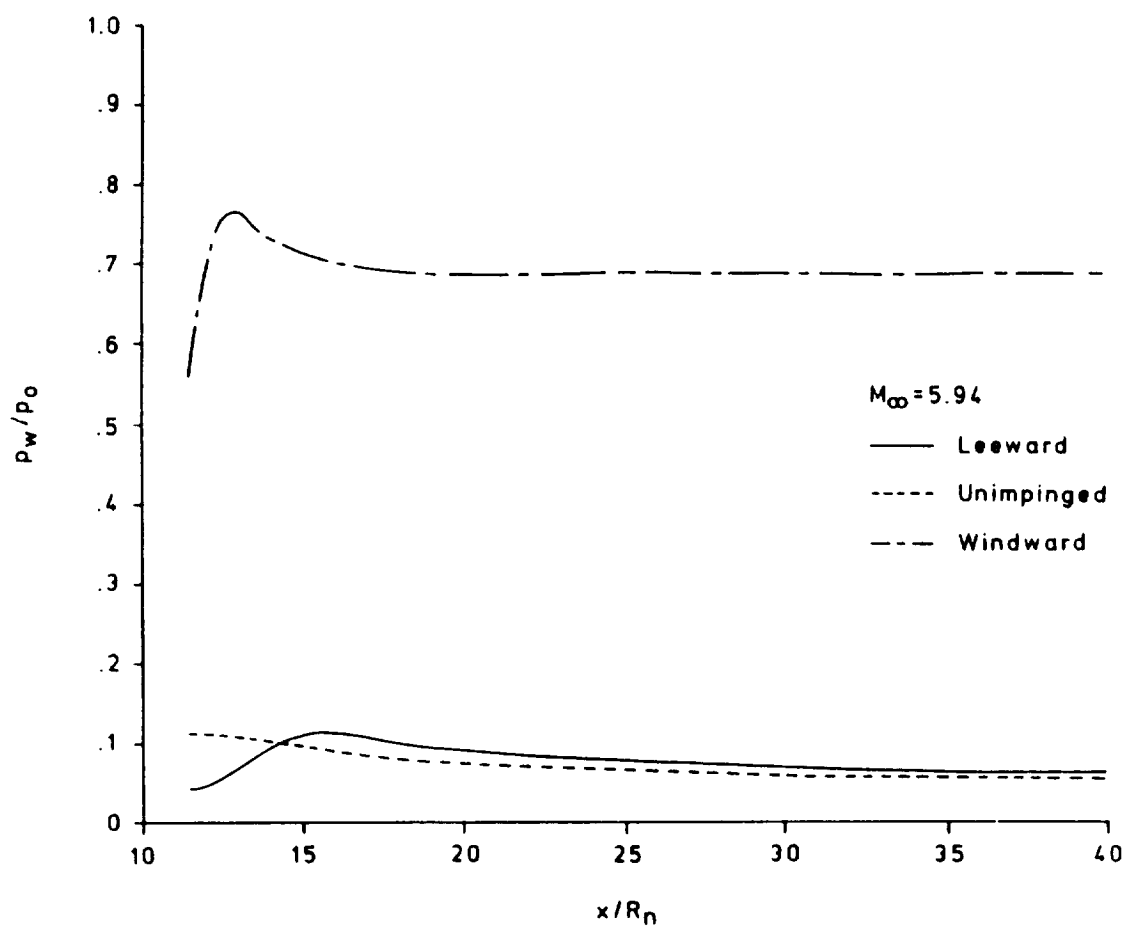


Fig. 5.58 Variation of surface pressure with axial distance for the cowl afterbody, $M_\infty = 5.94$

5.3 Forebody Shock and the Inlet Sidewall Shock Interaction

In this section the interaction of the forebody shock with the inlet sidewall shock is discussed. As noted previously, the flow is fully three-dimensional in nature for this case due to the orientation of the impinging forebody shock as well as the sweep of the inlet. Due to sweep of the inlet sidewall, the Type V interaction occurs and is considered in this section. Results have been obtained for a 25° swept sidewall and 10° impinging shock generator angle. The freestream conditions used for the present calculations are given in Table 5.6. For three-dimensional calculations also, the flow field is initialized by the undisturbed flow field solution. First the results are presented for the undisturbed flow and then with the impinging shock to show the effect of impingement.

Figure 5.59 shows the pressure contours for the unimpinged case. The stagnation plane ($\theta = 0$) contours are shown in Fig. 5.59(a). The bow shock can be seen clearly and is swept back as it follows the body contours. The flow in each cross-sectional plane is identical, so only one such plane is shown in Fig. 5.59(b). The figure shows a typical blunt body solution. At the stagnation point, the pressure has its peak value and the shock standoff distance is minimum. Figure 5.60 shows the temperature, Mach number and the pressure contours in the stagnation plane with shock impingement. The temperature contours are shown in Fig. 5.60(a). Due to stretching, the grid away from the surface is coarse; consequently, the shock and the other flow features are smeared over several grid points. The impinging shock is clearly visible in the figure. The bow shock moves away from its unimpinged position and a shear layer is produced. The shear layer interacts with the boundary layer. Also, a transmitted shock is produced which strikes the body causing a jump in pressure and heating rates. These are typical features of the Type V interaction. There are temperature and density gradients across the shear layer. The Mach

Table 5.6 Freestream conditions for inlet.

M_∞	Re_D	T_w	T_∞	R_n	δ
5.94	180000	394 k	59.6 k	0.0125 m	10.0

ORIGINAL PAGE IS
OF POOR QUALITY

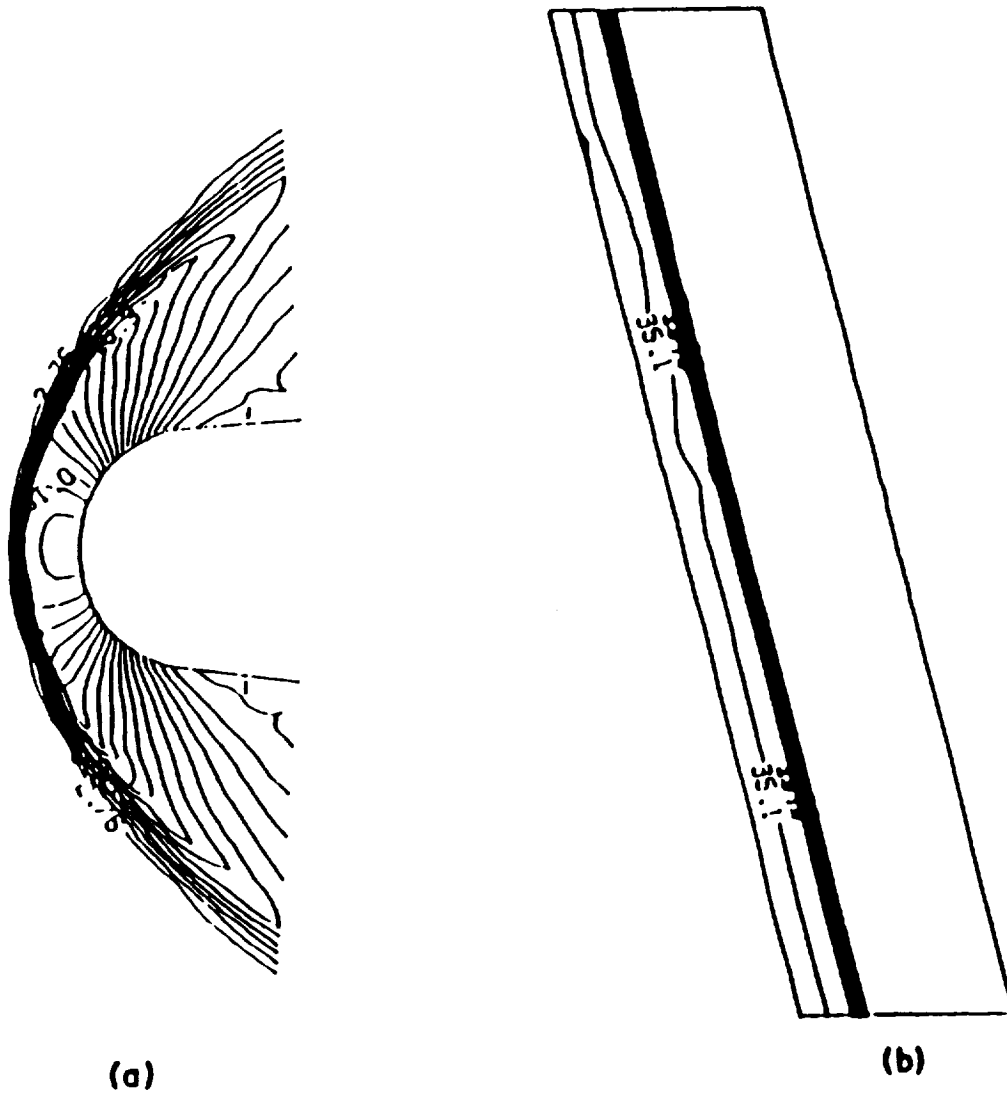


Fig. 5.59 Pressure contours for the unimpinged case in stagnation ($\theta = 0$) and $z =$ constant plane.

number contours are shown in Fig. 5.60(b); the flow is fully subsonic behind the bow shock and the shear layer can be seen. Figure 5.60(c) shows the pressure contours in the stagnation plane. Since the pressure is constant across the shear layer, it is not visible in this figure. Some expansion waves can be seen emanating from the intersection point. These expansion waves reduce the surface pressure as the flow expands.

More insight into the numerical solution can be gained by examining the plots for $z = \text{constant}$ planes. Figure 5.61 shows a series of contour plots for increasing values of z . The movement of the impingement point (as it moves away from stagnation point) can be seen clearly; also, the shear layer as it develops is very well captured.

Figure 5.62 shows a cylindrical fin coated with temperature sensitive paint and the corresponding schlieren photograph locating regions of high pressure and heat transfer for Type V interference at Mach 4.6 and is taken from [31]. It should be noted that the freestream conditions for this case are slightly different but it shows a typical Type V interaction. The numerical solutions are shown in Figs. 5.63 and 5.64. The surface pressure contours are shown in Fig. 5.63 and the stagnation plane pressure contours in Fig. 5.64. The numerical solution captures the first two (A and B) peaks in pressure and heat transfer. The third peak (C) is caused due to separation near the nose which is absent in the numerical solution due to assumption of infinite length of the body. The behavior of bow shock near the impingement point is very well captured by the numerical scheme. The comparison of Figs. 5.63(b) and 5.64 shows how well the physical phenomenon is captured by the numerical scheme.

Figures 5.65 - 5.70 show the variation of pressure and heat transfer along the surface. They are nondimensionalized with respect to the unimpinged stagnation line values. The unimpinged stagnation line pressure is obtained by the

ORIGINAL PAGE IS
OF POOR QUALITY

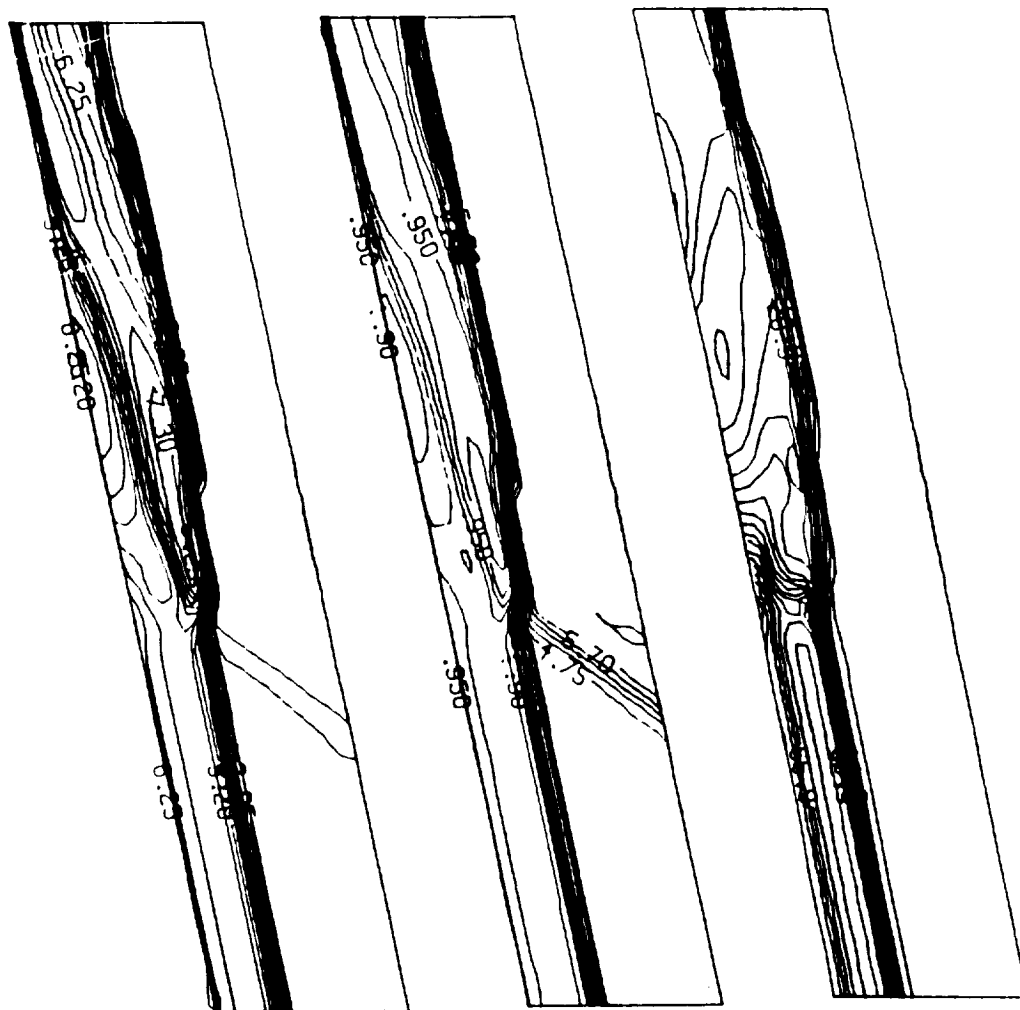


Fig. 5.60 Temperature, Mach number and the Pressure contours in the stagnation plane($\theta = 0$).

ORIGINAL PAGE IS
OF POOR QUALITY

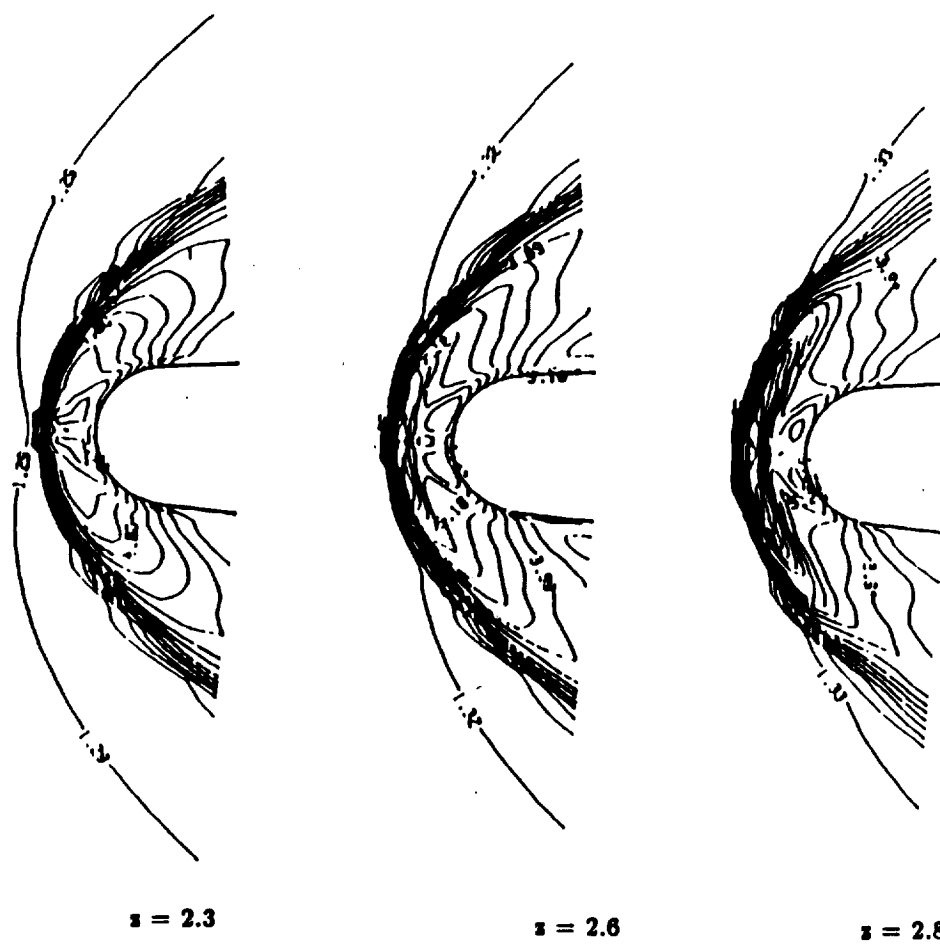


Fig. 5.61 Temperature contours in the $z = 2.3, 2.6$, and 2.8 cm plane.

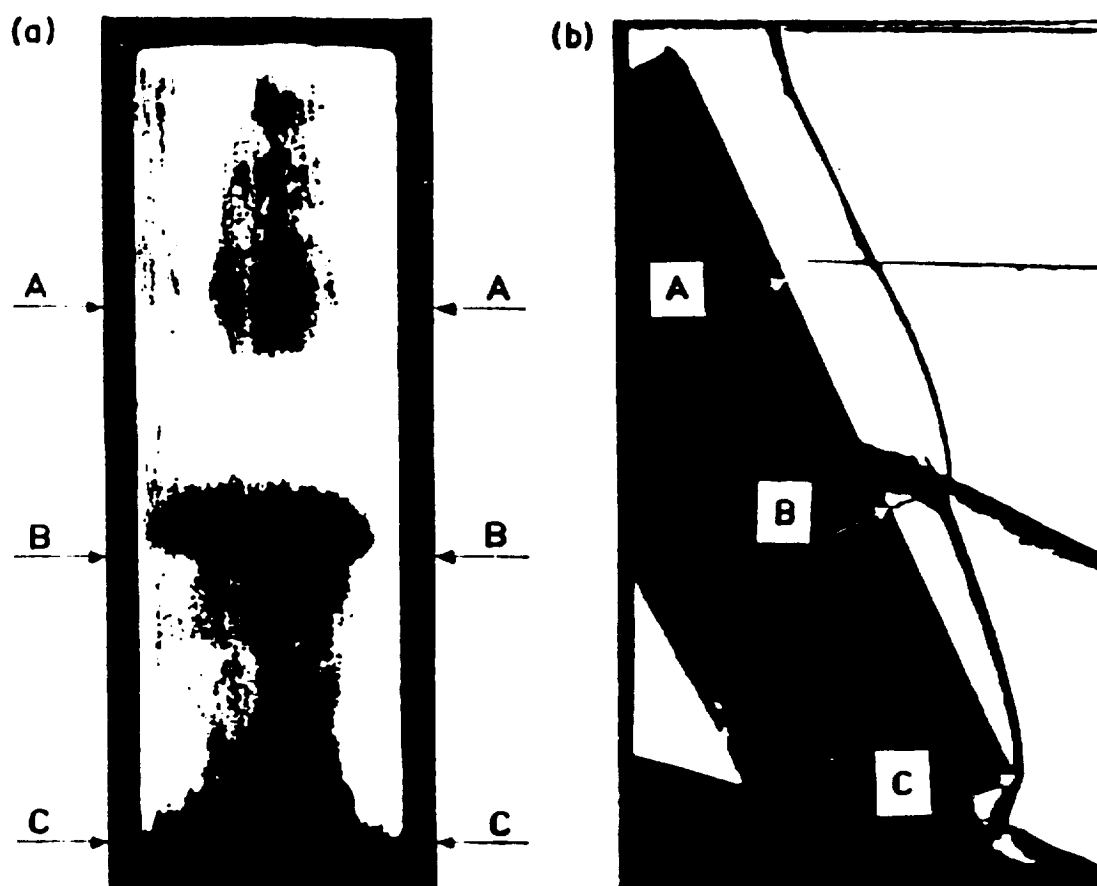


Fig. 5.62 Local regions of high heating rates and corresponding schlieren photograph.

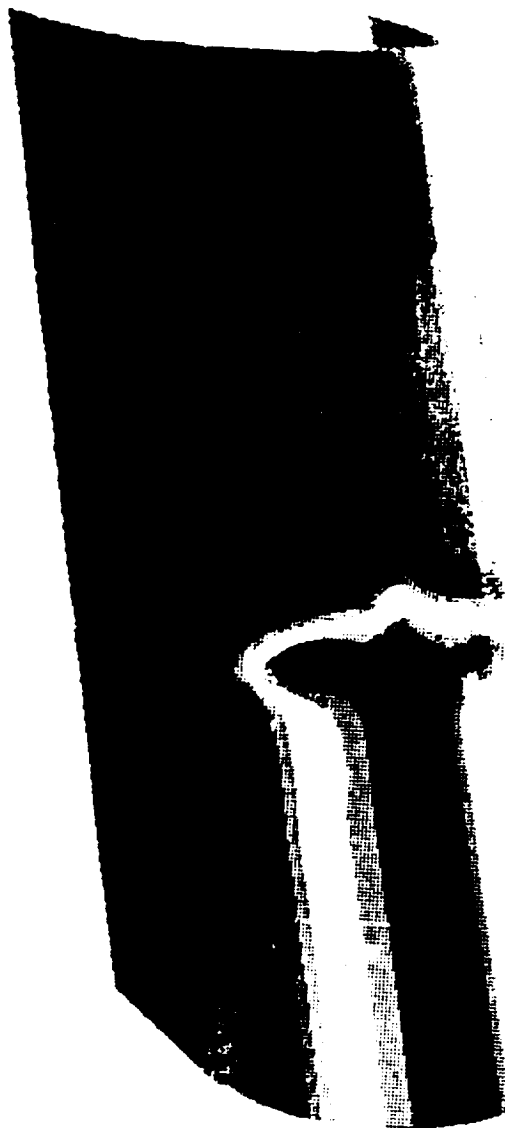


Fig. 5.63 Surface pressure contours for Type V interaction.

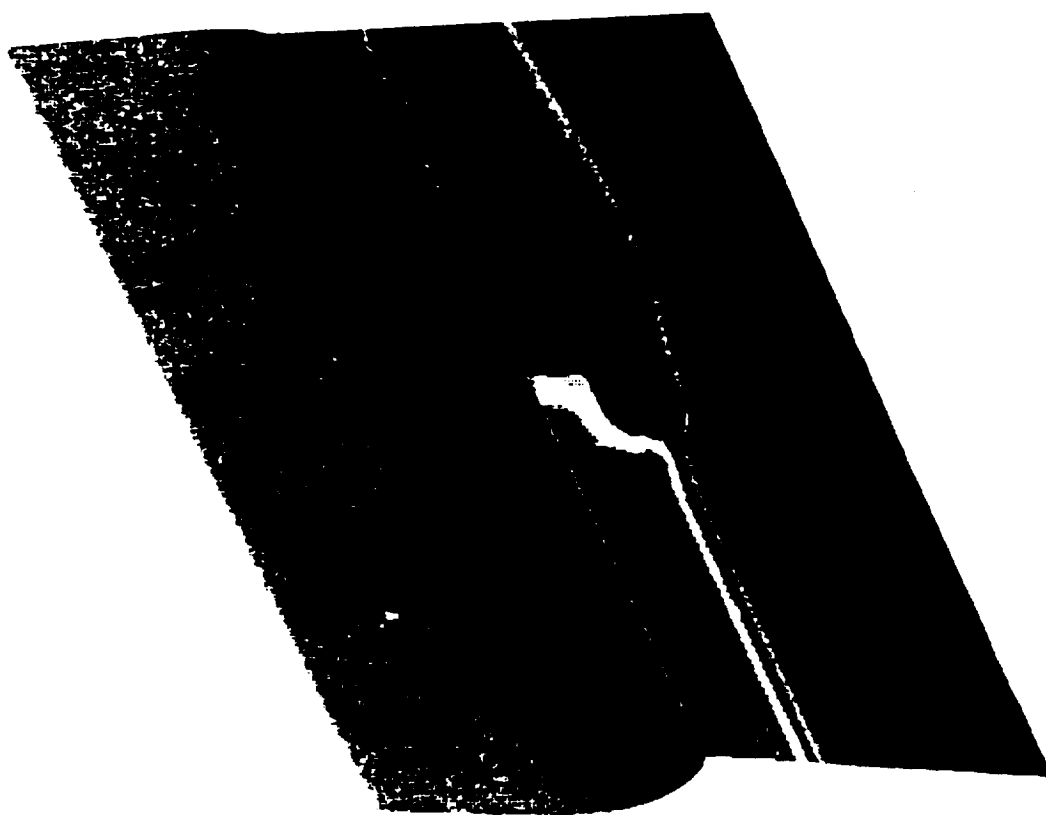


Fig. 5.64 Pressure contours in the stagnation plane($\theta = 0$).

Rayleigh pitot formula as

$$\frac{p_o}{p_\infty} = \left(\frac{6M_1^2}{5}\right)^{\frac{7}{2}} \left(\frac{6}{7M_1^2 - 1}\right)^{\frac{5}{2}} \quad (5.1)$$

Where M_1 is the normal Mach number. The stagnation line heat transfer is obtained by the following expression developed by Beckwith and Gallagher [77]

$$q_o = k_\infty \frac{T_{aw} - T_w}{2D} \left(\frac{2Re_{D,\infty}\mu_o}{M_\infty\mu_\infty}\right)^{\frac{1}{2}} \left[\frac{2T_\infty p_o}{\gamma T_o p_\infty} \left(\frac{p_o}{p_\infty} - 1\right)\right]^{\frac{1}{4}} \quad (5.2)$$

where

$$T_{aw} = T_e \left(1 + r \frac{\gamma - 1}{2} M_e^2\right)$$

here r is the recovery factor and is taken as 0.85 and subscript e denotes the boundary layer edge conditions.

Figure 5.65 shows the comparison of stagnation line pressure with the experimental data of Keyes and Hains [32] and numerical calculations of Holst et al. [47]. In the experimental set up, the interaction point was only 3 cm downstream from the end of the cylinder ($z = 0$) and, therefore, there was some relieving effect (Fig. 5.62). But in the present calculations, the body is assumed as infinite in length and hence no relieving effect is allowed. Due to this discrepancy in the model used, the results do not match near the end. However, the results compare fairly well away from the end point. The peak value of the pressure is caused by the interaction of the transmitted shock with the boundary layer and it is very well captured. The flow overexpands and then recompresses back to the unimpinged value. The peak value of the pressure is about 2.2 times the unimpinged stagnation line pressure. The variation of the stagnation line heat transfer is shown in Fig. 5.66. In this case also, the comparison is poor near the end for the same reasons as explained earlier. But away from the end, results compare fairly well. As expected, the heat transfer follows the same general trend as the pressure. The peak value of heat transfer is about three times the unimpinged stagnation line heat transfer. The experimental data is available only for the stagnation plane.

The results from the present calculations show a remarkable improvement over Holst's calculations due to various factors. The flow field is much better resolved due to a finer grid, no artificial thickening of the boundary layer has been attempted and the boundary condition at the end ($z=0$) are physically correct. The present calculations employ zero gradient conditions at the end which are physically realistic. In the previous calculations, the flow was maintained at constant conditions corresponding to the unimpinged flow solution, which is incorrect for the impinging shock case.

The variation of pressure and heat transfer at the surface is shown in Figs. 5.67 and 5.68 for various values of y . The stagnation line ($y=0$) has the maximum amplification of pressure and heating rates as the bow shock has its maximum strength along this line. Away from the stagnation line, strength of bow shock decreases. Consequently, the interaction becomes weaker and weaker, thereby causing less amplification of the wall quantities.

The circumferential variations of the wall pressure and the heat transfer are shown in Figs. 5.69 and 5.70 for various values of z . The impinging shock intersects at the normal portion of the bow shock at $z = 2.4$ cm, and therefore, the peak values of pressure and heating occur in this circumferential plane. At higher values of z , the impinging shock intersects away from the normal portion of the bow shock, thus reducing the amplification.

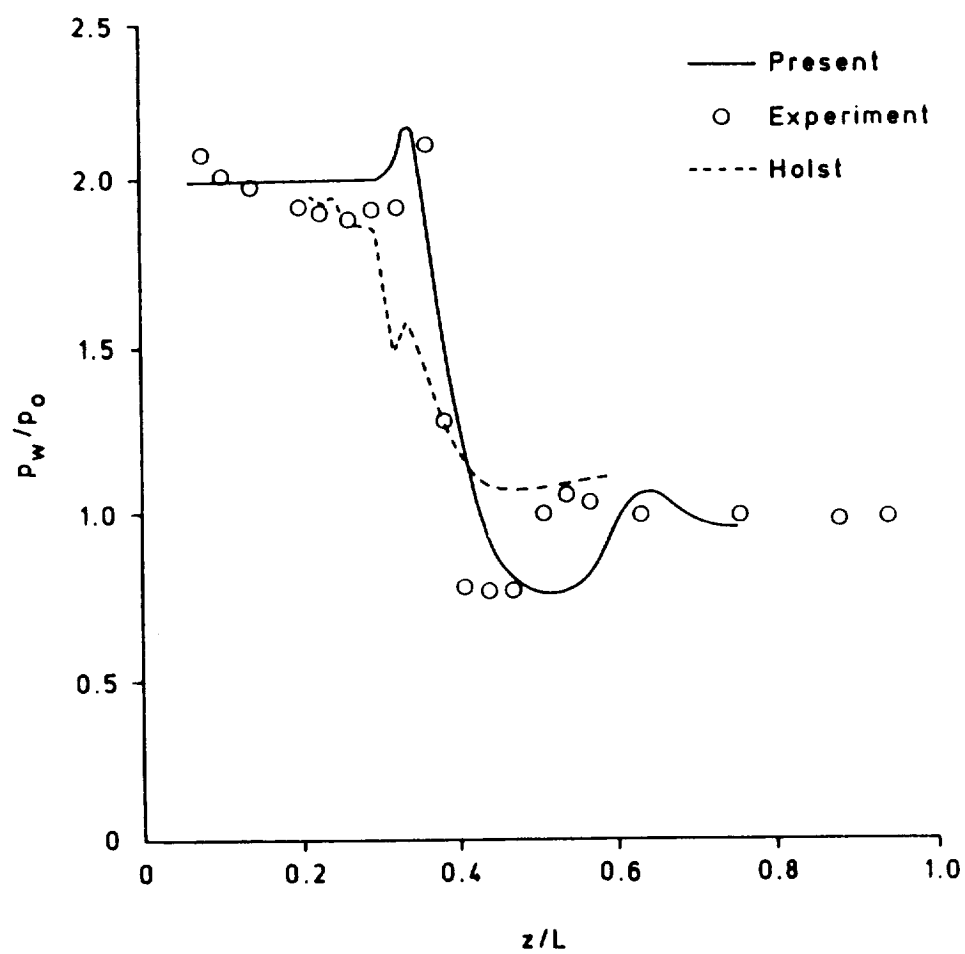


Fig. 5.65 Comparison of surface pressure with the experimental data.

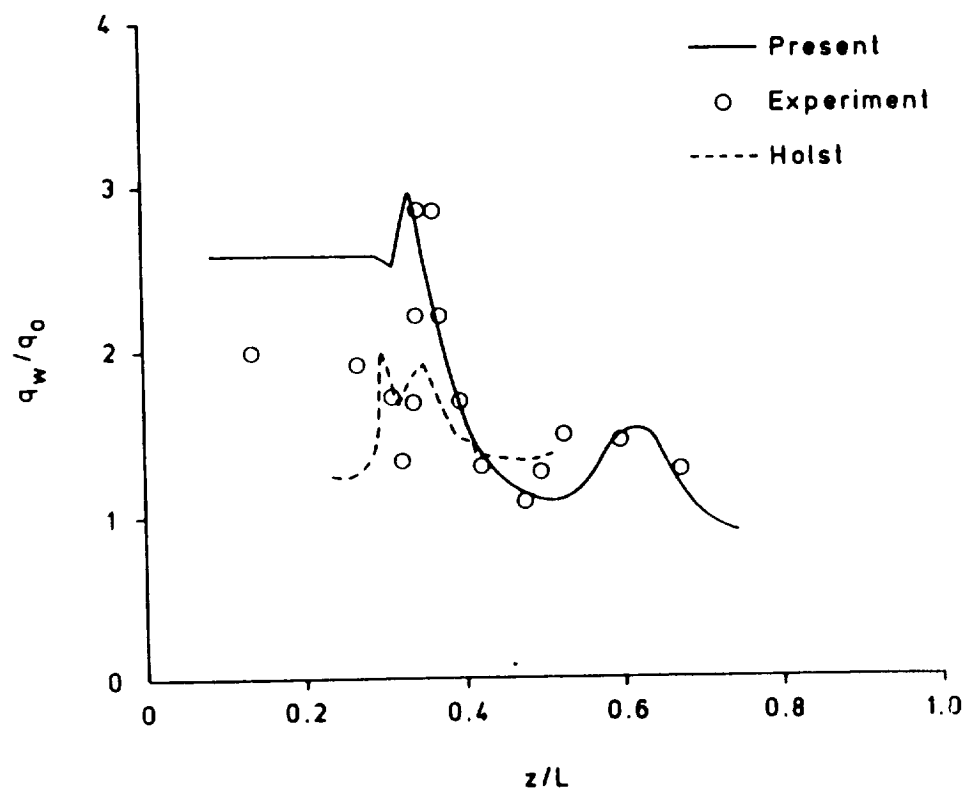


Fig. 5.66 Comparison of surface heat transfer with the experimental data.

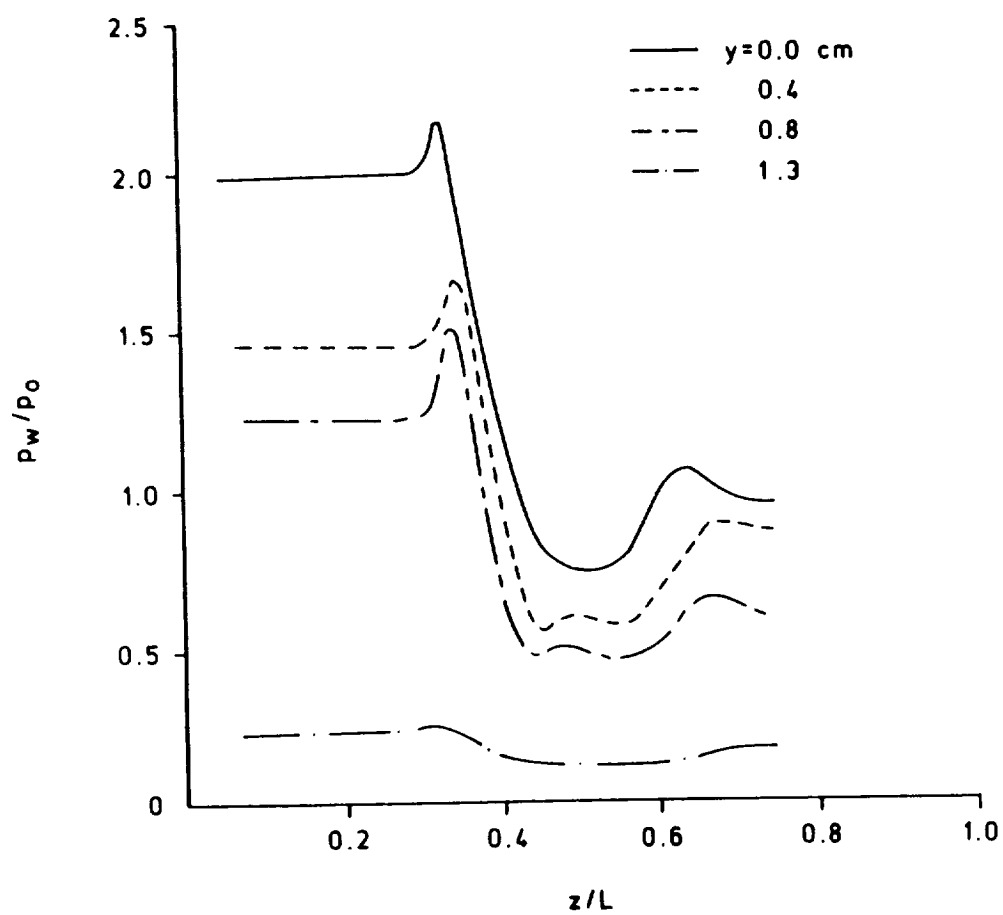


Fig. 5.67 Variation of the surface pressure in various $y = \text{constant}$ planes

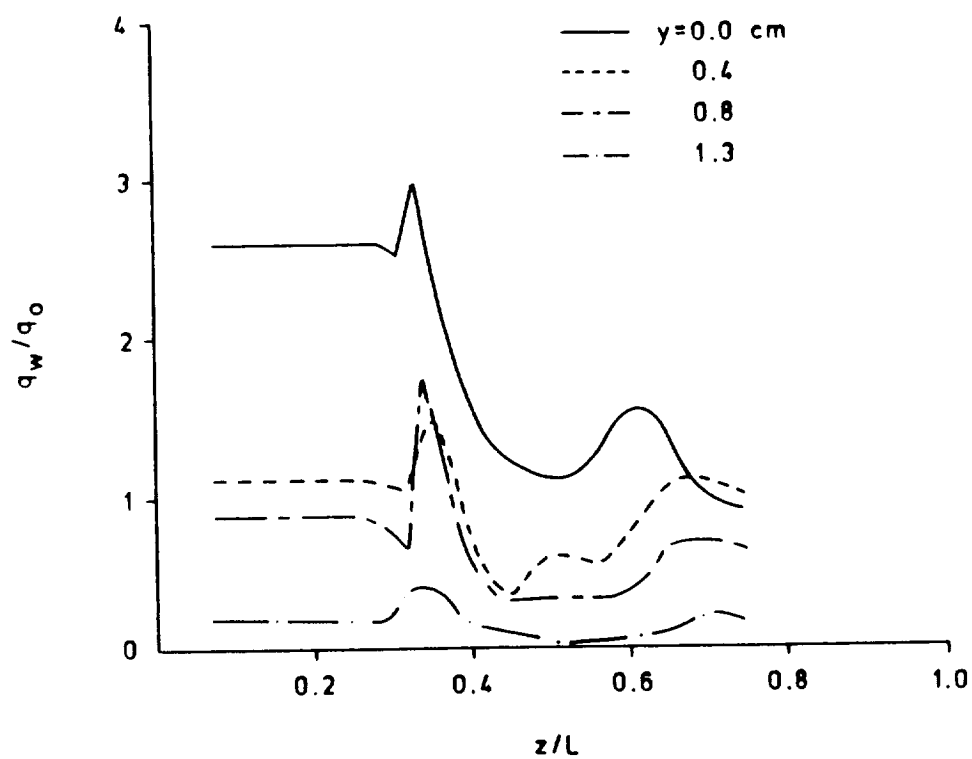


Fig. 5.68 Variation of the surface heat transfer in various $y = \text{constant}$ planes

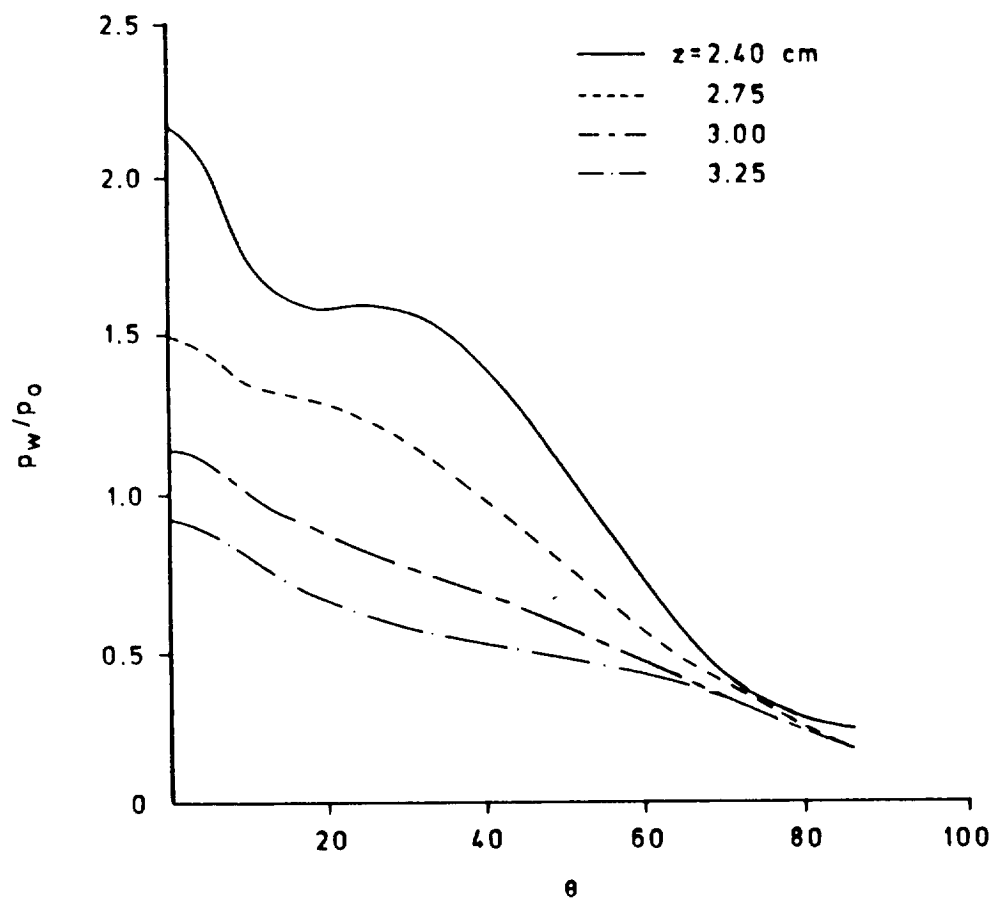


Fig. 5.69 Variation of the surface pressure in various $z = \text{constant}$ planes

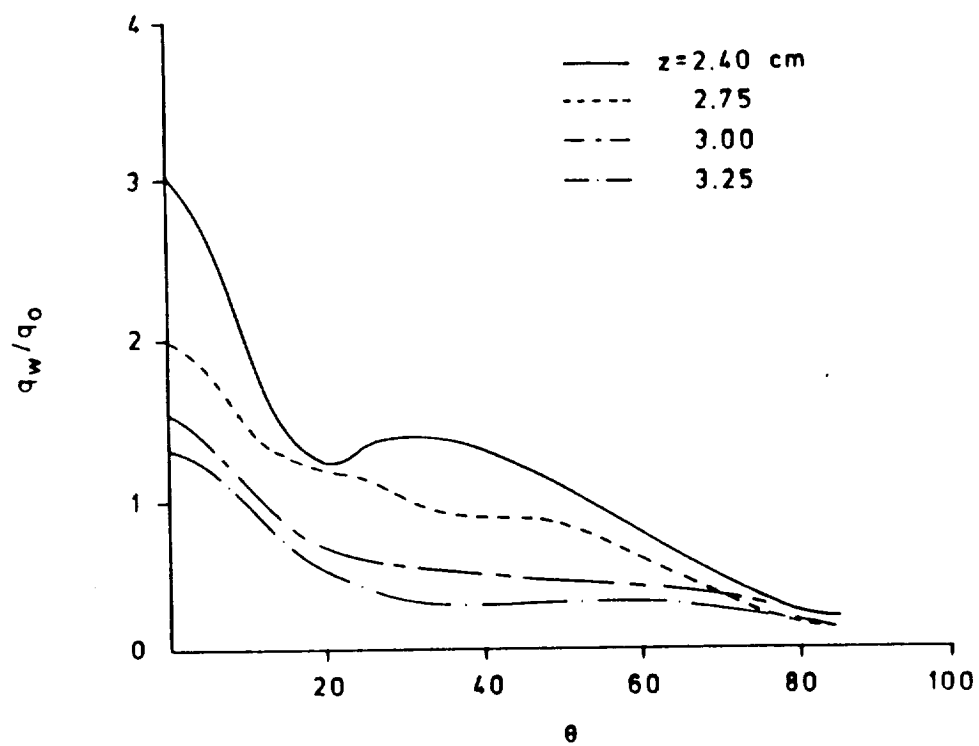


Fig. 5.70 Variation of the surface heat transfer in various $z = \text{constant}$ planes

Chapter 6

CONCLUSIONS

This study presents a numerical investigation of the effects of blunt leading edges on the viscous flow field around a hypersonic vehicle such as the proposed National Aero-Space Plane. Attention is focused on two specific regions of the flow field. In the first region, effects of nose bluntness on the forebody flow field are investigated. The second region of the flow considered is around the leading edges of the scramjet inlet where the forebody shock interacts with the shock produced by the blunt leading edges of the inlet compression surfaces.

An accurate solution procedure is developed to determine the downstream influence of forebody bluntness and the conditions, under which it can be modeled by a relatively simple pointed nose body of revolution, are determined. A wide range of physical and geometrical conditions are considered. The geometrical models used are spherically blunted cones of 5° , 10° , and 20° angles and ogives with various degree of bluntness. Several approximate methods as well as combination of Navier-Stokes and parabolized Navier-Stokes equations are used to accurately compute the flow field. The high temperature effects are incorporated by using equilibrium gas model. The influence of entropy layer generated by the shock curvature on the flow field are also addressed. The results show that the effects of leading edge bluntness persist several hundred nose radii downstream depending upon the bluntness, freestream conditions and geometry. It is found that the entropy layer

generated by the shock curvature affects the development of the boundary layer far downstream of the nose. These effects decrease with increasing Mach number. Also the bluntness effects decrease with increasing cone angle. The results show that the wall quantities are not affected much by the inclusion of high temperature effects through equilibrium chemistry for the conditions considered in the study.

The interaction of the forebody shock with the blunt cowl shock and with the shock produced by the blunt leading edge shock of the inlet is also investigated. The calculation of flow field and aerothermal loads under such conditions is quite difficult due to complexity of the flow field and the presence of high gradients. A modern computational algorithm developed by van Leer which has the advantage of better modeling of physics of the problem has been used. The impinging forebody shock is treated as a sharp discontinuity across which the exact shock jump conditions (Rankine-Hugoniot) are applied. The compressible Navier-Stokes equations are solved using a shock capturing algorithm. It does not require any prior information about the shock impingement flow field to be computed as is the case with some of the previous semi-empirical approaches. The use of solution adaptive grid technique to properly resolve the flow gradient is made and the importance of suitable grid in the numerical calculations is shown. The numerical computations are primarily done for Type IV supersonic jet interaction since it represents the most severe case in terms of aerothermal loads. A preliminary investigation of the Type V interaction which occurs on the leading edge of the compression side walls of the inlet is also made. The flow field for this interaction is found to be fully three-dimensional unlike the cowl plate interaction. Results of the study show the presence of local regions of very high surface pressure and intense heating. For Type IV interaction, the peak amplification of pressure is found to be nine times and heating amplification to be eight times the stagnation point value of the unimpinged case. The degree of amplification is found to increase with the increas-

ing Mach number. For Type V interaction, the amplification factors are found to be much lower, the pressure is amplified by a factor of 2.25 and heat transfer three times the stagnation values for unimpinged case. The results compare well with the experimental data. The study demonstrates the capability of CFD to simulate extremely complex viscous hypersonic flows.

Based on the present study, several recommendations concerning the extensions of this work are suggested.

- (1) The realistic forebody geometry should be used for calculating bluntness effect.
- (2) The flow in the present investigation is assumed to be laminar, but in actuality the flow would be turbulent, so an appropriate turbulence model should be incorporated into the governing equations.
- (3) Due to high Mach number flows considered, it would be desirable to examine the non-equilibrium high temperature effects.
- (4) The oscillatory behavior of the supersonic jet in Type IV interaction needs to be further investigated.
- (5) Since the inlet will have more than one shock impinging on it, the effects of multiple shock wave interaction needs to be determined.
- (6) The effects of oscillations in the impinging shock should be investigated.
- (7) The use of adaptive grids for three-dimensional calculations to properly resolve the flow should be made.
- (8) For Type V interaction considered, the end effects should be accounted for to have a better comparison with the experiment by using zonal techniques.
- (9) The effects of shock wave interference in the presence of active cooling should be determined because to relieve the thermal stresses, some form of active cooling would be used.
- (10) Various shock interference pattern for three-dimensional calculations should be computed by varying the sweep angle.

REFERENCES

- [1] Truitt, R. W., Hypersonic Aerodynamic, Ronald Press, New York, 1959.
- [2] Hayes, W. D. and Probstein, R. F., Hypersonic Flow Theory, Academic Press, New York, 1959.
- [3] Chernyi, G. G., Introduction to Hypersonic Flow (Translated from Russian by R. F. Probstein), Academic Press, New York, 1961.
- [4] Dorrance, W. H., Viscous Hypersonic Flow, McGraw-Hill Book Co., New York, 1962.
- [5] Cox, R. N. and Crabtree, L. F., Elements Of Hypersonic Aerodynamics, Academic Press, New York, 1965.
- [6] Hammitt, A. G. and Bogdonoff, S. M., "Hypersonic Studies of the Leading Edge Effect on the Flow Over a Flat Plate," Jet Propulsion, Vol. 26, No. 4, April 1956, pp.241-246.
- [7] Vas, I. E., Bogdonoff, S. M., and Hammitt, A. G., "An Experimental Investigation of the Flow Over Simple Two Dimensional and Axial Symmetric Bodies at Hypersonic Speeds," Jet Propulsion, Vol. 26, No. 2, February 1958, pp. 97-104.
- [8] Allegere, J. and Bisch, C., "Angle of attack and Leading Edge Effects on the Flow about a Flat Plate at Mach Number 18," AIAA Journal, Vol. 6, No. 5, May 1968, pp. 848-852.
- [9] Cheng, H. K., Gordon Hall, J., Golian, T. C., and Hertzberg, A., "Boundary Layer Displacement and Leading-Edge Bluntness Effects in High-Temperature Hypersonic Flows," Journal of the Aero/Space Sciences, Vol. 28, No. 5, May 1961, pp. 353-381.
- [10] Bradfield, W. S., Decouroin, D. G., and Blumer, C. G., "The Effect of Leading Edge Bluntness on a Laminar Supersonic Boundary Layer," Journal of the Aeronautical Sciences, Vol. 21, No. 6, June 1954, pp. 373-382.
- [11] Vas, I. E. and Sierchio, J. G., "Down Stream Effect of Bluntness in the Merged Flow Regime," Rarefied Gas Dynamics, Edited by Karamcheti, K., Academic Press, New York 1972.
- [12] McCroskey, S., Bogdonoff, S. M., and Genchi, A. F., "Leading Edge Flow Studies of Sharp Bodies in Rarefied Hypersonic Flows," Rarefied Gas Dynamics, 5th Symposium, Vol. 2, 1967, pp. 1047-1066.

- [13] Feik, R. A., Genchi, A., and Vas, I. E., "A Study of Merging of Cones," Rarefied Gas Dynamics, Supplement 5, Vol. 1, 1969, pp. 493-499.
- [14] Vogenitz, F. W. and Takata, G. Y., "Rarefied Hypersonic Flow about Cones and Flat Plates by Monto Carlo Simulation," AIAA Journal, Vol. 9, No. 1, January 1971, pp. 94-100.
- [15] Burke, A. F. and Curtis, J. T., "Blunt Cone Pressure Distribution at Hypersonic Mach Numbers," Journal of the Aero/Space Sciences, Vol. 29, February 1962, pp. 237-238.
- [16] Bertram, M. H., "Tip-Bluntness Effects on Cone Pressure at Mach 6.85" Journal of the Aero/Space Sciences, Vol. 23, No. 9, September 1956, pp. 898-900.
- [17] Dewey, C. F., "Bluntness and Viscous-Interaction Effects on Slender Bodies at Hypersonic Speeds," AIAA Paper 65-63, January 1965.
- [18] Cheng, H. K. and Pallone A. J., "Inviscid Leading Edge Effects in Hypersonic Flows," Reader's Forum, Journal of the Aeronautical Sciences, Vol. 23, No. 7, July 1956, pp. 700-702.
- [19] Lees, L. and Kubota, T., "Inviscid Hypersonic Flow Over Blunt Nosed Slender Bodies," Journal of the Aeronautical Sciences, Vol. 24, No. 3, March 1957, pp. 195-202.
- [20] Cheng, H. K., "Similitude of Hypersonic Real Gas Flows Over Slender Bodies with Blunted Noses," Journal of the Aeronautical Sciences, Vol. 26, No. 9, September 1959, pp. 575-585.
- [21] Lees, L., "Laminar Heat Transfer Over Blunt Nosed Bodies at Hypersonic Flight Speeds," Jet Propulsion, Vol. 26, No. 4, April 1956, pp. 259-269.
- [22] De Jarnette, F. R. and Davis, R. M., "A Simplified Method for Calculating Laminar Heat Transfer Over Bodies at an Angle of Attack," NASA TN D-4720, August 1968.
- [23] Stetson, K. F., "Nose Tip Bluntness Effects on Cone Frustum Boundary Layer Transition in Hypersonic Flow," AIAA Paper 83-1763, July 1983.
- [24] Nowak, R. J., Albertson, C. W., and Hunt, L. R., "Aeronautical Tests of a 12.5° Cone at Attack, and Nose Shapes," NASA TP 2345, January 1985.
- [25] Zoby, E. V. and Simmonds, A. L., "Engineering Flowfield Methods with Angle of Attack Applications," Journal of Spacecrafts and Rockets, Vol. 22, No. 4, July-August 1985, pp. 398-404.
- [26] Thompson, R. A., Zoby, E. V., Wurster, K. E., and Gnoffo, P. A., "An Aerothermodynamic Study of Slender Conical Vehicle," AIAA Paper 87-1475, June 1987.
- [27] Gupta, R. N., Lee, K. P., Moss, J. N., Zoby, E. V., and Tiwari, S. N., "Viscous Shock Layer Analysis of Long Slender Bodies," AIAA Paper 87-2487, August 1987.

- [28] Zoby, E. V., Lee, K. P., Gupta, R. N., Thompson, R. A., and Simmonds, A. L., "Viscous Shock Layer Solutions with Nonequilibrium Chemistry for Hypersonic Flows Past Slender Bodies," AIAA Paper 88-2709, June 1988.
- [29] Teterin, M. P., "Study of Gas Flow in Region of Incidence of a Shock on a Cylinder in High Supersonic Flow," Fluid Dynamics, Vol. 2, Number 2, March-April 1967, pp. 98-100.
- [30] Sukovstin, A. G. and Shestova, N. P., "Incidence of Plane Supersonic Jet on a Plane at an Arbitrary Angle," Fluid Dynamics, Vol. 2, Number 4, July-August 1967, pp. 97-100.
- [31] Edney, B. E., "Anomalous Heat Transfer and Pressure Distribution on Blunt Bodies at Hypersonic Speeds in the Presence of an Impinging Shock," Aeronautical Research Institute of Sweden, FAA Report 115, February 1968.
- [32] Keyes, J. W. and Hains, F. D., "Analytical and Experimental Studies of Shock Interference Heating in Supersonic Flows," NASA TN D-7139, May 1973.
- [33] Craig, R. R. and Ortwerth, P. J., "Experimental Study of Shock Impingement on a Blunt Leading Edge with Application to Hypersonic Inlet Design," Air Force Patterson Aeronautical Laboratory Report, AFPAL-TR-71-10, October 1971.
- [34] Wieting, A. R. and Holden, M. S., "Experimental Study of Shock Wave Interference Heating in Supersonic Flows," AIAA Paper 87-1511, June 1987.
- [35] Morris, D. J. and Keyes, J. W., "Computer Programs for Predicting Supersonic and Hypersonic Interference Flowfield and Heating," NASA TM X-2725, May 1973.
- [36] Crawford, D. H., "A Graphical Method for the Investigation of Shock Interference Phenomena," AIAA Journal, Vol. 11, November 1973, pp. 1590-1592.
- [37] Keyes, J. W. and Morris, D. J., "Correlations of Peak Heating in Shock Interference Regions at Hypersonic Speeds," Journal of Spacecraft and Rockets, Vol. 9, August 1972, pp. 621-623.
- [38] Bramlette, T. T., "Simple Technique for Predicting Type III and IV Shock Interference," AIAA Journal, Vol. 2, August 1974, pp. 1151-1152.
- [39] Markarian, C. F., "Heat Transfer in Shock Wave Boundary layer Interactions," Naval Weapons Center, China Lake, California, NWC TP 4485, November 1968.
- [40] Bertin, J. J., Graumann, B. W., and Goodrich, W. D., "Analysis of High Velocity and Real Gas Effects On the Shock-Interference Pattern for Delta-Wing Orbiters," AIAA Paper 74-522, June 1974.
- [41] Tannehill, J. C., Holst, T. L., and Rakich, J. V., "Numerical Computation of a Two-Dimensional Viscous Blunt Body Flows with an Impinging Shock," AIAA Journal, Vol. 14, No. 2, February 1976, pp. 204-216.
- [42] Tannehill, J. C., Holst, T. L., Rakich, J. V., and Keyes, J. W., "Comparison of a Two-Dimensional Shock Impingement Computation With Experiment," AIAA Journal, Vol. 14, April 1976, pp. 539-541.

- [43] White, J. A. and Rhie, C. M., "Numerical Analysis of Peak Heat Transfer Rates for Hypersonic Flow Over a Cowl Leading Edge," AIAA Paper 87-1895, June 1987.
- [44] Klopfer, G. H. and Yee, H. C., "Viscous Hypersonic Shock-on-Shock Interaction on Blunt Cowl Lips," AIAA Paper 88-0233, January 1988.
- [45] Perry, K. M. and Imley, S. T., "Blunt Body Flow Simulations" AIAA Paper 88-2904, July 1988.
- [46] Moon, Y. J. and Holt, M., "Interaction of an Oblique Shock with Turbulent Hypersonic Blunt Body Flows," AIAA Paper 89-0272, January 1989.
- [47] Holst, T. L., Tannehill, J. C., and Rakich, J. V., "Numerical Computation of Viscous Blunt Body Flows with Planer Impinging Shock," Presented at the NASA Conference on Aerodynamic Analysis Requiring Advanced Computers, March 4-6, 1975, Langley Research Center, Hampton, Virginia.
- [48] Ferri, A., "Some Heat Transfer Problems in Hypersonic Flows," Aeronautics and Astronautics, Pergammon Press, New York, 1960. pp. 344-377.
- [49] Klaimson, J. H., "Bow Shock Correlations for Slightly Blunted Cones," AIAA Journal, Vol. 1, No. 2, February 1963, pp. 490-491.
- [50] Rotta, N. R., "Effects of Nose Bluntness on the Boundary Layer Characteristic of Conical Body of Hypersonic Speed," New York University Report, NY-AA-66-66, November 1966.
- [51] Anderson, D. A., Tannehill, J. C., and Pletcher, R. H., Computational Fluid Mechanics and Heat Transfer, McGraw Hill, New York 1984.
- [52] Gnoffo, P. A., "A Vectorized Finite Volume, Adaptive Grid Algorithm Applied to Planetary Entry Problems," AIAA Paper 82-1018, June 1982.
- [53] Vigneron, Y. C., Rakich, J. V., and Tannehill, J. C., "Calculation of Supersonic Viscous Flow Over Delta Wings with Sharp Subsonic Leading Edges," NASA TM 78500, June 1978.
- [54] Gnoffo, P. A., "Hypersonic Flow Over Biconics Using a Variable-Effective-Gamma, Parabolized-Navier-Stokes Code," AIAA Paper 83-1666, July 1983.
- [55] Beam, R. M. and Warming, R. F., "An Implicit Factored Scheme for the Compressible Navier Stokes Equation," AIAA Journal, Vol. 16, 1978, pp.393-401.
- [56] Kumar, A., Graves, R. A., and Weilmuenster, K. J., "Users Guide for Vectorized Code EQUIL for Calculating Equilibrium Chemistry on Control Data STAR 100 Computer," NASA TM 80193, April 1980.
- [57] Vaglo-Laurin, R. and Bloom, M. H., "Chemical Effects in External Hypersonic Flows," Hypersonic Flow Research, Vol. 7, Progress in Astronautics and Rocketry, Progress in Astronautics and Rocketry, Academic Press, New York, 1962. pp. 205-254.
- [58] Whalen, R. J. "Viscous and Inviscid Nonequilibrium Gas Flows," Institute of Aerospace Sciences Paper No. 61-23, IAS 29th Annual Meeting, New York, January 1961.

- [59] White, F. M., Viscous Fluid Flow, McGraw Hill Book Co., New York 1974.
- [60] Shapiro, A. H., The Dynamics and Thermodynamics of Compressible Fluid Flow, Vol. 1, Ronald Press, New York, 1959.
- [61] Holden, M. S., "Shock-Wave-Turbulent Boundary Layer Interaction in Hypersonic Flows," AIAA 72-72, 1972.
- [62] van Leer, B., Thomas, J. L., Roe, P. L., and Newsome, R. W., "A Comparison of Numerical Flux Formulas for the Euler and Navier-Stokes Equations," AIAA paper 87-1104, June 1987.
- [63] Moretti, G., "The λ Scheme," Computer and Fluids, Vol. 7, 1979, pp. 191-205.
- [64] Chakravarty, S. R., Anderson, D. A., and Salas, M. D., "The Split Coefficient Matrix Method for Hyperbolic System of Gas Dynamics Equations," AIAA Paper 80-0268, January 1980.
- [65] Gudonov, S. K., "A Finite Difference Method for the Numerical Computation of Discontinuous Solutions of the Equations of Fluid Dynamics," Matematicheskii Sbornik (Novaja Seriya) Vol. 47, 1959, pp. 271-306.
- [66] Osher, S. and Soloman, F., "Upwind Difference Schemes for Hyperbolic System of Conservation Law," Mathematics of Computation, Vol. 38, April 1982, pp. 339-374.
- [67] Yee, H. C., "Linearized form of Implicit TVD Schemes for Multidimensional Euler and Navier-Stokes Equations," Computers and Mathematics with Applications, Vol. 12A, April-May 1986, pp. 413-432.
- [68] Roe, P. L., "Approximate Riemann Solver, Parameter Vectors and Difference Schemes" Journal of Computational Physics, Vol. 43, October 1981, pp. 357-372.
- [69] Steger, J. L. and Warming, R. F., "Flux Vector Splitting for the Inviscid Gas Dynamics Equations with Applications to Finite Difference Methods," Journal of Computational Physics, Vol. 40, April 1981, pp. 263-293.
- [70] van Leer, B., "Flux Vector Splitting for the Euler Equations" Lecture Notes in Physics, Vol. 170, Springer-Verlag, New York, 1982, pp. 507-512.
- [71] MacCormack, R. W., "The Effect of Viscosity in Hypervelocity Impact Cratering," AIAA Paper 78-257, May 1968.
- [72] Personnel Communication with Dr. E. v. Lavante of Old Dominion University, Norfolk, Va.
- [73] Thomas, J. L. and Walters, R. W., "Upwind Relaxation Algorithms for the Navier-Stokes Equations," AIAA Paper 85-1501, July 1985.
- [74] Newsome, R., Walters, R. W., and Thomas, J. L., "An Efficient Iteration Strategy For Upwind/Relaxation Solutions to the Thin-Layer Navier-Stokes Equations," AIAA Paper 87-1113, June 1987.

- [75] Rumsey, C. L., Taylor, S. L., Thomas, J. L., and Anderson, W. K., "Application of an Upwind Navier-Stokes Code to a Two-Dimensional Transonic Airflow Flow," AIAA Paper 87-0413, 1987.
- [76] Abolhassani, J. S., Smith, R. E., and Tiwari, S. N., "Grid Adaptation for Hypersonic Flow," AIAA Paper 87-1169, June 1987.
- [77] Beckwith, I. E. and Gallagher, J. J., "Local Heat Transfer and Recovery Temperatures on a Yawed Cylinder at a Mach Number of 4.14 and High Reynolds number," NASA TR, R-104, 1961.
- [78] White, W.B., Johnson, S. M., and Dantzig, G.B., "Chemical Equilibrium in Complex Mixture," Journal of Chemical Physics, Vol. 28, No. 5, May 1958, pp. 751-755.
- [79] Tiwari, S. N., Singh, D. J., and Kumar, A., "Transient Energy Transfer by Conduction and Radiation in Nongray Gases," Journal of Thermophysics and Heat Transfer, Vol. 3, No. 2, April 1989, pp. 167-174.
- [80] Tiwari, S. N., and Singh, D. J., "Interaction of Transient Radiation in Fully Developed Laminar Flows," AIAA Paper 87-1521, June 1987.
- [81] Tien, C. L., "Thermal Radiation Properties of Gases," Advances in Heat Transfer, Vol. 3, Academic Press, New York, 1968.

APPENDICES

APPENDIX A

EQUILIBRIUM CHEMISTRY

A fully vectorized code EQUIL as described in [56] has been used in the present analysis to include the real gas effects. It is based on free energy minimization technique [78] in which the method of steepest descent is used. In this method, with the known values of local temperature, pressure and elemental mass fractions of the gas, the mole numbers of species are calculated which minimizes the free energy. The free energy of a mixture of n species containing x_i moles of the i th species is expressed as

$$F(X) = \sum_{i=1}^n f_i \quad (\text{A.1})$$

where

$$X = (x_1, x_2, x_3, \dots, x_n) \quad (\text{A. 2})$$

$$f_i = x_i \left[c_i + \ln \frac{x_i}{\bar{x}} \right] \quad (\text{A. 3})$$

$$c_i = \left(\frac{F}{RT} \right)_i + \ln P \quad (\text{A. 4})$$

$$\bar{x} = \sum_{i=1}^n x_i \quad (\text{A. 5})$$

Equation (A.1) is minimized, subject to mass balance constrain. An initial assumption is made on the mole numbers of various species, and then an iterative procedure is followed to find the set of mole numbers which satisfy both the constraints. Once the mole numbers are known, the molecular weight and mass fraction

of each species are calculated. The specific heat, free energy, viscosity and thermal conductivity are calculated using polynomial expressions given below.

$$\frac{c_p}{R} = a_1 + a_2T + a_3T^2 + a_4T^3 + a_5T^4 \quad (\text{A. 6})$$

$$\frac{H}{RT} = a_1 + a_2\frac{T}{2} + a_3\frac{T^2}{3} + a_4\frac{T^3}{4} + a_5\frac{T^4}{5} + a_6\frac{1}{T} \quad (\text{A. 7})$$

$$\frac{F}{RT} = a_1(1 - \ln T) - a_2\frac{T}{2} - a_3\frac{T^2}{6} - a_4\frac{T^3}{12} - a_5\frac{T^4}{20} + a_6\frac{1}{T} + a_7 \quad (\text{A. 8})$$

$$\mu = b_1 + b_2T + b_3T^2 \quad (\text{A. 9})$$

$$k = c_1 + c_2T \quad (\text{A. 10})$$

The values of constants $a_1, a_2, \dots, a_7, b_1, \dots, b_3, c_1$ and c_2 are given in [56]

APPENDIX B

ADAPTIVE GRID

An adaptive grid system was employed to improve the quality of the solution without increasing the number of grid points. The accuracy of the numerical solution depends on the fineness of the grid. The presence of large gradients causes the error to be large in numerical approximation of the derivatives. Therefore, it is desirable to have fine grid spacing near the shocks, shear layers, and boundary layer. The method developed by Abolhassani et al. [76] has been used. It is a very general method with capability to adapt the grids with various variables such as pressure, Mach number, shear stress etc and is based on variational approach. It is an algebraic method and is formulated in such a way that there is no need for matrix inversion, which makes it computationally very efficient. The grids were adapted by using Euler Lagrange equations

$$X_{\xi}w = constant \quad (B. 1)$$

This equation can be written in normalized form as

$$\xi(s) = \frac{\int_0^s w(t)dt}{\int_0^1 w(t)dt} \quad (B. 2)$$

where s is the arc length. The weight function is used to reduce the grid point spacing where w is large. For grid adaptation with several variables, the weight

function is expressed as

$$w = 1 + \sum_{i=1}^n b_i f_i \quad (\text{B. 3})$$

where n is the number of variables, b_i are the constants and f_i are the variables (or their derivatives). The constant 1 is for uniformity. The values of b_i are calculated based on percentage of grid points allocated to each variable. The percentage of grid points for each f_i can be written as

$$R_j = \frac{b_j F_j(S_{max})}{S_{max} + \sum_{i=1}^n b_i F_i(S_{max})}; j = 1, 2, 3, 4, \dots \quad (\text{B. 4})$$

where

$$F_i(s) = \int_0^s f_i(t) dt$$

The integral is approximated by a trapezoidal rule. After some algebraic manipulations, Eqs. (B.2) and (B.4) can be written as

$$\xi(s) = \frac{s}{s_{max}} \left[1 - \sum_{i=1}^n R_i \right] + \sum_{i=1}^n R_i \frac{F_i(s)}{F_i(S_{max})} \quad (\text{B. 5})$$

In order to avoid extremely small grid spacing near the shocks, the weight functions f_i are multiplied by the factor

$$1 - e^{\frac{-\Delta s}{\Delta S_{min}}} \quad (\text{B. 6})$$

where ΔS_{min} is the allowable minimum spacing. The function varies from 0 to 1 and is proportional to the spacing.

APPENDIX C

RADIATIVE INTERACTIONS IN LAMINAR FLOWS

A preliminary study was conducted to include the radiative formulation in the general governing equations and provide the step by step analysis and solution procedure for realistic problems. The objective of this study was to prepare the ground work for future studies of inlet flows involving radiative interactions. The original plan was to compute the inlet flow in combination with shock-shock interaction as well as radiative heat transfer. But due to time limitation this part of study could not be completed. However, some very important results were obtained during the course of this study. A brief introduction to the problem is given here, the details are available in [79] and [80].

The problem has been formulated in such a way that any nongray gas model for participating species can be used. The governing equations involving radiative interactions, in general, are integro-differential equations. In order to fully understand the radiative part, it was decided to use a very simple fluid dynamic model along with sophisticated nongray gas models. The laminar flow of participating species between two parallel plates was considered. The Tien and Lowder [81] wide-band correlation model was used to account for the spectral properties. The walls are assumed as black.

Specific results were obtained for energy transfer by pure radiation, radiation and conduction, and finally by radiation, conduction and convection. The participating species considered were CO, OH, CO₂, H₂O and their mixtures. It was noted that the extent of radiative interaction is dependent on the nature of participating species and parameter such as T_1 , T_2/T_1 , P and PL . Here T_1 and T_2 are lower and upper wall temperatures, P is the pressure and L is the plate spacing. Radiative ability of a gas was found to increase with increasing pressure, temperature and plate spacing. For most conditions, H₂O was found to be a highly participating species (as compared to CO, OH and CO₂)

The analysis, computational procedure, and results presented in [79] and [80] provide essential information on how to account for radiative interaction in internal flows. The models developed in the references can be used to investigate radiative interaction in complex flows as long as the system temperature remains within the range 300 - 5,000 K.

